technische universität
dortmund

Diploma Thesis

Self-consistent spin wave theory for a frustrated Heisenberg model in the collinear phase and the application for the iron pnictides

Daniel Stanek

June 18, 2010

Lehrstuhl für Theoretische Physik I
Fakultät für Physik
Technische Universität Dortmund

Supervised by Prof. Dr. Götz S. Uhrig.
Second advisor: Prof. Dr. Werner Weber

Typeset using LaTeX and KOMA-Script.

Contents

List of Figures

List of Tables

1. Abstract

In 2008, Kamihara *et al.* [1] reported superconductivity in the iron based compound $LaO_{1-x}F_xFeAs$ with a relatively high critical temperature of $T_c = 26$ K. Soon, superconductivity was discovered in other members of this family called iron pnictides with critical temperatures up to $T_c = 55$ K [2]. More than 20 years after the discovery of superconductivity in the copper oxides by Bednorz and Müller [3], where the critical temperatures were quickly pushed up to $T_c \sim 150$ K, these are the highest critical temperatures in copper-free compounds reported so far. Recently, pressure-induced superconductivity with $T_c = 36.7$ K has also been detected in the simple binary compound FeSe [4], which belongs to the class of ferro-chalcogenides. Most of the superconducting compounds discovered since the discovery of superconductivity in the copper oxides in 1986, for example the iron based LaOFeP [5], exhibit critical temperatures which are located more in the range of those found in conventional superconductors like mercury and lead.

Conventional superconductors are based on the formation of Cooper pairs, which is caused by an effective attraction between the electrons due to electron-phonon coupling. This is described very well by the famous Bardeen-Cooper-Schrieffer (BCS) theory proposed in 1957. For the copper-oxide-based superconductors, the underlying microscopic mechanism is still unknown. Current research activities concentrate mostly on the superconducting mechanism in the iron pnictides. Similar to the situation in the copper-oxides, the superconducting mechanism in the iron pnictides is not mediated via electron-phonon coupling [6].

The iron pnictides share similarities and dissimilarities with the copper-oxide based superconductors. Therein lies hope that iron pnictides lead to a deeper understanding of the microscopic mechanisms at high temperatures, which are not restricted to certain classes of materials.

Certainly, one important key role in the copper oxide-based as well as in the iron-based superconductors is assigned to the magnetism in these compounds. An attractive interaction between the charge carries might be induced by magnetic fluctuations. In the phase diagrams of both classes of materials, the antiferromagnetic long-range ordered phase is located close to the superconducting phase. In the iron pnictides, the superconducting and long-range ordered phase even overlap [7]. The long-range order in the pnictides shows an collinear order unequal to the Néel order. In the square lattice formed by the iron ions, the spins are aligned parallel in *b*-direction and antiparallel in *a*-direction.

In this thesis, we study the magnetic excitations in the three dimensional collinear phase for an frustrated Heisenberg model within *self-consistent spin wave theory* at zero temperature. The collinear ordered spin pattern is the one relevant for the iron pnictides. The three dimensional character of the magnetism in iron pnictides has recently been revealed by inelastic neutron scattering studies [8, 9, 10]. In addition, we introduce a biquadratic exchange in the collinear ordered layers to increase the anisotropy between the effective exchange constants perpendicular and parallel to the spin

stripes. Therefore, the quantitative accuracy of the mean field approximation has to be checked and compared with other methods. Finally, the model is fitted to experimental data of the iron pnictides to check its applicability. This work is based on previous studies by Uhrig *et al*. [11]. With respect to the results of Uhrig *et al*., we discuss the possibility that iron pnictides reside in the vicinity of a quantum phase transition for our model in three dimensions and with biquadratic exchange. Our studies are concluded by the discussion of the dynamical structure factor of our model, which gives evidence how inelastic neutron scattering counting rates look for our model.

The basic technique is self-consistent spin wave theory, which leads to a renormalization of the exchange constants due to quantum fluctuations. Namely, the *Dyson-Maleev* and the *Schwinger bosons* representation are applied to the extended Heisenberg model within an appropriate mean field approximation. The spin wave theory corresponds to an expansion in $1/S$, which is known to give very accurate results for $S = 1$. Then, the Hamiltonians can be diagonalized with standard techniques. The set of self-consistency equations, which we obtain for the quantum correction parameters, has to be solved numerically.

Outline

In Chapter 2, we briefly introduce the iron pnictides and some of their properties, which can be captured by a localized model. The Heisenberg model and the basics of collective magnetism are discussed. Furthermore, the biquadratic exchange, which leads to a strengthening of the anisotropy of the effective exchange constants, is motivated. In addition, we briefly present other eligible approaches to explain the magnetism in the iron pnictides.

Chapter 3 gives an introduction in spin wave theory and the corresponding basic techniques. As an example, the dynamical structure factor is evaluated within the Dyson-Maleev representation.

The relevant technique and the mean field decoupling for biquadratic exchange terms is discussed in Chapter 4. The Dyson-Maleev as well as the Schwinger bosons representation are applied to the two dimensional *Néel phase* with additional biquadratic exchange. By comparing our results to data from other theoretical techniques, the Dyson-Maleev representation is identified as the best choice for our purposes.

The three dimensional collinear phase is introduced and studied in Chapter 5. The numerics and the general results for different interlayer couplings are discussed and presented. In addition, special attention is paid to the critical point, where the collinear phase ceases to exist.

In Chapter 6, the biquadratic exchange between in-plane nearest neighbor sites, as introduced in Chapter 4, is included to our model of the three dimensional collinear phase. The discussed results show that the biquadratic exchange indeed helps to strengthen the anisotropy of the effective in-plane exchange constants.

To prove the relevance of our model for the iron pnictides, it is fitted to two different scenarios in Chapter 7. In detail, a merely theoretical scenario for the compounds $BaFe_2As_2$ and $SrFe_2As_2$ and

the experimental scenario for $CaFe_2As_2$ as determined from neutron scattering studies are discussed. Both scenarios are compared and the closeness to a quantum phase transition is discussed. In addition, the scenario of $CaFe_2As_2$ is discussed under the influence of the biquadratic exchange from Chapter 6. For a comparison with experimental data, constant-energy cuts are extracted from the dynamical structure factor and compared with constant-energy cuts obtained from neutron scattering.

Finally, Chapter 8 summarizes the results and gives a possible outlook for future work.

Further calculations and details about the used notation and conventions can be found in the appendices.

2. Introduction

In this chapter, we introduce the iron pnictides and some of their properties. Based on experimental and theoretical results, we motivate the localized approach for studying the magnetic excitations in the iron pnictides. The Heisenberg model is introduced briefly and the basics of collective magnetism are presented. Furthermore, a brief overview of the J_1-J_2 model and the collinear phase is given. In addition, we discuss the origin of biquadratic exchange and its relevance for the iron pnictides. For the sake of completeness, a short overview of alternative approaches for studying magnetism in the iron pnictides is given.

2.1. Iron pnictides

Since the discovery of superconductivity upon doping of the iron-based compound LaOFeAs by Kamihara *et al.* [1], it has emerged that there are basically two classes of iron pnictides with superconducting properties up to critical temperatures of $T_c = 56$ K [7].

The compound LaOFeAs belongs to the class of the 1111 pnictides, which are also known as oxypnictides since they contain oxygen. In general, these are the compounds ReOFeAs where Re are rare earth elements such as lanthanum (La) or gadolinium (Gd). Shortly after the discovery of superconductivity in LaOFeAs, superconductivity in $BaFe_2As_2$ was realized via hole doping by Rotter *et al.* [12]. $BaFe_2As_2$ is a member of the second class of iron pnictides, namely the 122 pnictides which do not contain oxygen. Superconductivity up to high temperatures can also be found in compounds where the alkaline earth metal barium (Ba) is replaced by calcium (Ca) [13] or strontium (Sr) [14].

All compounds consist of negatively charged FeAs layers, which alternate with positively charged layers depending on the corresponding parent compound. As an example, the schematic structures of $LaO_{1-x}F_xFeAs$ and $BaFe_2As_2$ are shown in Fig. 2.1. Thus, it is very likely that the two dimensional physics of these layers plays an important role. The situation has similarities to the one of the cuprates, but the exchange between the layers in the iron pnictides is much larger than in the cuprates [15]. Consequently, the magnetism in the iron pnictides is rather of three than of two dimensional nature. This will be confirmed by our results below.

In both classes, the system undergoes a structural and magnetic phase transition when it is cooled down. At first, the in-plane lattice constants (a, b) become unequal and the crystal structure changes from a tetragonal to an orthorhombic structure. Afterwards, a long-range antiferromagnetic order sets in. In contrast to the 1111 pnictides [17, 18], both transitions happen at the same temperature in the 122 compounds and cannot be distinguished [19, 20]. Typical *Néel temperatures*, where the

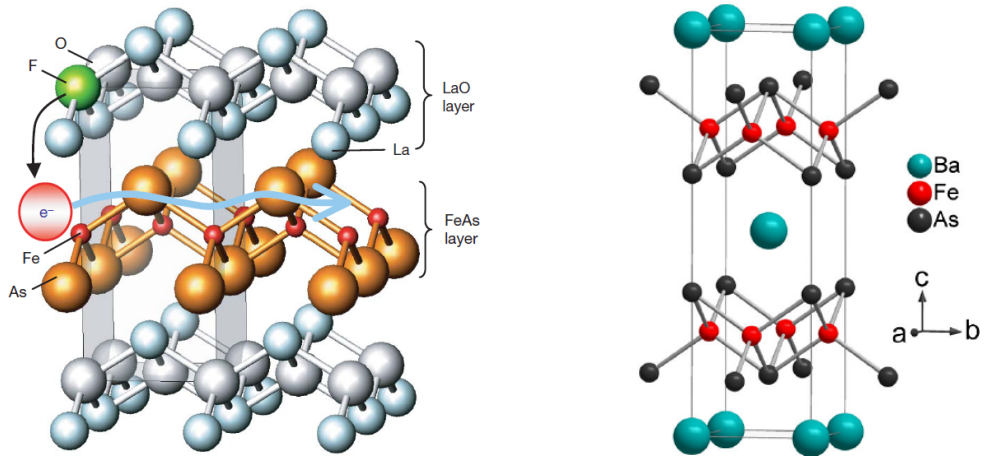

(a) $LaO_{1-x}F_xFeAs$ (Figure taken from Ref. [16])

(b) $BaFe_2As_2$ (Figure taken from Ref. [12])

Fig. 2.1.: Schematic crystal structure of doped $La_{1-x}F_xFeAs$ and the parent compound $BaFe_2As_2$.

collinear order sets in, are located in the range of $T_N \sim 100 - 200$ K. Above T_N, the compounds are paramagnetic.

The magnetic long-range order is a striped phase where the spins of the irons show an antiferromagnetic order in a-direction and a ferromagnetic order in b-direction (see Fig. 2.2). Between the layers (c-direction), the spins are also aligned antiparallel [9, 10]. Hence, the magnetic ordering vector of the three dimensional phase reads $Q = (1, 0, 1)$. For simplicity, the reciprocal lattice vectors are denoted in units of $\pi/$(lattice constant) where the lattice constants are the lattice constants of the orthorhombic/tetragonal lattice formed by the iron ions. The experimental results agree with theoretical band structure calculations, which show that the striped phase is the most stable one [21, 22].

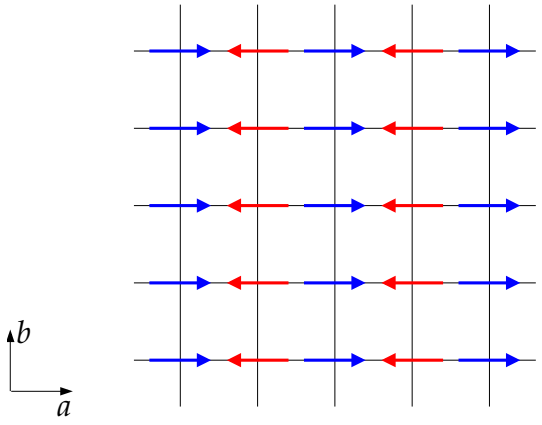

Fig. 2.2.: Schematical order of the spins of the irons in an FeAs layer.

The long-range ordered magnetic phase is located in the vicinity of the superconducting phase. Upon doping the parent compounds, superconductivity emerges and the magnetic long-range order is suppressed [23]. In the phase diagram in Fig. 2.3, even a coexistence of superconductivity and magnetic long-range order can be observed [7].

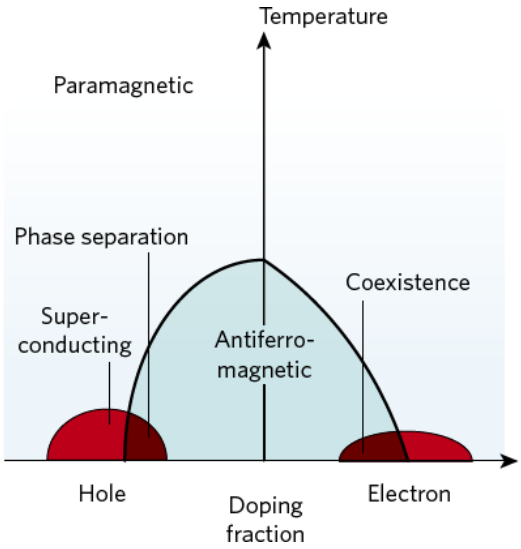

Fig. 2.3.: Schematic phase diagram for the 122 pnictides (Figure taken from Ref. [7]).

As an example of doping, the oxygen ions in LaFeAsO are substituted with fluoride ions (F^-), which increases the concentration of electrons in the FeAs layer [1], see Fig. 2.1a. For optimal doping, the critical temperature increases up to $T_c \sim 26$ K. By additionally applying a static pressure of 4 GPa, the critical temperature can be increased up to $T_c \sim 43$ K [16]. In case of the 122 pnictides, superconductivity was first detected upon hole doping. By doping the Ba layer of $BaFe_2As_2$ with K^+ ions, Rotter *et al.* [12] determined a critical temperature $T_c \sim 38$ K. Furthermore, it is possible to directly dope the iron arsenide layers. Leithe-Jasper *et al.* [24] reported superconductivity up to $T_c \sim 20$ K under doping of the iron arsenide layer with electrons using cobalt. The 122 pnictides also show pressure-induced superconductivity without any doping [25, 26].

2.2. Why a strongly localized model?

In contrast to the undoped parent compounds of the copper-oxides, which are insulators, the iron pnictides can be regarded as bad metals [1]. Studies with localized as well with itinerant approaches have both been successful. Hence, the strength of the effective Coulomb repulsion is still under debate. In this section, we summarize experimental and theoretical arguments in favor and in disfavor of a localized model and motivate our choice of an extended Heisenberg model.

In general, the interaction in the pnictides seems to be less important than in the copper oxides. The success of density functional theory (DFT) underlines this argument. For the pnictides, the proper-

ties of the ground state are described quite well by DFT [6, 22, 27], which speaks in favor of a less important interaction. This is not the case for the stronger interacting copper oxides. [28]. In addition, perturbative calculations based on diagrammatic techniques were successful [29]. A less important Coulomb repulsion is also supported by X-ray data. Yang *et al.* [30] measured a value of $U \approx 2$ eV, which is moderate compared to the bandwidth $W \approx 4$ eV.

However, there are also several successful calculations with a Coulomb repulsion of the order of the bandwidth ($U \approx 2-4$ eV) [31, 32, 33]. Furthermore, the bandwidth of $W \approx 4$ eV results from all d-bands of the iron while the bandwidth of the individual d-bands is at most $W_{\text{ind}} \approx 2.8$ eV [34]. Thus, it is comparable or even smaller than the effective Coulomb repulsion. Another argument for a localized model is the kinetic energy. Measurements of the optical conductivity by Qazilbash *et al.* [35] showed that the kinetic energy of the electrons is reduced to half of the value obtained by band structure calculations with nearly free electrons. A strong interaction is also stressed by angle-resolved photoemission (ARPES) results [36]. While it was possible to explain the data for LaOFeP with results from band structure calculations using the local density approximation (LDA), it failed for LaOFeAs. For LaOFeP, the DFT data had to be renormalized by a factor of two. Even no qualitative agreement was found for LaOFeAs. Consequently, the interactions are more important in the iron pnictides based on arsenide than in those based on phosphorus. In addition, magnetic excitations are detected with neutron scattering experiments [9, 10] up to energies as high as 200 meV. The observed weak damping of the excitations is another argument in favor of a localized model.

A related question still under debate is the reduced size of the local magnetic moment. Neutron scattering studies determined a reduced staggered magnetic moment of (0.31-0.41)μ_B for LaOFeAs [17], (0.8-0.9)μ_B for the 122 pnictide $BaFe_2As_2$ [37], (0.90-0.98)μ_B for $SrFe_2As_2$ [20] and 0.8μ_B for $CaFe_2As_2$ [10, 15]. In contrast, theoretical band structure calculations determined much higher values, e.g. up to 2.3μ_B for LaOFeAs [38].

It was suggested that the reduction of the local moment is due to a strong frustration within a localized model [32], which drives the system in the vicinity of a quantum phase transition. Studies of the two dimensional collinear ordered phase within self-consistent spin wave theory by Uhrig *et al.* [11] confirmed this result. The situation with respect to the interlayer coupling is discussed in this thesis. Strong frustration is also in agreement with LDA calculations which indicate that the ratio of the exchange perpendicular to the spin stripes and the next nearest neighbor exchange follows the trend of $J_{1a}/J_2 \sim 2$ [34], which is also in agreement with recent neutron scattering studies [10]. Because the exchange between nearest and next nearest neighbor ions is mediated via the arsenic ions, they are both estimated to be of similar magnitude.

However, the local magnetic moment depends on many parameters, especially on the local electronic situation. In band structure calculations, the magnetic moment is extremely sensitive to the position of the arsenic ions.

All in all, there are many arguments pointing towards a localized model for studying the magnetic excitations in the iron pnictides. But we have to keep in mind that an itinerant approach is also justified.

2.3. The Heisenberg model

Based on the summary of the last section, it is certainly justified, though not undisputed, to consult a localized model for studying the magnetic excitations in the iron pnictides.

A simple, but very successful model for studying the kinetic and interacting properties of electrons on a crystal lattice is the *Hubbard model* [39, 40, 41]

$$H = -t \sum_{\langle i,j\rangle,\sigma} \left(c^\dagger_{i,\sigma} c_{j,\sigma} + \text{h. c.} \right) + U \sum_i c^\dagger_{i,\uparrow} c_{i,\uparrow} c^\dagger_{i,\downarrow} c_{i,\downarrow} - \mu \sum_{i,\sigma} c^\dagger_{i,\sigma} c_{i,\sigma} \,, \tag{2.1}$$

where the fermionic operators $c^\dagger_{i,\sigma}, c_{i,\sigma}$ create (annihilate) an electron with spin $\sigma \in \{\uparrow, \downarrow\}$. The parameter t is the hopping integral, $U > 0$ the Coulomb repulsion and μ the chemical potential. For simplicity, the sums have already been restricted to nearest neighbor sites (N.N.) on a lattice with arbitrary dimension, which is indicated by the brackets $\langle i, j\rangle$.

In case of very strong repulsion $U \to \infty$ and at half filling, it is generally acknowledged that the Hubbard model is mapped to the antiferromagnetic *Heisenberg model* in second order perturbation theory in the hopping t

$$H = J \sum_{i,j} \mathbf{S}_i \cdot \mathbf{S}_j, \tag{2.2}$$

where $\mathbf{S}_{i,j}$ are the spin vector operators and $J > 0$ the exchange constant, which is related to the parameters of the Hubbard model via $J = 4t^2/U$. The Hamiltonian (2.2) is SU(2) symmetric. In general, the eigenvalue S of the spin operators in (2.2) can adopt any value $S = 0, 1/2, 1, 3/2, \ldots$.

For the iron pnictides, the possible values of the spin are $S = 0, 1, 2$ because Fe^{2+} has got an even number of electrons in its outer shell. According to Hund's rules, the maximum spin $S = 2$ should be realized. But this would result in a too strong local moment for the iron pnictides. For $S = 0$, the local moment is too small compared to the measured moment. Hence, $S = 1$ is an appropriate choice for the iron pnictides [11].

In addition, it has already been shown by Reischl *et al.* [42] that the two dimensional Hubbard model in the vicinity of half filling can be mapped on generalized *t-J* models when the interaction is comparable to the bandwidth or larger. Therewith, the charge degrees of freedom are included, which lies beyond this thesis.

In the antiferromagnetic Heisenberg model, the classical ground state at $T = 0$ is the so called Néel order, where the lattice separates into two bipartite sublattices A and B. Two spins on different sublattices are orientated antiparallel. Within one sublattice, all spins are aligned parallel, which is indicated by the same color in Fig. 2.4a. An interaction only exists between spins on two different sublattices, not within one sublattice. The classical ground state in Fig. 2.4a is not a true eigenstate of the Hamiltonian (2.2) because of quantum mechanical zero-point fluctuations.

For $J < 0$, all spins are aligned parallel at $T = 0$ and the Hamiltonian (2.2) describes the ferromagnetic Heisenberg model (Fig. 2.4b). For a ferromagnet, the classical ground state is identical to the quantum mechanical ground state.

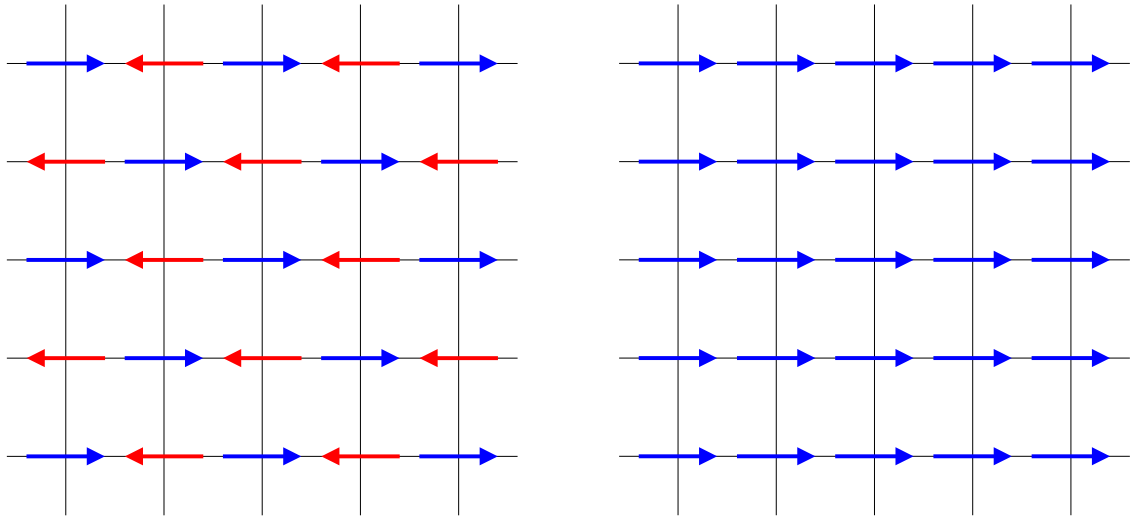

(a) Antiferromagnetic: $J > 0$ (Néel order). **(b)** Ferromagnetic: $J < 0$.

Fig. 2.4.: Classical ground states of the Heisenberg model.

2.4. Collective magnetism

2.4.1. Spontaneous symmetry breaking

We add an external ordering magnetic field $h > 0$ along the z-direction to the Hamiltonian (2.2)

$$H(h) = H - hS_k^z, \tag{2.3}$$

where S_k^z is the Fourier transform of the spin operator in momentum space according to A.2a and k the wave vector. For convenience, vectors in real and momentum space are not branded with arrows or printed in bold. Under the influence of the magnetic field, the spins are aligned along the field which is characterized by the magnetization per site

$$m_k(h) = \frac{1}{NZ} \operatorname{Tr}\left(\mathrm{e}^{-\beta H} S_k^z\right). \tag{2.4}$$

N is the number of lattice sites, $\beta = 1/T$ the inverse temperature and Z the canonical partition function. In general, units are used in this thesis where $\hbar = k_b = 1$.

The system experiences a spontaneous symmetry breaking if

$$\lim_{h \to 0^+} \lim_{N \to \infty} m_k(h, N, T) \neq 0, \tag{2.5}$$

which implies a finite magnetization in the thermodynamic limit of the system in the limit of the vanishing ordering field h. Singularities can only be observed in the thermodynamic limit, so the order of the limits in (2.5) is crucial.

Consequently, the system has less symmetry than the studied Hamiltonian itself. For the Heisenberg model (2.2), a preferred orientation of the spins exists which breaks the rotational symmetry. The non-vanishing magnetization in the limit of $h \to 0^+$ is called *spontaneous magnetization*. In an antiferromagnet, the spontaneous magnetization alternates from site to site, but its absolute value is identical in both sublattices. In contrast to the ferromagnet, this so called *spontaneous staggered magnetization* is always smaller than S because of quantum mechanical zero-point fluctuations. These quantum mechanical fluctuations are discussed in this thesis. At finite temperatures, the magnetization is additionally reduced by thermal fluctuations.

Without an ordering field, spontaneous broken symmetry is characterized by the two point correlation function (spin-spin correlation), which implies true long-range order when the symmetry is broken.

2.4.2. Mermin and Wagner's theorem

Mermin and Wagner's theorem [43] specifies the conditions under which a spontaneously symmetry breaking can be excluded.

We consider the quantum Heisenberg model

$$H = \frac{1}{2}\sum_{i,j} J_{ij}\,\mathbf{S}_i \cdot \mathbf{S}_j - hS_k^z, \tag{2.6}$$

where the interaction is of short-range so that

$$\bar{J} = \frac{1}{2N}\sum_{i,j} |J_{ij}||r_i - r_j|^2 < \infty. \tag{2.7}$$

Then there is no spontaneously broken symmetry at finite temperatures in one and two dimensions.

The proof can be found in Mermin and Wagner's letter [43]. Furthermore, it can be extended to other models which show a continuous symmetry. The theorem does not make any statement at zero temperature in one and two dimensions. In fact, one finds that there is no long range order in the antiferromagnetic Heisenberg chain at $T = 0$. In contrast, the ground state of the two dimensional system has long range order at zero temperature [44].

For finite temperatures, three is the lowest dimension where a spontaneous broken symmetry can be expected. The broken symmetry persists up to a critical temperature T_{crit}, where the magnetic ordering vanishes due to thermal fluctuations. For an antiferromagnet, this temperature is called *Néel temperature* T_N, while it is called *Curie temperature* T_C for a ferromagnet. At the critical temperature, the systems undergo a phase transition to a paramagnet.

However, the restrictions of Mermin and Wagner's theorem do not affect our studies, since we study two and three dimensional systems at zero temperature.

2.4.3. Goldstone's theorem

A consequence of the spontaneously broken symmetry of a Hamiltonian with short-range interaction are bosonic excitations without energy gap, which are the famous *Goldstone modes*. For example, *acoustic phonons* are the Goldstone bosons for a broken translational symmetry of the lattice. For the Heisenberg model (2.2), the rotational spin symmetry is broken and the corresponding Goldstone modes are *spin waves* or *magnons*.

Goldstone's theorem was originally formulated for relativistic field theories, where the excitations are massless. The non-relativistic version of Goldstone's theorem was proven by Lange [45].

Outgoing from Mermin and Wagner's theorem, we study a Hamiltonian

$$H = \frac{1}{2} \sum_{i,j} J_{ij} \, \mathbf{S}_i \cdot \mathbf{S}_j, \tag{2.8}$$

with short-range interaction

$$\bar{J} = \frac{1}{2N} \sum_{i,j} |J_{ij}| \, |r_i - r_j|^2 < \infty. \tag{2.9}$$

When the equal-time correlation function

$$S\left(k\right) = \frac{1}{N} \left\langle S_k^z S_{-k}^z \right\rangle \tag{2.10}$$

diverges at a wave vector Q

$$\lim_{k \to Q} S\left(k\right) \to \infty, \tag{2.11}$$

there exists a Goldstone mode with wave vector k and its excitation energy becomes gapless at Q:

$$\lim_{k \to Q} E\left(k\right) = 0. \tag{2.12}$$

Of great importance is the corrolary, which states that in case of spontaneously broken symmetry Goldstone modes exist. The converse of the theorem is not true, e.g. there are systems with gapless excitations which do not have a spontaneously broken symmetry.

Different from the ferromagnet, the antiferromagnet has two gapless modes which are located at $Q = (0, 0, \ldots)$ and $Q = (1, 1, \ldots)$. The latter one is the magnetic ordering vector of the Néel phase.

2.4.4. Spin waves

As mentioned before, spin waves or magnons are the Goldstone bosons of the Heisenberg model. This insert gives an idea how a magnon can be interpreted. For simplicity, we now restrict ourselves to the case of the ferromagnet. We also do not distinguish between spin wave and magnons. Both terms could be distinguish by identifying the magnon as the quantized spin wave.

A single magnon state, characterized by its momentum k, is a superposition of all possible states where the quantum number of S_i^z acting on lattice site i is reduced by one. For $S = 1/2$, the spin is flipped (Fig. 2.5). In total, this leads to a total spin deviation of one for the complete lattice with N sites. Thus, the average spin deviation from S at each site is $1/N$. This can be interpreted as a collective excitation where the spin deviation of one is distributed over the whole lattice.

In a semi-classical model (Fig. 2.6), the spins are interpreted as vectors precessing around the z-axis. Their projection onto the z-axis is $S - 1/N$. The phase shift from site to site is defined by the momentum $k = 2\pi/\lambda$. Hence, they define a wave.

In an antiferromagnet, the spins on different sublattices precess in opposite directions.

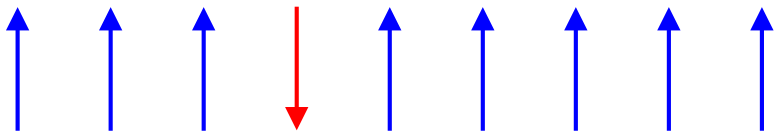

(a) $S = 1/2$

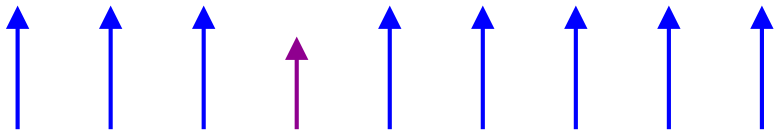

(b) $S > 1/2$

Fig. 2.5.: Ferromagnetic states with one excitation.

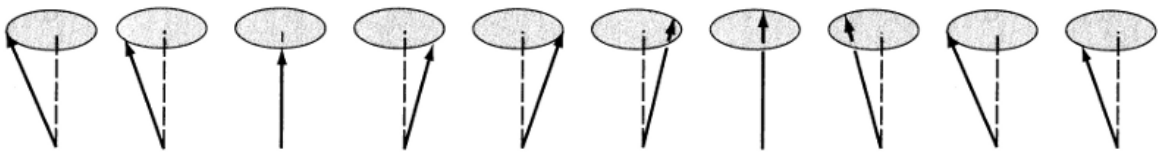

Fig. 2.6.: Semi-classical picture of a spin wave (Figure taken from Ref. [46]).

2.5. Frustration

A frustration of spins with an antiferromagnetic coupling can be induced in different ways. On the one hand, it might be caused by the lattice topology, for example on the triangular lattice (Fig. 2.7a). If two spins are perfectly aligned antiparallel, the third one is frustrated because it is not possible for the spin to align itself antiferromagnetically to both other spins at the same time. Consequently, the classical ground state energy cannot be optimally minimized.

On the other hand, additional exchange constants can be introduced. For our purposes, we introduce a next nearest neighbor coupling between the iron spins on the square lattice (Fig. 2.7b). The Hamiltonian then reads

$$H = J_1 \sum_{\langle i,j \rangle} \mathbf{S}_i \cdot \mathbf{S}_j + J_2 \sum_{\langle\langle i,j \rangle\rangle} \mathbf{S}_i \cdot \mathbf{S}_j, \tag{2.13}$$

where $J_{1,2} > 0$ are the exchange constants and the newly introduced double brackets $\langle\langle i, j \rangle\rangle$ indicate a summation over all next nearest neighbor (N.N.N.) sites. For $J_2 < 0$, no frustration is present. Hence, frustration always depends on the lattice topology and the signs of the couplings.

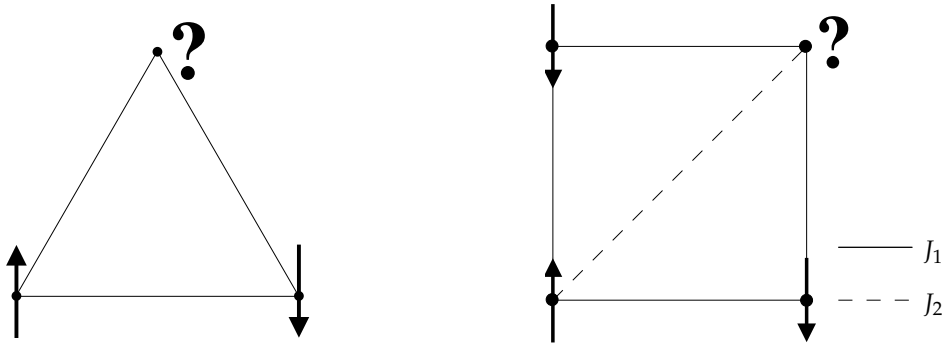

(a) Triangular lattice. **(b)** Square lattice.

Fig. 2.7.: Frustrated spins with antiferromagnetic couplings $J_{1,2} > 0$.

2.6. The J_1-J_2 Heisenberg model & the collinear phase

The J_1-J_2 Heisenberg model (2.13) and its ground states have been of general interest in research. The ground state of the simple Heisenberg model with $J_2 = 0$ on the square lattice is the Néel order which is reduced by quantum fluctuations (classical ground state see Fig. 2.4a). For $J_2 \neq 0$, the ground state depends on the ratio J_2/J_1 of the couplings. With increasing J_2/J_1, the Néel phase is destabilized. It persists up to a critical value where the system becomes unstable and undergoes a phase transition to a quantum disordered state. The intermediate phase is stable in the range of $0.4 \lesssim J_2/J_1 \lesssim 0.6$ and

is dominated by short-range singlet (dimer) formation [47, 48]. For $J_2/J_1 > 0.6$, the spins arrange in a collinear pattern (see Fig. 2.2). In the classical limit $S \to \infty$, the transition between the Néel and collinear order occurs at $J_2/J_1 = 0.5$.

Singh *et al*. [49] studied the excitation spectra of the collinear phase with series expansion and mean field spin wave theory. They calculated the spin wave velocities which depend heavily on the coupling ratio J_2/J_1. Gapless excitations were only found at $k = (0,0)$ and $k = (1,0)$, while the modes at $k = (0,1)$ and $k = (1,1)$ are gapped because of the order by disorder effect. In contrast to Mermin and Wagner's theorem, it was proposed by Chandra *et al*. [50] that the spontaneously broken symmetry can survive up to finite temperatures in two dimensions. No evidence for a phase transition at finite temperatures was found by Sing *et al*., insted they proposed a scenario for a zero temperature transition based on quantum fluctuations. However, later studies by Capriotti *et al*. [51] reported an Ising-type phase transition at finite temperatures for every value of the spin when the system is in the collinear phase.

Furthermore, Shannon *et al*. [52] studied the J_1-J_2 Heisenberg model with competing ferromagnetic and antiferromagnetic exchange. They reported an additional instability at $J_1 \approx -2J_2$, where the system undergoes a phase transition from the collinear ordered state to a ferromagnetic state.

For the application to iron pnictides, the spin wave excitations in the collinear phase have been studied in two dimensions by Yao and Carlson [53]. Their analysis does not include the effect of quantum fluctuations. Thus, they also find gapless excitations at the conventional Néel magnetic ordering vector $Q = (1,1)$ and at $Q = (0,1)$. In their second paper [54], they studied the magnetic excitations in the three dimensional collinear phase with ab-initio anisotropic in-plane exchange constants J_{1a} and J_{1b}.

The spin wave spectra of the two dimensional J_{1a}-J_{1b}-J_2 model were also studied with series expansion techniques [55] by Applegate *et al*. [56].

Attempts with spin wave approximation and in part with exact diagonalization methods for the J_{1a}-J_{1b}-J_2 model were recently made by Schmidt *et al.* [57]. According to their results, a strong reduction of the local moment due to quantum fluctuations can be excluded.

2.7. Biquadratic exchange

In this section, we discuss the evidence for an additional biquadratic exchange in the Heisenberg model (2.2) for $S \geq 1$, which reads

$$H_{\mathrm{bq}} = -J_{\mathrm{bq}} \sum_{\langle i,j \rangle} \left(\mathbf{S}_i \cdot \mathbf{S}_j \right)^2 \tag{2.14}$$

with $J_{\mathrm{bq}} > 0$. Together with the usual bilinear terms, the biquadratic term induces an anisotropy in the effective exchange constants between ferromagnetic and antiferromagnetic ordered spins.

2.7.1. Anisotropy

In Section 2.1, it has already been mentioned that the iron pnictides undergo a structural phase transition to an orthorhombic structure, which means that the lattice constants a and b of the collinear ordered layers (see Fig. 2.2) become inequivalent. The orthorhombic distortion is less than 1% [9, 37]. In contrast, a large anistropy between the exchange constants parallel and perpendicular to the spin stripes is required to fit a frustrated Heisenberg model to spin wave dispersions measured by inelastic neutron scattering (INS) [9, 10]. The exchange perpendicular to the spin stripes J_{1a} is much stronger than the exchange parallel to stripes J_{1b}, which can even be negative [10]. Due to the very small lattice distortion, a significant deviation in the in-plane nearest neighbor exchange constants parallel and perpendicular to the spin stripes is rather unlikely and an ab-initio introduction of anisotropic exchange constants cannot be justified.

Thus, the anisotropy has to be caused by other mechanisms. One plausible origin is a biquadratic exchange between nearest neighbor sites. Consistently, the biquadratic exchange also has to be introduced between next nearest neighbor sites because there is no reason why it should not be important for the interaction between next nearest neighbors when it is important for the interaction between nearest neighbors. However, we only discuss the biquadratic exchange between nearest neighbor sites in this thesis.

2.7.2. DFT results

Evidence for biquadratic exchange has already appeared in self-consistent LSDA (local spin-density approximation) calculations by Yaresko *et al.* [22]. They obtained DFT results for the energy dependence on the angle between the magnetic moments of nearest neighbor ions. The results for $BaFe_2As_2$ and LaOFeAs are are shown in Fig. 2.8. The angle α is measured relatively between the moments of the ions. The dependence of $E(\alpha) = A \cdot \sin^2 \alpha$ on α is a typical fingerprint of a biquadratic terms. A term $\sim \sin^2 \alpha$ does not appear in the frustrated J_1-J_2 Heisenberg model. The classical energy per spin in dependence of the angle α for a biquadratic exchange term (2.14) reads

$$E(\alpha) = 2J_{\mathrm{bq}} \sin^2 \alpha, \tag{2.15}$$

which is simply derived by treating the spins as classical vectors. Thereby, appropriate values for the biquadratic exchange are determined by the maximum $E(\alpha = 90^\circ)$ in Fig. 2.8. The obtained values are

$$J_{\mathrm{bq}} = 21.5 \text{ meV for LaOFeAs},$$
$$J_{\mathrm{bq}} = 10.1 \text{ meV for } BaFe_2As_2.$$

Yaresko *et al.* also performed spin spiral calculations. The magnetic moment in the a-b-plane rotates upon a lattice translation $\mathbf{t}$ by an angle

$$\varphi(t) = \pi \, \mathbf{k} \cdot \mathbf{t}. \tag{2.16}$$

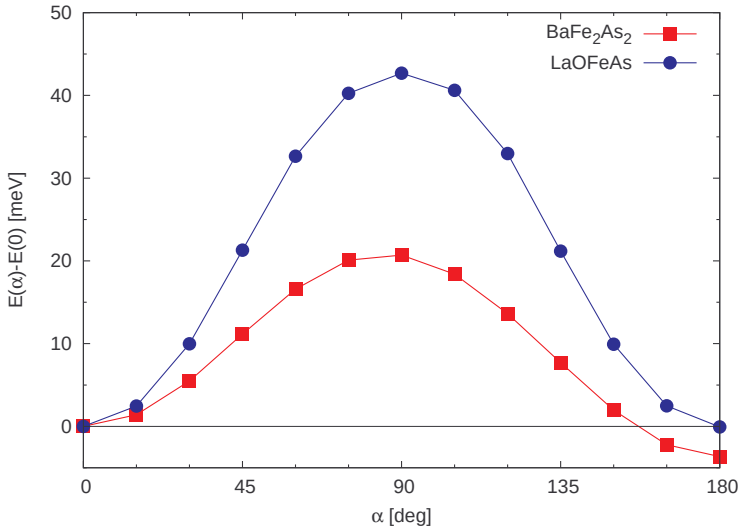

Fig. 2.8.: Dependence of the energy on the relative angle α between the magnetic moments of nearest neighbor ions. The data was provided by A.N. Yaresko [58].

In this section, vectors are printed in bold for clarity. Their DFT results of the total energy show that the collinear ordered phase $\mathbf{k} = (k_a, k_b) = (1, 0)$ is the global minimum of the total energy. By applying the definition of spin spirals to classical vectors, the classical energy per spin as a function of the wave vector $\mathbf{k} = (k_a, k_b)$ for the J_1-J_2 Heisenberg model (2.13) can be derived as

$$E\left(k\right) = J_1\left(\cos k_a + \cos k_b\right) + 2J_2 \cos k_a \cos k_b - E\left(0\right). \tag{2.17}$$

In Fig. 2.9, the total energy calculated by Yaresko *et al.* is shown along with fits to (2.17). The J_1-J_2 Heisenberg model describes the main aspects of the total energy quite well, but it cannot catch all details.

Fits of the classical energy of the J_1-J_2 Heisenberg model (2.13) with an additional biquadratic exchange (2.14)

$$E\left(k\right) = J_1\left(\cos k_a + \cos k_b\right) + 2J_2 \cos k_a \cos k_b - J_{\mathrm{bq}}(\cos^2 k_a + \cos^2 k_b) - E\left(0\right) \tag{2.18}$$

to the total energy appeared to be insufficient because the shape of the total energy can only be reproduced properly for $J_{\mathrm{bq}} \sim -1$ meV, which is too small compared to Fig. 2.8. In addition, the results are very ambiguous and depend strongly on the choice of the initial values of the exchange constants because as many as four fitting parameters are required. Two examples are presented in Fig. 2.10.

However, by combining the results of the total energy (Fig. 2.9) and the angle dependence (Fig. 2.8) we see that biquadratic exchange seems to be important. According to our analysis, we obtain a ratio of $J_{\mathrm{bq}}/J_1 \approx 0.5$ which shows that the biquadratic exchange is of significant size. A strong biquadratic exchange for the iron chalcogenide FeSe was recently reported by Pulikkotil *et al.* [59]. According to their results, a similar behavior was also found for other pnictides.

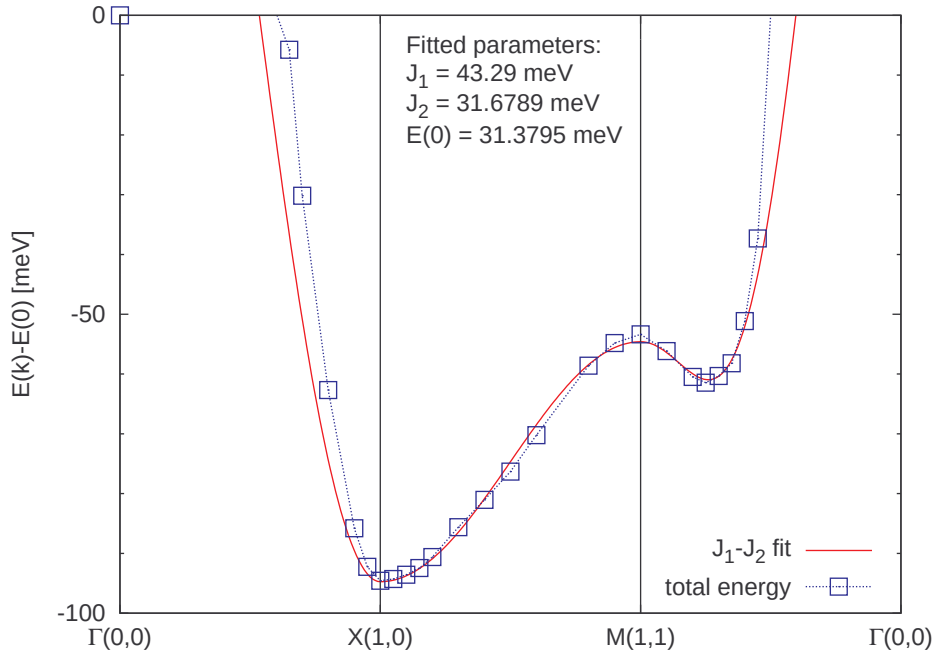

(a) LaOFeAs

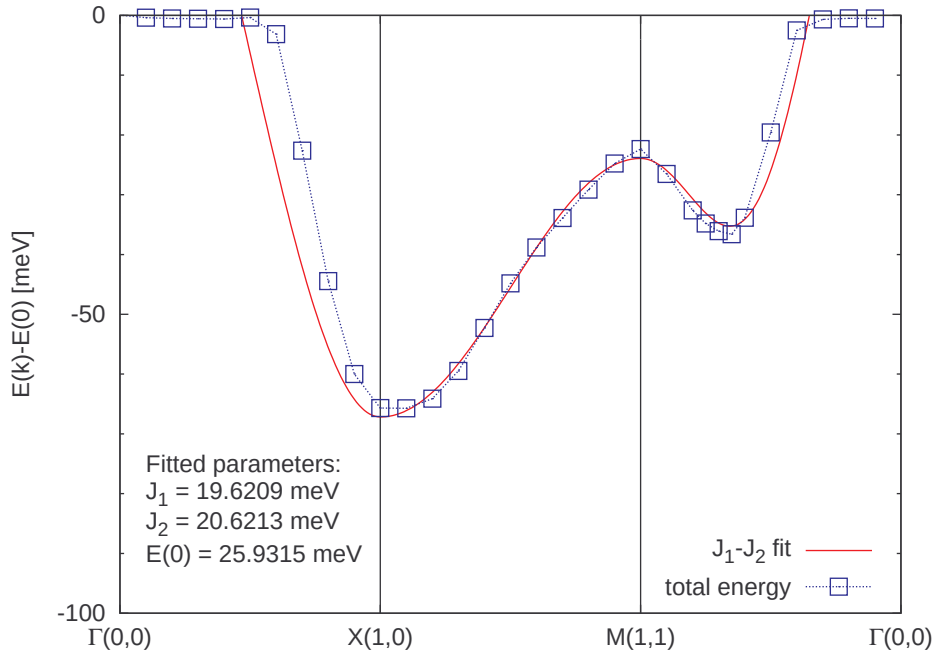

(b) $BaFe_2As_2$

Fig. 2.9.: Total energy as a function of the wave vector obtained from spin spiral calculations and fits to the classical J_1-J_2 Heisenberg model. The total energies were provided by A.N. Yaresko [58].

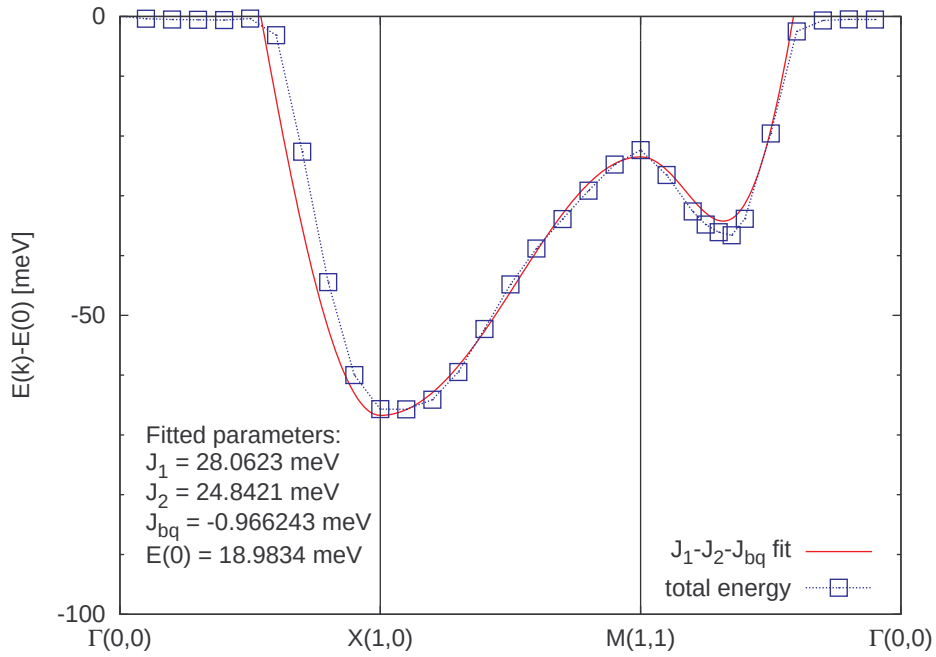

(a) The determined value of J_{bq} is too small compared to Fig. 2.8.

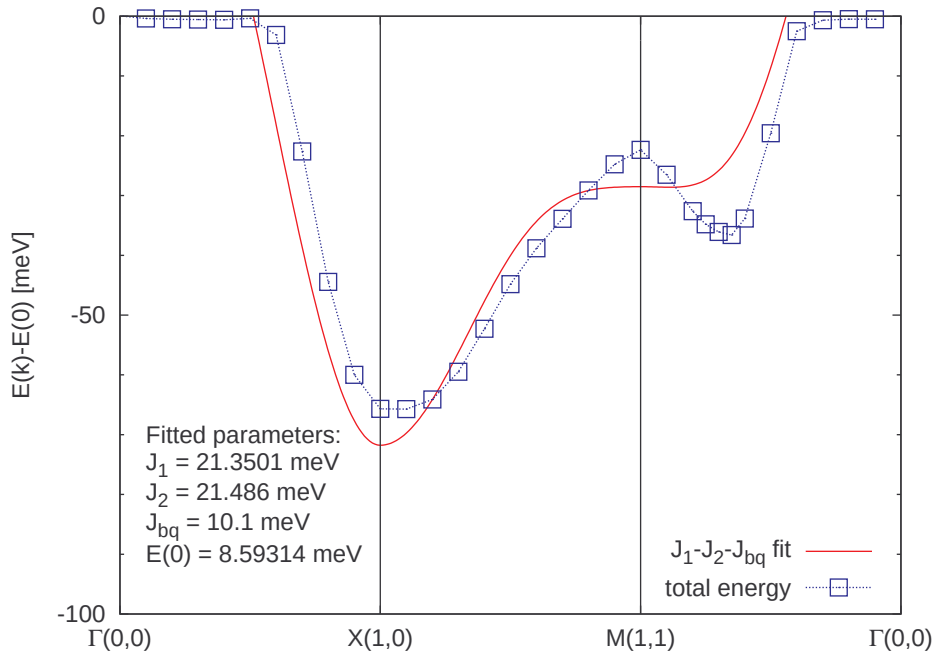

(b) Fit with fixed value of $J_{bq} = 10.1$ meV taken from the calculation of the angle dependence (see Fig. 2.8). The obtained fit does not reproduce the total energy in all details.

Fig. 2.10.: Total energy as a function of the wave vector obtained from spin spiral calculations for $BaFe_2As_2$ and fits to the classical J_1-J_2-J_{bq} Heisenberg model. The obtained exchange constants depend strongly on the initial values. The standard deviation of J_1, J_2 and E_0 is $\sim 10^{11}$-10^{13}. The total energies were provided by A.N. Yaresko [58].

2.7.3. Many-electron exchange

The electronic situation in the iron pnictides is very complex as up to five bands are important [27, 38, 22]. At least, two band models are necessary [60]. Hence, one is actually confronted with a many-electron exchange than with a single-electron exchange. For a many-electron exchange between nearest neighbor sites with $N > 1$ electrons in an unfilled atomic shell, it has already been shown that it leads to an Hamiltonian with bilinear and biquadratic exchange of similar magnitude [61].

2.8. Alternative approaches

The discovery of the high-temperature superconducting iron pnictides has lead to an enormous research activity in theoretical and experimental physics.

During our justification of a localized model in Section 2.2 it was clear that also an itinerant approach is supported by experimental results. Thus, the nature of the magnetism in the iron pnictides is not completely clarified by now.

In stark contrast to our localized starting point, the magnetism can be caused by the itinerant band electrons. The situation can be described by an extended multi-band Hubbard model with at least two bands. In this scenario, the interaction between the electrons is small compared to the bandwidth and only the electrons close to the Fermi surface are important. Hence, the interaction can be treated as a small perturbation and diagrammatic techniques can be applied. In the limit of weak interaction, a nesting of the Fermi surface leads to a spin-density wave (SDW) instability from which the magnetism originates [29, 62, 63, 64, 65].

Furthermore, the success of localized as well as itinerant approaches may point towards a combination of both approaches, which was shown recently by Lv *et al.* [66]. They studied a model where the local moments are described by a strongly frustrated Heisenberg model. In addition, the itinerant electrons of the degenerate d_{xz} and d_{yz} bands are included. The local moments and itinerant electrons are coupled by a ferromagnetic Hund's coupling. Under the influence of super- and double-exchange via the As^{+} ions, the calculated spin wave dispersion is fitted to an effective Heisenberg model with effective exchange constants parallel and perpendicular to the spin stripes which show a very strong anisotropy. It is even possible to obtain a ferromagnetic exchange parallel to the stripes. Therewith, they are able to reproduce the spin wave dispersion measured by Zhao *et al*. [10].

3. Spin wave theory

Our main objective is to diagonalize Hamiltonians based on the Heisenberg model (2.2) to obtain the spin wave dispersion. Since spin waves or magnons are bosonic excitations, it is self-evident to replace the spin operators by expressions of bosonic operators.

Therefore, the spin operators S^x and S^y are written in terms of spin ladder operators

$$S_i^+ = S_i^x + iS_i^y \tag{3.1a}$$
$$S_i^- = S_i^x - iS_i^y. \tag{3.1b}$$

Consequently, the Hamiltonian (2.2) is given by

$$H = J \sum_{\langle i,j \rangle} \left[S_i^z S_j^z + \frac{1}{2} \left(S_i^+ S_j^- + S_j^+ S_i^- \right) \right]. \tag{3.2}$$

If there is an antiferromagnetic coupling between the spins on nearest neighbor sites, the lattice separates into two bipartite sublattices A and B and it is convenient to rotate all spins on sublattice B by an angle of π about the x-axis. Then we have $\forall\, i \in B$

$$S_i^+ \rightarrow S_i^- \tag{3.3a}$$
$$S_i^- \rightarrow S_i^+ \tag{3.3b}$$
$$S_i^z \rightarrow -S_i^z \tag{3.3c}$$

and the Hamiltonian for the antiferromagnet reads

$$H = J \sum_{\langle i,j \rangle} \left[-S_i^z S_j^z + \frac{1}{2} \left(S_i^+ S_j^+ + S_j^- S_i^- \right) \right]. \tag{3.4}$$

The replacement of the spin ladder operators can be realized by many different representations. The next section introduces three of them.

In addition, a general expression for the dynamical structure factor is derived, which is evaluated afterwards within the Dyson-Maleev representation for the collinear ordered phase. The decision for this representation is based on an anticipated result from Chapter 4. There, we apply both, the Dyson-Maleev and Schwinger bosons representation to the antiferromagnetic Heisenberg model with biquadratic exchange and compare our results with results from numerical calculations.

3.1. Spin representations

3.1.1. Holstein-Primakoff bosons

This widely acclaimed spin representation was introduced by Holstein and Primakoff in 1940 [67]. Originating from the symmetry broken phase, the components of the spin operator are expressed in terms of bosonic creation and annihilation operators $b_i^\dagger$ and b_i,

$$S_i^+ = \sqrt{2S - \hat{n}_i}\, b_i \tag{3.5a}$$

$$S_i^- = b_i^\dagger \sqrt{2S - \hat{n}_i} \tag{3.5b}$$

$$S_i^z = S - \hat{n}_i\,, \tag{3.5c}$$

where $\hat{n}_i = b_i^\dagger b_i$ is the occupation number operator on site i. It describes the deviation of the spin from its maximum value.

The operators conserve the spin commutation relations

$$\left[S^\alpha, S^\beta\right] = i \sum_\gamma \epsilon^{\alpha\beta\gamma} S^\gamma, \tag{3.6}$$

where $\epsilon^{\alpha\beta\gamma}$ is the totally antisymmetric tensor. Although the bosonic Hilbert space is actually infinite, the operators are constructed in a way that the physical subspace is never left. It contains $2S+1$ states with the bosonic occupation numbers $0, 1, \ldots, 2S$.

To obtain a Hamiltonian which only consists of terms with one, two, ... particle operators, the square roots in (3.5) have to be expanded in powers of $1/S$. This corresponds to an expansion in the semiclassical limit $S \to \infty$. Keeping the terms of $\mathcal{O}(S^2)$ and $\mathcal{O}(S)$ of the complete Hamiltonian, the Hamiltonian only contains constant terms and quadratic terms of bosonic operators. Consequently, the interaction between magnons is neglected. This method is called *linear spin wave theory*. The interaction between magnons first appears in $\mathcal{O}(1)$ of the Hamiltonian, which corresponds to $\mathcal{O}(1/S)$ in the expansion of the square root. Terms of this order and higher can be treated by a mean field approximation. Then, physical quantities such as the staggered magnetization or the spin wave velocities are renormalized due to fluctuations.

Holstein-Primakoff bosons are not going to be further investigated in this thesis. They are mentioned because of their widely acceptance and application. Furthermore, the dispersions used by experimentalists are usually derived from linear spin wave theory.

3.1.2. Dyson-Maleev representation

In the Holstein-Primakoff representation, the necessary expansion of the square root is the main obstacle. This is not the case in the following representation, which was introduced by Dyson [68, 69]

and Maleev [70]. The expression of the spin operators in terms of bosonic operators here reads

$$S_i^+ = b_i^\dagger \left(2S - \hat{n}_i\right) \tag{3.7a}$$
$$S_i^- = b_i \tag{3.7b}$$
$$S_i^z = -S + \hat{n}_i \,. \tag{3.7c}$$

Note that the operators S^+ and S^- are no longer manifest Hermitian conjugates in this spin representation, which may invoke unphysical results. As in the case of the Holstein-Primakoff bosons, the disadvantageous origin in the symmetry broken phase still persists. However, for the simple Heisenberg model (2.2) one only receives terms which are quadratic and quartic in the bosonic operators. The latter one can easily be treated within a mean field approximation, which consequently leads to a *renormalized* or *self-consistent spin wave theory*.

For an antiferromagnet with two bipartite lattices, the representation on sublattice B reads

$$S_i^+ = b_i^\dagger \tag{3.8a}$$
$$S_i^- = \left(2S - \hat{n}_i\right) b_i \tag{3.8b}$$
$$S_i^z = -S + \hat{n}_i \,, \tag{3.8c}$$

after a π-rotation of the spins around the x-axis.

In addition, it is possible to regard diagrams of higher orders. For example, the ground state energy of the Heisenberg antiferromagnet has been calculated in fourth order by Weihong and Hamer [71].

3.1.3. Schwinger bosons

In this representation, there are two *Schwinger bosons* a and b at each lattice site. Therewith, the spin operators can be expressed as

$$S_i^+ = a_i^\dagger b_i \tag{3.9a}$$
$$S_i^- = b_i^\dagger a_i \tag{3.9b}$$
$$S_i^z = \frac{1}{2}\left(a_i^\dagger a_i + b_i^\dagger b_i\right). \tag{3.9c}$$

The constraint

$$a_i^\dagger a_i + b_i^\dagger b_i = 2S \tag{3.10}$$

guarantees that the physical subspace is never left. It is illustrated in Fig. 3.1. Consequently, the Schwinger bosons of type a stand for positive eigenvalues of S^z, whereas the bosons of type b stand for negative eigenvalues. The ladder operators also satisfy the commutator relation (3.6).

In case of the Heisenberg model (2.2), one only obtains quartic terms of bosonic operators. Within a mean field theory, they yield two independent excitations per lattice site. In contrast to the representations mentioned before, the Schwinger bosons do not single out a specific spin direction. So they can also be used to describe the symmetric phases, which is a clear advantage.

Furthermore, the representation can easily be extended up to $\mathcal{N}$ boson flavors. The mean field theory is then derived as an expansion in $1/\mathcal{N}$ [44].

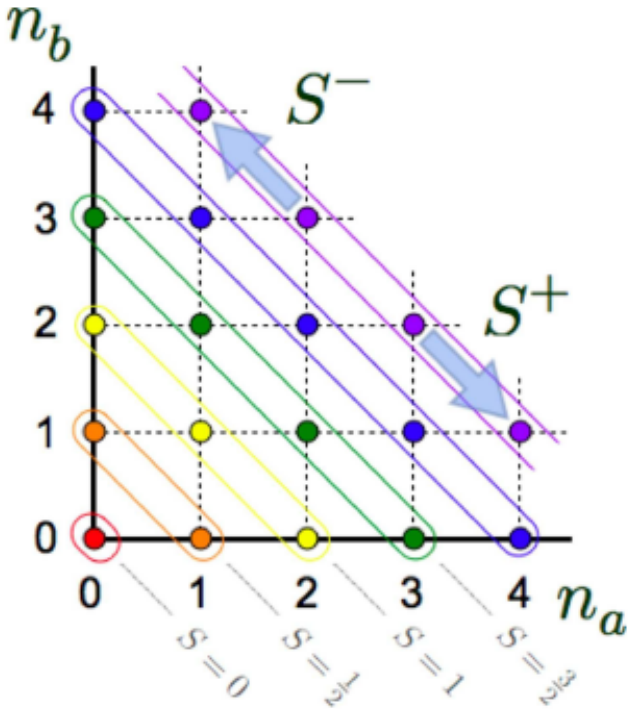

Fig. 3.1.: Illustration of Schwinger bosons and the constraint of SU(2) (Figure taken from Ref. [72]).

3.2. Dynamical structure factor

The most important experimental method for investigating spin waves is inelastic neutron scattering. Consequently, it is very useful to compare the measured scattering intensities with theoretical predictions. The neutron cross section is proportional to the dynamical structure factor $S_T^{\alpha\beta}(k,\omega)$ [73], which can be calculated within our theory.

In this section, we derive a general expression for the dynamical structure factor. Its inelastic part is then evaluated within the Dyson-Maleev formalism for a lattice, which decomposes into two bipartite sublattices A and B. In the upcoming chapter 4, it is proven that the Dyson-Maleev representation works best for our purposes.

3.2.1. General expression

At first, we start with the retarded dynamical susceptibility [73, 74]

$$\chi_T^{\alpha\beta}\left(k,\omega\right) = i\int\limits_{-\infty}^{\infty} \mathrm{d}t\, \mathrm{e}^{i\omega t} \sum_{r,r_0} \mathrm{e}^{-ik(r-r_0)} \left\langle \left[S_r^{\alpha}\left(t\right), S_{r_0}^{\beta}\left(t=0\right)\right] \right\rangle \Theta\left(t\right), \tag{3.11}$$

which is connected to the dynamical structure factor $S_T^{\alpha\beta}(k,\omega)$ via the relation

$$S_T^{\alpha\beta}\left(k,\omega\right) = \frac{1}{1-\mathrm{e}^{-\beta\omega}} \operatorname{Im}\chi_T^{\alpha\beta}\left(k,\omega\right). \tag{3.12}$$

The indices of the spin operators are $\alpha,\beta \in \{x,y,z\}$ and $\Theta(t)$ is the Heaviside function. For simplification, it has already been taken into account that the Hamiltonian is translational invariant and time independent.

The expectation value $\langle \ldots \rangle$ is given by the trace

$$\begin{aligned}\langle \ldots \rangle :=& \frac{1}{Z} \operatorname{Tr}\left(\mathrm{e}^{-\beta H} \ldots\right) \\ =& \frac{1}{Z} \sum_n \langle n| \mathrm{e}^{-\beta H} \ldots |n\rangle \\ =& \frac{1}{Z} \sum_n \mathrm{e}^{-\beta E_n} \langle n| \ldots |n\rangle,\end{aligned} \tag{3.13}$$

which is taken over the eigenbase of the Hamiltonian with $H|n\rangle = E_n|n\rangle$. $Z := \operatorname{Tr}(\mathrm{e}^{-\beta H})$ is the partition function of the system.

Because the Hamiltonian is time independent, the time evolution of $S_r^{\alpha}(t)$ in the Heisenberg picture reads

$$S_r^{\alpha}\left(t\right) = \mathrm{e}^{iHt}\, S_r^{\alpha}\, \mathrm{e}^{-iHt}. \tag{3.14}$$

All together, the susceptibility reads as follows

$$\begin{aligned}
\chi_T^{\alpha\beta}(k,\omega) &= i\int_0^\infty \mathrm{d}t\, \mathrm{e}^{i\omega t} \sum_{r,r_0} \mathrm{e}^{-ik(r-r_0)} \frac{1}{Z} \sum_n \mathrm{e}^{-\beta E_n} \\
&\quad \cdot \left[\langle n| \mathrm{e}^{iHt}\, S_r^\alpha\, \mathrm{e}^{-iHt}\, S_{r_0}^\beta |n\rangle - \langle n| S_{r_0}^\beta\, \mathrm{e}^{iHt}\, S_r^\alpha\, \mathrm{e}^{-iHt} |n\rangle \right] \\
&= \frac{i}{Z}\int_0^\infty \mathrm{d}t\, \mathrm{e}^{i\omega t} \sum_{r,r_0} \mathrm{e}^{-ik(r-r_0)} \sum_{n,m} \mathrm{e}^{-\beta E_n} \\
&\quad \cdot \left[\mathrm{e}^{i(E_n-E_m)t} \langle n| S_r^\alpha |m\rangle \langle m| S_{r_0}^\beta |n\rangle - \mathrm{e}^{i(E_m-E_n)t} \langle n| S_{r_0}^\beta |m\rangle \langle m| S_r^\alpha |n\rangle \right] \\
&= \frac{i}{Z}\int_0^\infty \mathrm{d}t\, \mathrm{e}^{i\omega t} \sum_{r,r_0} \mathrm{e}^{-ik(r-r_0)} \sum_{n,m} \mathrm{e}^{i(E_n-E_m)t} \\
&\quad \cdot \langle n| S_r^\alpha |m\rangle \langle m| S_{r_0}^\beta |n\rangle \left[\mathrm{e}^{-\beta E_n} - \mathrm{e}^{-\beta E_m} \right].
\end{aligned} \tag{3.15}$$

In the last step, n and m have been swapped in the second summand.

Next, the Fourier representation of the spin operators (A.2a) is inserted. The two sums in position space yield Dirac delta functions (A.4), which simplify the susceptibility to

$$\begin{aligned}
\chi_T^{\alpha\beta}(k,\omega) &= \frac{i}{Z}\int_0^\infty \mathrm{d}t\, \mathrm{e}^{i\left(\omega+i0^+\right)t} \sum_{n,m} \sum_{k',k''} \mathrm{e}^{i(E_n-E_m)t} \\
&\quad \cdot \langle n| S_{k'}^\alpha \delta(k-k') |m\rangle \langle m| S_{k''}^\beta \delta(k+k'') |n\rangle \left[\mathrm{e}^{-\beta E_n} - \mathrm{e}^{-\beta E_m} \right] \\
&= \frac{i}{Z}\int_0^\infty \mathrm{d}t \sum_{n,m} \mathrm{e}^{i\left(E_n-E_m+\omega+i0^+\right)t} \langle n| S_k^\alpha |m\rangle \langle m| S_{-k}^\beta |n\rangle \left[\mathrm{e}^{-\beta E_n} - \mathrm{e}^{-\beta E_m} \right].
\end{aligned} \tag{3.16}$$

To ensure the convergence of the integration in time, an infinitesimal positive number 0^+ has been inserted. After carrying out the integration, one obtains the expression

$$\begin{aligned}
\chi_T^{\alpha\beta}(k,\omega) &= -\frac{1}{Z}\sum_{n,m} \langle n| S_k^\alpha |m\rangle \langle m| S_{-k}^\beta |n\rangle \frac{\mathrm{e}^{-\beta E_n} - \mathrm{e}^{-\beta E_m}}{E_n - E_m + \omega + i0^+} \\
&= -\frac{1}{Z}\sum_{n,m} \langle n| S_k^\alpha |m\rangle \langle m| S_{-k}^\beta |n\rangle \left[\mathrm{e}^{-\beta E_n} - \mathrm{e}^{-\beta E_m} \right] \\
&\quad \cdot \left\{ \mathcal{P}\left(\frac{1}{E_n - E_m + \omega} \right) - i\pi\delta\left(E_n - E_m + \omega\right) \right\},
\end{aligned} \tag{3.17}$$

for the retarded dynamical susceptibility. In the last step, the identity

$$\frac{1}{x \mp i0^+} = \mathcal{P}\left(\frac{1}{x}\right) \pm i\pi\delta(x) \tag{3.18}$$

has been used to decompose $\chi_T^{\alpha\beta}$ into its real and imaginary part. $\mathcal{P}(1/x)$ denotes the principal value of $1/x$.

Inserting (3.17) in (3.12), a general expression for the dynamical structure factor is given by

$$S_T^{\alpha\beta}(k,\omega) = \frac{1}{1-\mathrm{e}^{-\beta\omega}} \frac{\pi}{Z} \sum_{n,m} \langle n| S_k^\alpha |m\rangle \langle m| S_{-k}^\beta |n\rangle \left[\mathrm{e}^{-\beta E_n} - \mathrm{e}^{-\beta E_m}\right] \delta(E_n - E_m + \omega) \ . \tag{3.19}$$

3.2.1.1. Limit of vanishing temperature

In the limit of $T \to 0$, the partition function can be approximated by

$$Z \approx \mathrm{e}^{-\beta E_0} \ , \tag{3.20}$$

as the ground state is the most important contribution for very low temperatures. Consequently, only terms with $n = 0$ or $m = 0$ contribute, which correspond to transitions from/to the ground state $|0\rangle$ (vacuum).

With $\omega_{n/m} = E_{n/m} - E_0$, the dynamical structure factor reduces to

$$\begin{aligned} S_T^{\alpha\beta}(k,\omega) = \frac{1}{1-\mathrm{e}^{-\beta\omega}} \pi \Bigg\{ & \sum_m \langle 0| S_k^\alpha |m\rangle \langle m| S_{-k}^\beta |0\rangle \, \delta(\omega - \omega_m) \\ & - \sum_n \langle n| S_k^\alpha |0\rangle \langle 0| S_{-k}^\beta |n\rangle \, \delta(\omega + \omega_n) \Bigg\} . \end{aligned} \tag{3.21}$$

The sums $\sum_{n,m}$ indicate a summation over all excited states with energy $\omega_{n/m}$ and momentum k. Hence, the indices m, n can also be replaced by the momentum k. The first term contributes for $\omega > 0$ and therefore corresponds to magnon emission processes, whereas the second one contributes for $\omega < 0$ and is connected to magnon absorption processes.

Furthermore, we restrict ourselves to the excitation of single magnons, as no excited states exist at $T = 0$. Thus, only terms with $\omega > 0$ contribute and the temperature dependent prefactor becomes unity in the limit of $T \to 0$.

3.2.2. Evaluation of the dynamical structure factor within the Dyson-Maleev representation

Our next aim is to calculate the dynamical structure factor within the Dyson-Maleev representation (3.7) and (3.8). The ladder operators S_i^+ on the A lattice and S_i^- on the B lattice can be simplified with the mean field approximation

$$S_i^+ = 2\,(S-n)\,b_i^\dagger \quad \text{for } i \in A \tag{3.22a}$$
$$S_i^- = 2\,(S-n)\,b_i \quad \text{for } i \in B, \tag{3.22b}$$

where $n := \langle b_i^\dagger b_i \rangle > 0$ is the average occupation number on each lattice site. The factor 2 is a consequence of Wick's theorem [75], because there are two possibilities to uncontract the operator

$$\begin{aligned} b_i^\dagger b_i^\dagger b_i &\approx \overbrace{b_i^\dagger b_i^\dagger} b_i + b_i^\dagger \overbrace{b_i^\dagger b_i} \\ &= 2n b_i^\dagger, \end{aligned}$$

so that all spin operators are now linear in $b_i^\dagger$ or b_i, respectively.

Now we have to derive the spin operators in momentum space. As the operators b_k and $b_k^\dagger$ are not in the basis of the diagonal Hamiltonian, they have to be transformed to new operators β_k and $\beta_k^\dagger$, using a bosonic *Bogoliubov transformation*

$$b_k = \beta_k \cosh\theta_k + \beta_{-k}^\dagger \sinh\theta_k \tag{3.23a}$$
$$b_k^\dagger = \beta_k^\dagger \cosh\theta_k + \beta_{-k} \sinh\theta_k. \tag{3.23b}$$

This transformation is unitary and canonical. The vacuum of the diagonalized Hamiltonian is characterized by $\beta_k |0\rangle = 0$. The angle θ_k is determined during the diagonalization of the Hamiltonian. It is inserted later in Section 7.3, when the structure factor is evaluated numerically for a specific scenario.

We restrict ourselves to the single mode approximation. Hence, the spin operator S^z does not change the number of magnons and therefore contributes only to the elastic part of the dynamical structure factor, in which we are not interested.

At first, we have to express the spin operators in terms of the creation/annihilation operators

$$S_i^x = \frac{1}{2}\left(S_i^+ + S_i^-\right) \tag{3.24a}$$
$$S_i^y = \frac{1}{2i}\left(S_i^+ - S_i^-\right). \tag{3.24b}$$

Following the conventions (A.2a), the Fourier transform into momentum space reads

$$
\begin{aligned}
S^x_k &= \sum_i \mathrm{e}^{-ikr_i}\, S^x_i \\
&= \frac{1}{2}\left\{ \sum_{i\in A} \left[2\,(S-n)\, b^\dagger_i + b_i\right] \mathrm{e}^{-ikr_i} + \sum_{i\in B} \left[b^\dagger_i + 2\,(S-n)\, b_i\right] \mathrm{e}^{-ikr_i} \right\} \\
&= \frac{1}{2}\frac{1}{\sqrt{N}} \sum_{k'} \left\{ \sum_{i\in A} \left[2\,(S-n)\, b^\dagger_{k'}\, \mathrm{e}^{-ir_i\left(k+k'\right)} + b_{k'}\, \mathrm{e}^{-ir_i\left(k-k'\right)}\right] \right. \\
&\quad \left. + \sum_{i\in B} \left[b^\dagger_{k'}\, \mathrm{e}^{-ir_i\left(k+k'\right)} + 2\,(S-n)\, b_{k'}\, \mathrm{e}^{-ir_i\left(k-k'\right)}\right] \right\} \\
&= \frac{1}{2\sqrt{N}} \frac{N}{2} \sum_{k'} \left\{ \left[\delta(k+k') + \delta(k+k'+Q)\right] 2\,(S-n)\, b^\dagger_{k'} \right. \\
&\quad + \left[\delta(k-k') + \delta(k-k'+Q)\right] b_{k'} + \left[\delta(k+k') - \delta(k+k'+Q)\right] b^\dagger_{k'} \\
&\quad \left. + \left[\delta(k-k') - \delta(k-k'+Q)\right] 2\,(S-n)\, b_{k'} \right\} \\
&= \frac{\sqrt{N}}{2} \left[\left(S-n+\frac{1}{2}\right)\left(b^\dagger_{-k} + b_k\right) + \left(S-n-\frac{1}{2}\right)\left(b^\dagger_{-k-Q} - b_{k+Q}\right) \right],
\end{aligned}
\tag{3.25}
$$

where the identities (A.8a) and (A.8b) for the collinear phase have been used for the two sums over the sublattices. The vector Q is the magnetic ordering vector, which reads $Q = (1,0,1)$ for the three dimensional collinear phase. For convenience, we denote all reciprocal lattice vectors in units of $\pi/(\text{lattice constant})$.

Next, the operators are transformed using the Bogoliubov transformation (3.23)

$$
\begin{aligned}
S^x_k = {} & \frac{\sqrt{N}}{2} \left(\cosh\theta_k + \sinh\theta_k\right) \\
& \cdot \left[\left(S-n+\frac{1}{2}\right)\left(\beta^\dagger_{-k} + \beta_k\right) + \left(S-n-\frac{1}{2}\right)\left(\beta^\dagger_{-k-Q} - \beta_{k+Q}\right) \right].
\end{aligned}
\tag{3.26}
$$

Finally, the spin operators are inserted into the dynamical structure factor

$$\begin{aligned}
S_T^{xx}(k,\omega) = &\frac{\pi}{1-e^{-\beta\omega}}\frac{N}{4}\left(\cosh\theta_k+\sinh\theta_k\right)^2 \\
&\cdot\Bigg\{\sum_m \langle 0|\left(S-n+\frac{1}{2}\right)\left(\beta^\dagger_{-k}+\beta_k\right)+\left(S-n-\frac{1}{2}\right)\left(\beta^\dagger_{-k-Q}-\beta_{k+Q}\right)|m\rangle \\
&\cdot\langle m|\left(S-n+\frac{1}{2}\right)\left(\beta^\dagger_k+\beta_{-k}\right)+\left(S-n-\frac{1}{2}\right)\left(\underbrace{\beta^\dagger_{k-Q}}_{\beta^\dagger_{k+Q}}-\beta_{-k+Q}\right)|0\rangle\,\delta(\omega-\omega_m) \\
&-\sum_n \langle n|\left(S-n+\frac{1}{2}\right)\left(\beta^\dagger_{-k}+\beta_k\right)+\left(S-n-\frac{1}{2}\right)\left(\beta^\dagger_{-k-Q}-\beta_{k+Q}\right)|0\rangle \\
&\cdot\langle 0|\left(S-n+\frac{1}{2}\right)\left(\beta^\dagger_k+\beta_{-k}\right)+\left(S-n-\frac{1}{2}\right)\left(\beta^\dagger_{k-Q}-\underbrace{\beta_{-k+Q}}_{\beta_{-k-Q}}\right)|n\rangle\,\delta(\omega+\omega_n)\Bigg\}
\end{aligned} \tag{3.27}$$

When we restrict ourselves to the creation and annihilation of single magnon states, only the highlighted operators contribute. The periodicity of the creation/annihilation operators can easily be seen in their Fourier transform (A.1)

$$\begin{aligned}
\beta_{-k+Q} &= \frac{1}{\sqrt{N}}\sum_i \mathrm{e}^{-ir_i(-k+Q)}\,\beta_i\cdot\underbrace{\mathrm{e}^{-iQr_i}\,\mathrm{e}^{iQr_i}}_{=1} \\
&= \frac{1}{\sqrt{N}}\sum_i \mathrm{e}^{-ir_i(-k-Q)}\cdot\underbrace{\mathrm{e}^{-2ir_iQ}}_{=1} \\
&= \beta_{-k-Q}
\end{aligned} \tag{3.28}$$

Now, we have obtained the final result for the inelastic part of the dynamical structure factor

$$\begin{aligned}
S_T^{xx}(k,\omega) &= \frac{\pi}{1-e^{-\beta\omega}}\frac{N}{4}\left(\cosh\theta_k+\sinh\theta_k\right)^2\left[\left(S-n+\frac{1}{2}\right)^2-\left(S-n-\frac{1}{2}\right)^2\right] \\
&\quad\cdot\left[\delta(\omega-\omega_k)-\delta(\omega+\omega_k)\right] \\
&= \frac{N\pi}{1-e^{-\beta\omega}}(S-n)\frac{1}{2}\left(\cosh\theta_k+\sinh\theta_k\right)^2\left[\delta(\omega-\omega_k)-\delta(\omega+\omega_k)\right].
\end{aligned} \tag{3.29}$$

Analogous to S_k^x, the Fourier transform of S_i^y reads

$$\begin{aligned}
S_k^y = &\frac{\sqrt{N}}{2i}\left(\cosh\theta_k+\sinh\theta_k\right) \\
&\cdot\left[\left(S-n-\frac{1}{2}\right)\left(\beta^\dagger_{-k}+\beta_k\right)+\left(S-n+\frac{1}{2}\right)\left(\beta^\dagger_{-k-Q}-\beta_{k+Q}\right)\right].
\end{aligned} \tag{3.30}$$

Therewith, $S_T^{yy}(k,\omega)$ is identical to $S_T^{xx}(k,\omega)$, which is consistent with the rotational symmetry about S^z.

Note that the inelastic part of the dynamical structure factor S^{xx} and S^{yy} is linear in the spin S, while the elastic part S^{zz} is quadratic in S [76]. A very similar result for (3.29) is mentioned in Ref. [54]. The wave vector dependence of (3.29) is manifested in the angle θ_k, which depends on the studied Hamiltonian.

4. 2D Néel phase with biquadratic exchange

In this section, the two dimensional Néel phase with an additional biquadratic exchange J_{bq} is studied. The Néel phase is the ground state of the antiferromagnetic Heisenberg model with nearest neighbor exchange (2.2). The schematic spin pattern can be found in Fig. 2.4a.

The relevance of a biquadratic exchange $\propto (\mathbf{S}_i \cdot \mathbf{S}_j)^2$ for $S \geq 1$ has already been discussed in Section 2.7. Biquadratic exchange terms are of special importance in the case of a many-electron exchange with a total spin of $S \geq 1$ [61].

For $S = 1/2$, the spin operators $S^\alpha = \sigma^\alpha/2$ are represented by the Pauli matrices σ^α. Because of the identity

$$\sigma^\alpha \sigma^\beta = \delta^{\alpha\beta} + i \sum_\gamma \epsilon^{\alpha\beta\gamma} \sigma^\gamma \tag{4.1}$$

of the Pauli matrices, a biquadratic term always reduces to bilinear one for $S = 1/2$.

We apply the Schwinger bosons as well as the Dyson-Maleev representation to the Heisenberg model with biquadratic exchange and introduce the correspondent mean field approximation for each of them. Our aim is to study the influence of the biquadratic exchange and to compare our results to results obtained by exact diagonalization and series expansion.

The studied Hamiltonian reads

$$\begin{aligned} H =& J \sum_{\langle i,j \rangle} \mathbf{S}_i \cdot \mathbf{S}_j - J_{\mathrm{bq}} \sum_{\langle i,j \rangle} \left(\mathbf{S}_i \cdot \mathbf{S}_j \right)^2 && \text{(4.2a)} \\ =& J \sum_{\langle i,j \rangle} \left(-S_i^z S_j^z + \frac{1}{2} \left(S_i^+ S_j^+ + \mathrm{h.\,c.} \right) \right) \\ & - J_{\mathrm{bq}} \sum_{\langle i,j \rangle} \left(-S_i^z S_j^z + \frac{1}{2} \left(S_i^+ S_j^+ + \mathrm{h.\,c.} \right) \right)^2, && \text{(4.2b)} \end{aligned}$$

with $J, J_{\mathrm{bq}} > 0$. The spins on one sublattice have already been rotated.

4.1. Dyson-Maleev representation

4.1.1. Mean field approximation

At first, we study the Hamiltonian (4.2b) in terms of the Dyson-Maleev representation (3.7) and (3.8). The bilinear product of the spin operators in (4.2b) reads

$$\mathbf{S}_i \cdot \mathbf{S}_j = -S^2 + S\left(\hat{n}_i + \hat{n}_j + b_i^\dagger b_j^\dagger + b_i\, b_j\right) - \hat{n}_i\hat{n}_j - \frac{1}{2}\left(b_i^\dagger \hat{n}_i b_j^\dagger + b_i\, \hat{n}_j b_j\right), \tag{4.3}$$

where $i \in A$ and $j \in B$. $\mathcal{O}(S^0)$ is quartic in the bosonic creation and annihilation operators. Thus, these terms have to be decoupled to bilinear expressions within a mean field approximation.

We introduce the expectation values

$$n := \left\langle b_i^\dagger b_i \right\rangle = \left\langle b_j^\dagger b_j \right\rangle \tag{4.4a}$$

$$a := \left\langle b_i^\dagger b_j^\dagger \right\rangle = \left\langle b_i\, b_j \right\rangle, \tag{4.4b}$$

where i, j are nearest neighbor sites with $i \in A$ and $j \in B$. All other expectation values precisely

$$0 = \left\langle b_i^\dagger b_j \right\rangle = \left\langle b_j^\dagger b_i \right\rangle$$
$$0 = \left\langle b_i^\dagger b_i^\dagger \right\rangle = \left\langle b_i\, b_i \right\rangle,$$

vanish because of the symmetry about S^z. It is assumed that all values are real. The quartic expressions are now decoupled according to Wick's theorem [75], which yields

$$\begin{aligned} \hat{n}_i\hat{n}_j &= b_i^\dagger b_i\, b_j^\dagger b_j \\ &\approx n\left(\hat{n}_i + \hat{n}_j\right) + a\left(b_i^\dagger b_j^\dagger + b_i\, b_j\right) - n^2 - a^2 \end{aligned} \tag{4.5a}$$

$$\begin{aligned} b_i^\dagger \hat{n}_i\, b_j^\dagger &= b_i^\dagger b_i^\dagger b_i\, b_j^\dagger \\ &\approx 2a b_i^\dagger b_i\, + 2n b_i^\dagger b_j^\dagger - 2na \end{aligned} \tag{4.5b}$$

$$\begin{aligned} b_i\, \hat{n}_j\, b_j &= b_i\, b_j^\dagger b_j\, b_j \\ &\approx 2a b_j^\dagger b_j\, + 2n b_i\, b_j\, - 2na. \end{aligned} \tag{4.5c}$$

The constant terms are unimportant and consequently neglected from now on. Therewith, the mean field approximation for the bilinear exchange results in

$$\mathbf{S}_i \cdot \mathbf{S}_j\Big|^{\mathrm{MF}} = \Big(\underbrace{S}_{O(S)}\ \underbrace{-n-a}_{O\left(S^0\right)}\Big)\left(\hat{n}_i\, + \hat{n}_j\, + b_i^\dagger b_j^\dagger + b_i\, b_j\right) + \text{const.}. \tag{4.6}$$

All operators have the same prefactor $S - n - a$, so that the spin rotation is conserved, as we will see later.

Now, we concentrate on the biquadratic term. Naturally, the decoupling is more complicated and challenging. The biquadratic term in the Dyson-Maleev representation sorted in orders of S has the form

$$\begin{aligned}\left(\mathbf{S}_i \cdot \mathbf{S}_j\right)^2 = S^4 & \\ & - 2S^3 \left(\hat{n}_i + \hat{n}_j + \hat{I}_0\right) \\ & + S^2 \left[\hat{n}_i^2 + \hat{n}_j^2 + 4\hat{n}_i\hat{n}_j + \hat{I}_0^2 + \left(\hat{n}_i + \hat{n}_j\right)\hat{I}_0 + \hat{I}_0\left(\hat{n}_i + \hat{n}_j\right) + \hat{I}_0'\right] \\ & - S\left[2\left(\hat{n}_i\hat{n}_j^2 + \hat{n}_i^2\hat{n}_j\right) + \hat{n}_i\hat{n}_j\hat{I}_0 + \hat{I}_0\hat{n}_i\hat{n}_j\right. \\ & \left. + \frac{1}{2}\left(\hat{I}_0\hat{I}_0' + \hat{I}_0'\hat{I}_0 + \left(\hat{n}_i + \hat{n}_j\right)\hat{I}_0' + \hat{I}_0'\left(\hat{n}_i + \hat{n}_j\right)\right)\right] \\ & + \hat{n}_i^2\hat{n}_j^2 + \frac{1}{4}\hat{I}_0'^2 + \frac{1}{2}\left(\hat{n}_i\hat{n}_j\hat{I}_0' + \hat{I}_0'\hat{n}_i\hat{n}_j\right),\end{aligned} \tag{4.7}$$

where

$$\hat{I}_0 := b_i^\dagger b_j^\dagger + b_i\, b_j \tag{4.8a}$$

$$\hat{I}_0' := b_i^\dagger \hat{n}_i\, b_j^\dagger + b_i\, \hat{n}_j\, b_j \tag{4.8b}$$

with i, j on nearest neighbor sites.

Analogously to the bilinear term, the biquadratic term has to be treated in the same mean field approximation. For clarity, we do not list the prefactors of all terms here. They can be found in the Appendix B.1. Therewith, we obtain the mean field approximation

$$\begin{aligned}\left(\mathbf{S}_i \cdot \mathbf{S}_j\right)^2\Big|^{\mathrm{MF}} = -\Big[2S^3 - 2S^2\left(1 + 5\left(n+a\right)\right) + S\left(18\left(n+a\right)^2 + 8\left(n+a\right) + 1\right) \\ -12\left(n+a\right)^3 - 9\left(n+a\right)^2 - 2\left(n+a\right)\Big]\left(\hat{n}_i + \hat{n}_j + b_i^\dagger b_j^\dagger + b_i\, b_j\right) + \text{const.}\end{aligned} \tag{4.9}$$

for the biquadratic exchange.

Neglecting all constant terms, the mean field Hamiltonian corresponding to (4.2b) is

$$\begin{aligned}H^{\mathrm{MF}} &= \Big\{J\left(S-\alpha\right) + J_{\mathrm{bq}}\Big[2S^3 - 2S^2\left(1 + 5\alpha\right) + S\left(18\alpha^2 + 8\alpha + 1\right) \\ &\qquad -12\alpha^3 - 9\alpha^2 - 2\alpha\Big]\Big\} \sum_{\langle i,j\rangle}\left(\hat{n}_i + \hat{n}_j + b_i^\dagger b_j^\dagger + b_i\, b_j\right) \\ &= \tilde{J}(\alpha)\left(S-\alpha\right)\sum_{\langle i,j\rangle}\left(\hat{n}_i + \hat{n}_j + b_i^\dagger b_j^\dagger + b_i\, b_j\right),\end{aligned} \tag{4.10}$$

where

$$\tilde{J}(\alpha) := J + J_{\mathrm{bq}} \frac{2S^3 - 2S^2(1+5\alpha) + S(18\alpha^2 + 8\alpha + 1) - 12\alpha^3 - 9\alpha^2 - 2\alpha}{S - \alpha}, \tag{4.11}$$

and the new parameter $\alpha := n + a$ have been introduced for convenience. The neglected constant terms are the classical ground state energy $E_0 := NdJS^2 + NdJ_{\mathrm{bq}}S^4$ for a d-dimensional lattice ($d = 2$ in our case).

Our next aim is to diagonalize the Hamiltonian. Therefore, we rewrite the sum over all nearest neighbors

$$H^{\mathrm{MF}} = \frac{1}{2}\tilde{J}(\alpha)\,(S-\alpha) \sum_{i,\delta} \left(\hat{n}_i + \hat{n}_{i+\delta} + b_i^\dagger b_{i+\delta}^\dagger + b_i\, b_{i+\delta} \right), \tag{4.12}$$

where $\delta \in \{(\pm 1, 0), (0, \pm 1)\}$ is the vector between two nearest neighbor sites on the square lattice. The factor $1/2$ prevents that bonds are over counted. Furthermore, we insert the Fourier transform (A.1) of the creation/annihilation operators

$$\begin{aligned}
H^{\mathrm{MF}} &= \frac{1}{2}\tilde{J}(\alpha)\,(S-\alpha)\,\frac{1}{N} \sum_{i,\delta,k,k'} \Big[\mathrm{e}^{-ir_i\left(k-k'\right)}\, b_k^\dagger b_{k'} + \mathrm{e}^{-ir_i\left(k-k'\right)}\, \mathrm{e}^{-i\delta\left(k-k'\right)}\, b_k^\dagger b_{k'} \\
&\quad + \mathrm{e}^{-ir_i\left(k+k'\right)}\, \mathrm{e}^{-i\delta k'}\, b_k^\dagger b_{k'}^\dagger + \mathrm{e}^{-ir_i\left(-k-k'\right)}\, \mathrm{e}^{i\delta k'}\, b_k b_{k'} \Big] \\
&= \frac{1}{2}\tilde{J}(\alpha)\,(S-\alpha) \sum_{\delta,k} \left[2 b_k^\dagger b_k + \mathrm{e}^{-i\delta k}\, b_k^\dagger b_{-k}^\dagger + \mathrm{e}^{i\delta k}\, b_k b_{-k} \right] \\
&= \tilde{J}(\alpha)\,(S-\alpha) \sum_{k} \left[4 b_k^\dagger b_k + \left(\cos k_a + \cos k_b\right) \left(b_k^\dagger b_{-k}^\dagger + b_k b_{-k} \right) \right] \\
&= 4\tilde{J}(\alpha)\,(S-\alpha) \sum_{k>0} \left[b_k^\dagger b_k + b_{-k}^\dagger b_{-k} + \gamma_k \left(b_k^\dagger b_{-k}^\dagger + b_k b_{-k} \right) \right],
\end{aligned} \tag{4.13}$$

where the sum over all lattice sites yields Dirac delta functions (A.4) and the sum over the four nearest neighbors yields

$$4\gamma_k := \sum_\delta \mathrm{e}^{\pm i\delta k} = 2\left(\cos k_a + \cos k_b\right). \tag{4.14}$$

In the final step, we have to transform the Hamiltonian by a Bogoliubov transformation (3.23) whereby

$$\begin{aligned}
H^{\mathrm{MF}} = 4\tilde{J}(\alpha)\,(S-\alpha) \sum_{k>0} \Big\{ & \left[\cosh 2\theta_k + \gamma_k \sinh 2\theta_k\right] \left(\beta_k^\dagger \beta_k + \beta_{-k}^\dagger \beta_{-k} \right) \\
& \left[\sinh 2\theta_k + \gamma_k \cosh 2\theta_k\right] \left(\beta_k^\dagger \beta_{-k}^\dagger + \beta_k^\dagger \beta_{-k}^\dagger \right) \\
& + 2\sinh^2\theta_k + \gamma_k \sinh 2\theta_k \Big\}
\end{aligned} \tag{4.15}$$

is the Hamiltonian expressed in the new bosonic creation and annihilation operators $\beta_k^\dagger$ and β_k.

In order to diagonalize the Hamiltonian, the prefactor in front of the non-diagonal operators has to vanish, which fixes the angle θ_k to

$$\begin{aligned} & \sinh 2\theta_k + \gamma_k \cosh 2\theta_k \stackrel{!}{=} 0 \\ \Leftrightarrow \quad & \tanh 2\theta_k = -\gamma_k. \end{aligned} \tag{4.16}$$

The prefactor in front of the diagonal operators is the spin wave dispersion. With trigonometric identities, one obtains

$$\begin{aligned} \omega_k &= 4\tilde{J}(\alpha)\,(S-\alpha)\,\sqrt{1-\gamma_k^2} \\ &= 4\tilde{J}(\alpha)\,(S-\alpha)\,\sqrt{1-\frac{1}{4}\left(\cos k_a + \cos k_b\right)^2}, \end{aligned} \tag{4.17}$$

by using the result

$$\begin{aligned} \sinh^2 2\theta_k &= \frac{\gamma_k^2}{1-\gamma_k^2} \\ \Leftrightarrow \sinh 2\theta_k &= \pm\frac{\gamma_k}{\sqrt{1-\gamma_k^2}}. \end{aligned} \tag{4.18}$$

According to (4.16), we have to select the negative solution, because $\cosh x \geq 1 \;\forall\; x$. The constant term in (4.15) is the ground state energy of H^{MF}

$$\begin{aligned} E^{\mathrm{MF}} &= \sum_k \left(\frac{\omega_k}{2} - 2\tilde{J}(\alpha)\,(S-\alpha) \right) \\ &= 2\tilde{J}(\alpha)\,(S-\alpha) \sum_k \left(\sqrt{1-\gamma_k^2} - 1 \right). \end{aligned} \tag{4.19}$$

Finally, the diagonalized Hamiltonian reads

$$H^{\mathrm{MF}} = \sum_k \omega_k \beta_k^\dagger \beta_k + E^{\mathrm{MF}}. \tag{4.20}$$

The gapless excitations at $k = (1,1)$ (the magnetic ordering vector of the Néel phase) and $k = (0,0)$ are the expected Goldstone modes (see Section 2.4.3), because the ground state of the system has broken symmetry. The existence of these gapless excitations is secured by the systematical expansion in $1/S$ and not self-evident because of the mean field approximation.

4.1.2. Self-consistency

We now have to determine the value of $\alpha = n - a$ self-consistently. Therefore, we calculate the energy correction of the ground state energy of H^{MF} for a single lattice site in first order perturbation theory, where α is treated as a small perturbation.

In general, we split our Hamiltonian H^{MF} in two parts $H = H_0 + \chi H_\chi$ where χ is regarded as a small perturbation. Thus, the leading correction of the ground state energy $E^{\mathrm{MF}}/N = 1/N \langle 0| H^{\mathrm{MF}} |0\rangle$ per spin is given as

$$\frac{1}{N}\frac{\partial E^{\mathrm{MF}}}{\partial \chi} = \frac{1}{N}\frac{\partial}{\partial \chi} \langle 0| H^{\mathrm{MF}} |0\rangle \tag{4.21a}$$

$$= \langle 0| H_\chi |0\rangle . \tag{4.21b}$$

In terms of the quantum correction parameter α, one obtains

$$\begin{aligned}\frac{1}{N}\frac{\partial E^{\mathrm{MF}}}{\partial \alpha} &= \frac{1}{N} \langle 0| \frac{\partial}{\partial \alpha} H^{\mathrm{MF}} |0\rangle \\ &= \frac{1}{2}\sum_\delta \underbrace{\langle 0| \hat{n}_i + \hat{n}_j + b_i^\dagger b_j^\dagger + b_i\, b_j\, |0\rangle}_{=2n+2a=2\alpha} \cdot \frac{\partial(\tilde{J}(\alpha)\,(S-\alpha))}{\partial \alpha} \\ &= \sum_\delta \alpha \cdot \frac{\partial(\tilde{J}(\alpha)\,(S-\alpha))}{\partial \alpha}\end{aligned} \tag{4.22a}$$

where the partial derivative only acts on $\tilde{J}(\alpha)(S-\alpha)$. Hence, α is determined by the self-consistency equation

$$\frac{1}{N}\frac{\partial E^{\mathrm{MF}}}{\partial \alpha} = 4\alpha \frac{\partial}{\partial \alpha}\left(\tilde{J}(\alpha)\,(S-\alpha)\right). \tag{4.23}$$

Utilizing the mean field energy per site in thermodynamic limit

$$\begin{aligned}\frac{1}{N}E^{\mathrm{MF}} &= \frac{1}{(2\pi)^2} 2\tilde{J}(\alpha)\,(S-\alpha) \iint\limits_{\mathrm{BZ}} \mathrm{d}^2k\, \left(\sqrt{1-\gamma_k^2} - 1\right) \\ &= \frac{1}{(2\pi)^2} 2\tilde{J}(\alpha)\,(S-\alpha) \iint\limits_{\mathrm{BZ}} \mathrm{d}^2k \sqrt{1 - \frac{1}{4}\left(\cos k_a + \cos k_b\right)^2} - 2\tilde{J}(\alpha)\,(S-\alpha),\end{aligned} \tag{4.24}$$

we derive the equation

$$\alpha = \frac{1}{2}\frac{1}{(2\pi)^2} \iint\limits_{\mathrm{BZ}} \mathrm{d}^2k \sqrt{1 - \frac{1}{4}\left(\cos k_a + \cos k_b\right)^2} - \frac{1}{2} \tag{4.25}$$

for α, where the integration runs over the *Brillouin zone* (BZ). We note that the value of α is independent of J and J_{bq}.

4.1.3. Numerics

To evaluate (4.25) numerically, one integration is done analytically by introducing a density of states $\varrho(\gamma)$ (C.6). For a detailed derivation, see Appendix C. Thereby, (4.25) is rewritten as

$$\begin{aligned}\alpha &= \int_0^1 \mathrm{d}\gamma\, \varrho\,(\gamma)\, \sqrt{1-\gamma^2} - \frac{1}{2} \\ &= \frac{2}{\pi^2} \int_0^1 \mathrm{d}\gamma\, K\left(\sqrt{1-\gamma^2}\right) \sqrt{1-\gamma^2} - \frac{1}{2},\end{aligned} \tag{4.26}$$

where $K(x)$ denotes the *complete elliptic integral of the first kind* (C.5). The integration is done with MAPLE and the determined value of α for $S = 1$ is

$$\alpha = -0.0789737105. \tag{4.27}$$

We are interested in the influence of the biquadratic exchange on the excitation energies. Thus, the ratios of the dispersions with and without biquadratic exchange is an appropriate quantity, which is given by

$$\begin{aligned}\frac{\tilde{J}(\alpha)}{J} &= 1 + \nu \frac{2S^3 - 2S^2(1+5\alpha) + S(18\alpha^2 + 8\alpha + 1) - 12\alpha^3 - 9\alpha^2 - 2\alpha}{S - \alpha} \\ &= 1 + 1.277081189 \cdot \nu,\end{aligned} \tag{4.28}$$

for $S = 1$ with $\nu := J_{\mathrm{bq}}/J$. It increases linearly with a gradient of 1.277081189, which is compared to gradients obtained by other theoretical techniques at the end of this section.

4.2. Schwinger bosons

4.2.1. Mean field approximation

We now study the same Hamiltonian (4.2b) as before, but in the Schwinger bosons representation.

At first, we concentrate on the usual bilinear term. Replacing the spin operators in the bilinear term with the Schwinger bosons representation (3.9), leads to the expression

$$\mathbf{S}_i \cdot \mathbf{S}_j = -\frac{1}{4}\left(a_i^\dagger a_j^\dagger a_i\, a_j + b_i^\dagger b_j^\dagger b_i\, b_j - a_i^\dagger b_j^\dagger a_i\, b_j - b_i^\dagger a_j^\dagger b_i\, a_j + 2a_i^\dagger a_j^\dagger b_i\, b_j + 2b_i^\dagger b_j^\dagger a_i\, a_j\right). \tag{4.29}$$

As the constraint (3.10) applies to each lattice site individually, we use

$$(2S)^2 = \left(a_i^\dagger a_i + b_i^\dagger b_i\right)\left(a_j^\dagger a_j + b_j^\dagger b_j\right), \tag{4.30}$$

to rewrite the bilinear term as

$$\begin{aligned}\mathbf{S}_i \cdot \mathbf{S}_j - S^2 &= -\frac{1}{2}\left(a_i^\dagger a_j^\dagger + b_i^\dagger b_j^\dagger\right)\left(a_i\, a_j + b_i\, b_j\right) \\ &= -\frac{1}{2} A_{ij}^\dagger A_{ij},\end{aligned} \tag{4.31}$$

where the bond operators

$$A_{ij}^\dagger = a_i^\dagger a_j^\dagger + b_i^\dagger b_j^\dagger \tag{4.32a}$$

$$A_{ij} = a_i\, a_j + b_i\, b_j \tag{4.32b}$$

have been introduced. They connect neighboring sites on different sublattices. Inserting the operators A_{ij} and $A_{ij}^\dagger$ in the bilinear and in the biquadratic term, one obtains

$$H = -\frac{J}{2}\sum_{\langle i,j\rangle}\left(A_{ij}^\dagger A_{ij} - 2S^2\right) - \frac{J_{\mathrm{bq}}}{4}\sum_{\langle i,j\rangle}\left(A_{ij}^\dagger A_{ij} - 2S^2\right)^2 \tag{4.33a}$$

$$= -\frac{J}{2}\sum_{\langle i,j\rangle}\left(A_{ij}^\dagger A_{ij} - 2S^2\right) - \frac{J_{\mathrm{bq}}}{4}\sum_{\langle i,j\rangle}\left(4S^4 - 4S^2 A_{ij}^\dagger A_{ij} + \left(A_{ij}^\dagger A_{ij}\right)^2\right) \tag{4.33b}$$

$$= -\frac{J}{2}\sum_{\langle i,j\rangle} A_{ij}^\dagger A_{ij} - \frac{J_{\mathrm{bq}}}{4}\sum_{\langle i,j\rangle}\left(-4S^2 A_{ij}^\dagger A_{ij} + \left(A_{ij}^\dagger A_{ij}\right)^2\right) + \text{const.} \tag{4.33c}$$

Next, we introduce an appropriate mean field approximation in terms of the bond operators. To illustrate and justify this approximation, we extend to $\mathcal{N}$ Schwinger boson flavors in the next steps, because the Schwinger bosons mean field theory is based on an expansion in $1/\mathcal{N}$ [44, 77, 78].

For $\mathcal{N}$ flavors, the bilinear term reads

$$\mathbf{S}_i \cdot \mathbf{S}_j = -\frac{1}{\mathcal{N}} A_{ij}^\dagger A_{ij} + S^2 \tag{4.34}$$

with the generalized bond operators

$$A_{ij}^\dagger = \sum_{m=1}^{\mathcal{N}} a_{i,m}^\dagger a_{j,m}^\dagger \tag{4.35a}$$

$$A_{ij} = \sum_{m=1}^{\mathcal{N}} a_{i,m} a_{j,m} \tag{4.35b}$$

and the constraint

$$\sum_{m=1}^{\mathcal{N}} a_{i,m}^\dagger a_{i,m} = \mathcal{N} S. \tag{4.36}$$

We define the expectation value

$$A := \langle A_{ij}\rangle = \langle A_{ij}^\dagger\rangle \in \mathbb{R}_0^+, \tag{4.37}$$

which is proportional to $\mathcal{N}$ according to the generalized constraint (4.36). Hence, the bilinear term is decoupled by

$$\begin{aligned}\mathbf{S}_i \cdot \mathbf{S}_j\Big|_{\mathrm{MF}} &\approx \frac{1}{\mathcal{N}} \left(A_{ij}^\dagger \left\langle A_{ij} \right\rangle + \left\langle A_{ij}^\dagger \right\rangle A_{ij} \right) - A^2 \\ &\approx \underbrace{\underbrace{\frac{1}{\mathcal{N}}}_{\mathcal{O}(1/\mathcal{N})} \underbrace{\left(A A_{ij}^\dagger + \mathrm{h.\,c.} \right)}_{\mathcal{O}(\mathcal{N})}}_{\mathcal{O}(1)},\end{aligned} \tag{4.38}$$

where we only keep the non-constant terms of the leading order $\mathcal{O}(1)$ in the expansion in $1/\mathcal{N}$.

In the same way, the quartic term of bond operators is decoupled in leading order by

$$\frac{1}{\mathcal{N}^2} \left(A_{ij}^\dagger A_{ij} \right) \cdot \left(A_{ij}^\dagger A_{ij} \right) \approx \frac{2A^2}{\mathcal{N}} \left(A_{ij}^\dagger A + A A_{ij} \right) + \text{const.}\,. \tag{4.39}$$

The factor 2 is a consequence of Wicks's theorem [75], as there are two possibilities to contract the operator $A_{ij}^\dagger$ or A_{ij}, respectively. Thus, the mean field decoupling of the entire biquadratic term is

$$\left(\mathbf{S}_i \cdot \mathbf{S}_j \right)^2 \Big|_{\mathrm{MF}} \approx -\frac{2S^2}{\mathcal{N}} A \left(1 - \frac{A^2}{\mathcal{N} S^2} \right) \left(A_{ij}^\dagger + A_{ij} \right) + \text{const.}\,. \tag{4.40}$$

We omit all constant terms from now on. Since $A \propto \mathcal{N} S$, Eq. (4.40) overall obtains a minus sign. Together with the bilinear exchange (4.38), the antiferromagnetic exchange in the Hamiltonian (4.33) is strengthened.

Returning to $\mathcal{N} = 2$, the mean field Hamiltonian is given by

$$H^{\mathrm{MF}} = -\frac{A}{2} \left(J - 2J_{\mathrm{bq}} S^2 \left(1 - \frac{A^2}{2S^2} \right) \right) \sum_{\langle i,j \rangle} \left(A_{ij}^\dagger + \mathrm{h.\,c.} \right) + \lambda \sum_i \left(a_i^\dagger a_i + b_i^\dagger b_i \right). \tag{4.41a}$$

The Lagrange multiplier λ has been introduced to respect the constraint (3.10). As before, we rewrite the sum over all nearest neighbors as a sum over all lattice sites and vectors δ to the nearest neighbor sites. The additional prefactor of $1/2$ prevents that bonds are over counted. The Hamiltonian reads

$$H^{\mathrm{MF}} = -\frac{\tilde{J}(A) A}{4} \sum_{i,\delta} \left(a_i^\dagger a_{i+\delta}^\dagger + b_i^\dagger b_{i+\delta}^\dagger + \mathrm{h.\,c.} \right) + \lambda \sum_i \left(a_i^\dagger a_i + b_i^\dagger b_i \right) \tag{4.41b}$$

with the short cut

$$\tilde{J}(A) := J - 2J_{\mathrm{bq}} S^2 \left(1 - \frac{A^2}{2S^2} \right). \tag{4.42}$$

The following steps are analogous to the calculation made in the Dyson-Maleev representation. Therefore, only the intermediate results are shown here. Following the conventions according to (A.1), the Hamiltonian (4.41b) in momentum space reads

$$\begin{aligned} H^{\mathrm{MF}} &= -\frac{\tilde{J}(A)A}{4}\sum_k \left(a_k^\dagger a_{-k}^\dagger + b_k^\dagger b_{-k}^\dagger + \mathrm{h.\,c.}\right)\underbrace{\sum_\delta \mathrm{e}^{-ik\delta}}_{:=4\gamma_k} + \lambda\sum_k\left(a_k^\dagger a_k + b_k^\dagger b_k\right) \\ &= -2\tilde{J}(A)A\sum_{k>0}\left(a_k^\dagger a_{-k}^\dagger + b_k^\dagger b_{-k}^\dagger + \mathrm{h.\,c.}\right)\gamma_k + \lambda\sum_{k>0}\left(a_k^\dagger a_k + b_k^\dagger b_k + \left(k\to -k\right)\right). \end{aligned} \tag{4.43}$$

Again, we use a Bogoliubov transformation (3.23) to diagonalize the Hamiltonian. Therewith, it transforms to

$$H^{\mathrm{MF}} = \sum_{k>0}\left[A_k\left(\alpha_k^\dagger\alpha_k + \alpha_{-k}^\dagger\alpha_{-k} + \left(\alpha\to\beta\right)\right) + B_k\left(\alpha_k^\dagger\alpha_{-k}^\dagger + \beta_k^\dagger\beta_{-k}^\dagger + \mathrm{h.\,c.}\right)\right] + E^{\mathrm{MF}}, \tag{4.44}$$

in terms of the new bosonic operators α and β, with

$$A_k = -2\tilde{J}(A)A\gamma_k\sinh 2\theta_k + \lambda\cosh 2\theta_k \tag{4.45a}$$

$$B_k = -2\tilde{J}(A)A\gamma_k\cosh 2\theta_k + \lambda\sinh 2\theta_k \tag{4.45b}$$

$$E^{\mathrm{MF}} = \sum_k\left(-2\tilde{J}(A)A\gamma_k\sinh 2\theta_k + 2\lambda\sinh^2\theta_k\right). \tag{4.45c}$$

The Hamiltonian is diagonal for $B_k \stackrel{!}{=} 0$. Thus, the relation[1] for the angle θ_k is given by

$$\tanh 2\theta_k = \frac{2\tilde{J}(A)A}{\lambda}\gamma_k\,. \tag{4.46}$$

This leads to the dispersion

$$A_k =: \omega_k := \sqrt{\lambda^2 - \left(2\tilde{J}(A)A\gamma_k\right)^2} \tag{4.47a}$$

and the mean field energy

$$E^{\mathrm{MF}} = \sum_k\left(\sqrt{\lambda^2 - \left(2\tilde{J}(A)A\gamma_k\right)^2} - \lambda\right). \tag{4.47b}$$

In thermodynamic limit, the mean field energy per spin reads

$$\frac{1}{N}E^{\mathrm{MF}} = \frac{1}{(2\pi)^2}\iint_{\mathrm{BZ}}\mathrm{d}^2k\,\sqrt{\lambda^2 - \left(2\tilde{J}(A)A\right)^2\gamma_k^2} - \lambda. \tag{4.47c}$$

[1] The relation obtains no minus sign compared to the one in the Dyson-Maleev representation (4.16). The missing minus sign is not important and is caused by the replacement of the bilinear term with Eq. (4.31).

4.2.2. Self-consistency

The procedure for deriving the self-consistency equations was explained in detail for the Dyson-Maleev representation (see Section 4.1). Treating λ and A as a small perturbation, one derives two self-consistency equations with Eq. (4.21). One for the Lagrange multiplier (the constraint)

$$2S = \frac{1}{N}\frac{\partial E^{\mathrm{MF}}}{\partial \lambda} \tag{4.48a}$$

and one for the quantum correction parameter

$$-2A\frac{\partial}{\partial A}\left(\tilde{J}(A)A\right) = \frac{1}{N}\frac{\partial E^{\mathrm{MF}}}{\partial A}\,. \tag{4.48b}$$

The self-consistency equation for λ results in

$$2S+1 = \frac{1}{(2\pi)^2}\iint\limits_{\mathrm{BZ}} \mathrm{d}^2k\, \frac{\lambda}{\sqrt{\lambda^2 - \left(2\tilde{J}(A)A\right)^2\gamma_k^2}} \tag{4.49a}$$

and the one for A in

$$A = \frac{1}{(2\pi)^2}\iint\limits_{\mathrm{BZ}} \mathrm{d}^2k\, \frac{2\tilde{J}(A)A\gamma_k^2}{\sqrt{\lambda^2 - \left(2\tilde{J}(A)A\right)^2\gamma_k^2}}. \tag{4.49b}$$

Note that the integrand in (4.49b) diverges for certain values of k, which was not the case for the Dyson-Maleev representation. There, numerator and denominator of the integrand vanish for the same k-values, so that there is no divergence.

The divergences in (4.49b) can be eliminated by considering the difference $\lambda \cdot$ (4.49a) $- 2\tilde{J}(A)A \cdot$ (4.49b) implying

$$\lambda\,(2S+1) - 2\tilde{J}(A)A^2 = \frac{1}{(2\pi)^2}\iint\limits_{\mathrm{BZ}} \mathrm{d}^2k\, \sqrt{\lambda^2 - \left(2\tilde{J}(A)A\right)^2\gamma_k^2}\,. \tag{4.50}$$

4.2.3. Evaluation in the symmetry broken phase

As mentioned before, the Schwinger bosons (3.9) can be used to describe the phase with spontaneously broken symmetry as well as the symmetric phase. We know that the ground state of the studied system has a spontaneously broken symmetry. Hence, there exist Goldstone modes. For these gapless excitations, the Lagrange multiplier λ has to be fixed to the value

$$\lambda = 2\tilde{J}(A)A. \tag{4.51}$$

The resulting Hamiltonian in the symmetry broken phase reads

$$H^{\mathrm{MF}} = \sum_k \omega_k \left(\alpha_k^\dagger \alpha_k + \beta_k^\dagger \beta_k \right) + E^{\mathrm{MF}} \tag{4.52}$$

with

$$\omega_k = 2\tilde{J}(A) A \sqrt{1 - \frac{1}{4} \left(\cos k_a + \cos k_b \right)^2} \tag{4.53a}$$

$$E^{\mathrm{MF}} = 2\tilde{J}(A) A \sum_k \left(\sqrt{1 - \frac{1}{4} \left(\cos k_a + \cos k_b \right)^2} - 1 \right). \tag{4.53b}$$

The self-consistent equation for A (4.50) is given by

$$A = 2S + 1 - \frac{1}{(2\pi)^2} \iint\limits_{\mathrm{BZ}} \mathrm{d}^2 k \, \sqrt{1 - \frac{1}{4} \left(\cos k_a + \cos k_b \right)^2} \tag{4.54a}$$

or as

$$A = 2S + 1 - 2 \int_0^1 \mathrm{d}\gamma \, \varrho\left(\gamma\right) \sqrt{1 - \gamma^2} \tag{4.54b}$$

in terms of a density of states (C.6). As before, the value of A is independent of $\tilde{J}(A)$. The evaluation of (4.54b) with MAPLE yields the result

$$A = 2.1579474210 \tag{4.55}$$

for $S = 1$. Therewith, we obtain

$$\begin{aligned} \frac{\tilde{J}(A)}{J} &= 1 - 2S^2 \left(1 - \frac{A^2}{2S^2} \right) \nu \\ &= 1 + 2.65673707 \cdot \nu, \end{aligned} \tag{4.56}$$

which is more than twice as much as in the Dyson-Maleev representation. In the upcoming section, both results are compared to results obtained by other methods. This helps us to decide, which spin representation and mean field approximation fits our purposes best.

4.3. Results & discussion

The huge difference in the gradient for the Schwinger bosons (4.56) and the Dyson-Maleev representation (4.28) is very surprising. Fortunately, our results for the 2D Néel phase with biquadratic exchange can be compared to gradients which are obtained by two other methods.

method	gradient
Schwinger bosons	2.65674
Dyson-Maleev	1.27708
exact diagonalization (4x4)	1.24505
series expansion	1.13423

Tab. 4.1.: Gradients for the influence of the biquadratic exchange on the excitation energies.

On the one hand, we have results calculated by an exact diagonalization of the Hamiltonian (4.2b). The Hamiltonian is exactly diagonalized on a finite 4x4 lattice to obtain the excitation energies as a function of the momentum k [79]. The calculations are repeated for several coupling ratios $\nu = J_{\mathrm{bq}}/J$. The data points in Fig. 4.1 are the maximum excitation energies found at $k = (0.5, 0.5)$ normalized to the excitation energy without biquadratic exchange.

On the other hand, the excitation energies can be calculated with a series expansion [55, 80]. Again, we calculated the ratios of the maximum excitation energies at $k = (0.5, 0.5)$.

For both methods, the gradient is determined by a linear fit. All results are compared in Tab. 4.1 and displayed in Fig. 4.1.

The Schwinger bosons result immediately catches ones eye, because the gradient outnumbers all other results by a factor greater than two. On the contrary, the Dyson-Maleev result matches very well with the exact diagonalization. The gradient of the series expansion, which is essentially exact, is slightly smaller. The exact diagonalization is hampered by finite-size effects, which cause the deviation to the result of the series expansion.

The deviation of the Dyson-Maleev gradient from the series expansion is in the range of 10-15%, which is still a bit too high but acceptable. Extending to a third dimension, the result should improve, since a mean field approximation becomes more accurate or even exact in higher dimensions. Therefore, we stick to the Dyson-Maleev representation and the corresponding mean field approximation for our upcoming analysis.

Discrepancies in the Schwinger boson mean field theory without biquadratic exchange have already appeared when the theory was introduced by Auerbach and Arovas. In their calculations, the coefficients of the mean field free energy exceed previous results by a factor of 2 and the spin correlation function by a factor of exactly $3/2$ [78]. In the mean field approximation for the Schwinger bosons, we treat both Schwinger bosons sitting on one lattice site independently. Thus, the constraint (3.10) is violated because because a change in the occupation of the a boson is always connected to a change of the occupation of the b boson sitting on the same lattice site (or vice versa). Hence, we suggest that the additional factors appear because of the missed fluctuations due to the interaction of the Schwinger bosons. As a consequence, Takahashi formulated a modified spin wave theory for the square lattice antiferromagnet [81]. Implying the Dyson-Maleev representation, the exact prefactor of the spin correlation function is preserved.

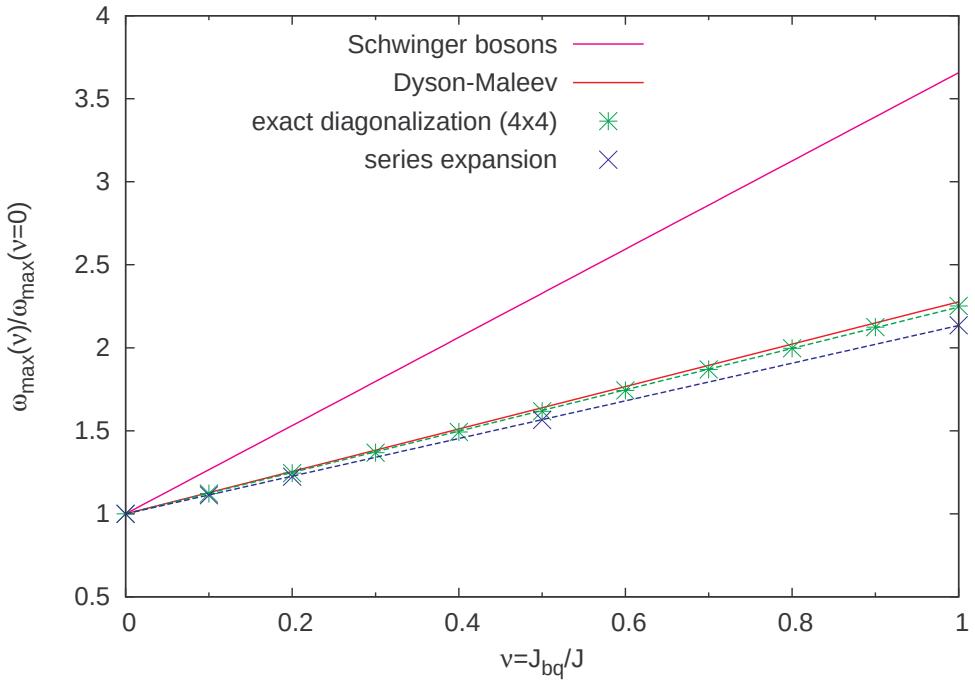

Fig. 4.1.: Influence of the biquadratic exchange on the excitation energies in the 2D Néel phase ($S = 1$). The dashed lines are fits to the corresponding data points.

5. 3D collinear phase

In this chapter, the frustrated Heisenberg model in the two dimensional collinear phase at $T = 0$ is extended to three dimensions.

The J_1-J_2 model (2.13) and the collinear phase have been of general interest. A brief overview is given in Section 2.6. For the iron pnictides, the upcoming chapter extends the work on the two dimensional collinear phase by Uhrig *et al*. [11] to three dimensions. The three dimensional character of the iron pnictides was revealed in recent neutron scattering studies because non-vanishing spin wave velocities and dispersions have been measured in all directions a, b and c [9, 10, 15]. The interlayer exchange J_c between the collinear ordered planes is antiferromagnetic and smaller in size than the in-plane exchange constants J_1 and J_2 due to the lattice structure (see Fig. 5.1). Hence, the interlayer exchange is also restricted to nearest neighbor sites. Furthermore, the spin wave velocity v_c is much smaller than v_a and v_b. Suitable ratios of v_c/v_a extracted from neutron scattering studies are $\sim$ 20-25 % [10, 9].

Thus, we study the Hamiltonian

$$H = J_1 \sum_{\langle i,j \rangle} \mathbf{S}_i \cdot \mathbf{S}_j + J_2 \sum_{\langle\langle i,j \rangle\rangle} \mathbf{S}_i \cdot \mathbf{S}_j + J_c \sum_{[i,j]} \mathbf{S}_i \cdot \mathbf{S}_j \tag{5.1}$$

with $J_1, J_2, J_c > 0$. The brackets $[i, j]$ indicate the exchange between inter-plane nearest neighbors. The small orthorhombic distortion within the collinear ordered layers is neglected.

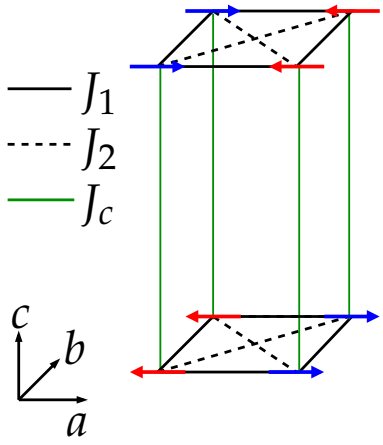

Fig. 5.1.: Three dimensional collinear phase with antiferromagnetic interlayer exchange J_c.

As a consequence of the results of the previous chapter, we choose the Dyson-Maleev representation. The mean field theory for the antiferromagnetic bilinear exchange has already been introduced. Hence, we now concentrate on the mean field approximation for the ferromagnetic bilinear exchange parallel to the spin stripes in b-direction. Combining the corresponding approximation for all exchange terms, we derive the mean field Hamiltonian, which is diagonalized with the previously introduced methods. In addition, the staggered magnetization is calculated. The obtained set of self consistent equations has to be evaluated numerically. Finally, the behavior of the critical point where our spin wave theory breaks down, is discussed.

5.1. Model

5.1.1. Mean field approximation

In total, we have to deal with four different types of bonds: One for each direction a, b and c and one for the next nearest neighbor exchange. All of them, except the ferromagnetic exchange parallel to the spin stripes (b-direction), are antiferromagnetic. Besides the average occupation number per lattice site

$$n := \left\langle b_i^\dagger b_i \right\rangle = \left\langle b_j^\dagger b_j \right\rangle , \tag{5.2a}$$

we define the following expectation values:

- in-plane antiferromagnetic nearest neighbor exchange perpendicular to the spin stripes (a-direction)

$$a_1 := \left\langle b_i^\dagger b_j^\dagger \right\rangle = \left\langle b_i \, b_j \right\rangle \tag{5.2b}$$

- interlayer antiferromagnetic nearest neighbor exchange (c-direction)

$$a_c := \left\langle b_i^\dagger b_j^\dagger \right\rangle = \left\langle b_i \, b_j \right\rangle \tag{5.2c}$$

- in-plane antiferromagnetic next nearest neighbor exchange

$$a_2 := \left\langle b_i^\dagger b_j^\dagger \right\rangle = \left\langle b_i \, b_j \right\rangle \tag{5.2d}$$

- in-plane ferromagnetic nearest neighbor exchange parallel to the spin stripes (b-direction)

$$f := \left\langle b_i^\dagger b_j \right\rangle = \left\langle b_j^\dagger b_i \right\rangle \tag{5.2e}$$

All other expectation values are zero. Again, we assume that all values are real. The mean field decoupling of the antiferromagnetic bonds (4.5) has already been introduced in Section 4.1. It is applied individually to all antiferromagnet bonds with the corresponding expectation values (5.2) and is not recapitulated again.

For ferromagnetic bonds, the scalar product of the spin operators is expressed in the Dyson-Maleev representation as

$$\mathbf{S}_i \cdot \mathbf{S}_j = S^2 - S\left(\hat{n}_i + \hat{n}_j - b_i^\dagger b_j - b_j^\dagger b_i\right) + \hat{n}_i\,\hat{n}_j - \frac{1}{2}\left(b_i^\dagger \hat{n}_i\, b_j + b_j^\dagger \hat{n}_j\, b_i\right) \tag{5.3}$$

because the spins are not rotated with respect to each other. Thus, the Wick decoupling of the quartic terms reads

$$\begin{aligned} \hat{n}_i\hat{n}_j &= b_i^\dagger b_i\, b_j^\dagger b_j \\ &\approx n\left(\hat{n}_i + \hat{n}_j\right) + f\left(b_i^\dagger b_j + b_j^\dagger b_i\right) - n^2 - f^2 \end{aligned} \tag{5.4a}$$

$$\begin{aligned} b_i^\dagger \hat{n}_i b_j &= b_i^\dagger b_i^\dagger b_i\, b_j \\ &\approx 2n b_i^\dagger b_j + 2f b_i^\dagger b_i - 2nf \end{aligned} \tag{5.4b}$$

$$\begin{aligned} b_j^\dagger \hat{n}_j b_i &= b_j^\dagger b_j^\dagger b_j\, b_i \\ &\approx 2n b_j^\dagger b_i + 2f b_j^\dagger b_j - 2nf. \end{aligned} \tag{5.4c}$$

Consequently, the decoupling of a ferromagnetic bilinear exchange term results in

$$\mathbf{S}_i \cdot \mathbf{S}_j\Big|_{\mathrm{MF}} = -\Big(\underbrace{S}_{O(S)} - \underbrace{(n-f)}_{O\left(S^0\right)}\Big)\left(\hat{n}_i + \hat{n}_j - b_i^\dagger b_j - b_j^\dagger b_i\right) + \text{const.}\,. \tag{5.5}$$

The constant terms are dropped in the upcoming steps. This is all we need for writing down the mean field Hamiltonian

$$\begin{aligned} H^{\mathrm{MF}} = {} & \frac{J_1}{2}(S-\alpha_1)\sum_{i,\delta_a}\left(\hat{n}_i + \hat{n}_{i+\delta_a} + b_i^\dagger b_{i+\delta_a}^\dagger + b_i\, b_{i+\delta_a}\right) \\ & - \frac{J_1}{2}(S-\beta)\sum_{i,\delta_b}\left(\hat{n}_i + \hat{n}_{i+\delta_b} - b_i^\dagger b_{i+\delta_b} - b_{i+\delta_b}^\dagger b_i\right) \\ & + \frac{J_c}{2}(S-\alpha_c)\sum_{i,\delta_c}\left(\hat{n}_i + \hat{n}_{i+\delta_c} + b_i^\dagger b_{i+\delta_c}^\dagger + b_i\, b_{i+\delta_c}\right) \\ & + \frac{J_2}{2}(S-\alpha_2)\sum_{i,\Delta}\left(\hat{n}_i + \hat{n}_{i+\Delta} + b_i^\dagger b_{i+\Delta}^\dagger + b_i\, b_{i+\Delta}\right) \end{aligned} \tag{5.6}$$

for the three dimensional collinear phase. The new parameters are defined as

$$\alpha_1 := n + a_1 \tag{5.7a}$$

$$\alpha_c := n + a_c \tag{5.7b}$$

$$\alpha_2 := n + a_2 \tag{5.7c}$$

$$\beta := n - f. \tag{5.7d}$$

The vectors δ_a, δ_b and δ_c connect nearest neighbors along the specific direction, Δ denotes the vectors between the four in-plane next nearest neighbors.

Replacing all operators with their Fourier transform (A.1), the mean field Hamiltonian is given in k-space by

$$\begin{aligned} H^{\mathrm{MF}} = & \frac{J_1}{2}(S-\alpha_1)\sum_{k,\delta_a}\left(2b_k^\dagger b_k + \mathrm{e}^{-i\delta_a k}\, b_k^\dagger b_{-k}^\dagger + \mathrm{e}^{i\delta_a k}\, b_k b_{-k}\right) \\ & - \frac{J_1}{2}(S-\beta)\sum_{k,\delta_a}\left(2 - \mathrm{e}^{-i\delta_b k} - \mathrm{e}^{i\delta_b k}\right) b_k^\dagger b_k \\ & + \frac{J_c}{2}(S-\alpha_c)\sum_{k,\delta_c}\left(2b_k^\dagger b_k + \mathrm{e}^{-i\delta_c k}\, b_k^\dagger b_{-k}^\dagger + \mathrm{e}^{i\delta_c k}\, b_k b_{-k}\right) \\ & + \frac{J_2}{2}(S-\alpha_2)\sum_{k,\Delta}\left(2b_k^\dagger b_k + \mathrm{e}^{-i\Delta k}\, b_k^\dagger b_{-k}^\dagger + \mathrm{e}^{i\Delta k}\, b_k b_{-k}\right). \end{aligned} \tag{5.8}$$

The δ_i and Δ sums yield cosines

$$\sum_{\delta_i} \mathrm{e}^{-i\delta_i k} = 2\cos k_i \tag{5.9a}$$

$$\sum_{\Delta} \mathrm{e}^{-i\Delta k} = 4\cos k_a \cos k_b, \tag{5.9b}$$

where k_i is the reciprocal lattice vector corresponding to the direction i. Next, we define the abbreviations

$$A_k := 2J_2(S-\alpha_2) + J_1(S-\alpha_1) + J_c(S-\alpha_c) + J_1(S-\beta)(\cos k_b - 1) \tag{5.10a}$$

$$B_k := J_1(S-\alpha_1)\cos k_a + J_c(S-\alpha_c)\cos k_c + 2J_2(S-\alpha_2)\cos k_a \cos k_b \tag{5.10b}$$

to simplify the Hamiltonian to

$$H^{\mathrm{MF}} = \sum_{k>0} 2A_k\left(b_k^\dagger b_k + b_{-k}^\dagger b_{-k}\right) + \sum_{k>0} 2B_k\left(b_k^\dagger b_{-k}^\dagger + b_k b_{-k}\right). \tag{5.11}$$

Inserting a bosonic Bogoliubov transformation (3.23), we get

$$\begin{aligned} H^{\mathrm{MF}} = & \sum_{k>0} 2\left[A_k\cosh 2\theta_k + B_k \sinh 2\theta_k\right]\left(\beta_k^\dagger\beta_k + \beta_{-k}^\dagger\beta_{-k}\right) \\ & + \sum_{k>0} 2\left[A_k\sinh 2\theta_k + B_k\cosh 2\theta_k\right]\left(\beta_k^\dagger\beta_{-k}^\dagger + \beta_k\beta_{-k}\right) \\ & + \sum_{k>0} 2\left[2A_k\sinh^2\theta_k + B_k\sinh 2\theta_k\right]. \end{aligned} \tag{5.12}$$

To eliminate the non-diagonal term, θ_k is fixed by the condition

$$\tanh 2\theta_k = -\frac{B_k}{A_k}. \tag{5.13}$$

Therewith, the spin wave dispersion is given as

$$\begin{aligned}\omega_k &:= 2\left[A_k \cosh 2\theta_k + B_k \sinh 2\theta_k\right] \\ &= 2\sqrt{A_k^2 - B_k^2},\end{aligned} \tag{5.14}$$

where

$$\sinh 2\theta_k = -\frac{B_k}{\sqrt{A_k^2 - B_k^2}} \tag{5.15a}$$

$$\cosh 2\theta_k = \frac{A_k}{\sqrt{A_k^2 - B_k^2}} \tag{5.15b}$$

have been used. As before, the constant term is identified as the mean field energy, which states

$$E^{\mathrm{MF}} = \sum_k \left(\sqrt{A_k^2 - B_k^2} - A_k\right). \tag{5.16a}$$

Consequently,

$$\frac{1}{N} E^{\mathrm{MF}} = \frac{1}{(2\pi)^3} \iiint_{\mathrm{BZ}} \mathrm{d}^3 k \, \left(\sqrt{A_k^2 - B_k^2} - A_k\right) \tag{5.16b}$$

is the mean field energy per spin in thermal limit.

All in all, the diagonal mean field Hamiltonian reads

$$H^{\mathrm{MF}} = \sum_k \omega_k \beta_k^\dagger \beta_k + E^{\mathrm{MF}}. \tag{5.17}$$

The Goldstone modes are now found at $k = (0,0,0)$ and $k = (1,0,1)$. The latter one is the magnetic ordering vector of the three dimensional collinear phase. In contrast to linear spin wave theory, the modes at $(0,1,0)$, $(1,1,1)$, $(0,1,1)$ and $(1,1,0)$ are gapped due to the renormalization of the exchange constants.

For the upcoming numerical evaluation, it is convenient to introduce the two parameters

$$x := \frac{J_1}{J_2} \tag{5.18a}$$

$$\mu := \frac{J_c}{J_1} \tag{5.18b}$$

and the dispersion $\bar{\omega}_k$ in units of J_2

$$\bar{\omega}_k := 2\sqrt{\bar{A}_k^2 - \bar{B}_k^2} \tag{5.19}$$

with

$$\bar{A}_k := 2\left(S - \alpha_2\right) + x\left(S - \alpha_1\right) + x\mu\left(S - \alpha_c\right) + x\left(S - \beta\right)\left(\cos k_b - 1\right) \tag{5.20a}$$

$$\bar{B}_k := x\left(S - \alpha_1\right)\cos k_a + x\mu\left(S - \alpha_c\right)\cos k_c + 2\left(S - \alpha_2\right)\cos k_a \cos k_b. \tag{5.20b}$$

5.1.2. Spin wave velocities

The dispersion (5.14) is expanded for small momenta

$$\omega_k^2 \approx v_a^2 k_a^2 + v_b^2 k_b^2 + v_c^2 k_c^2 \tag{5.21}$$

to derive the spin wave velocities

$$v_a = 2\sqrt{\left[2J_2\left(S-\alpha_2\right)+J_1\left(S-\alpha_1\right)+J_c\left(S-\alpha_c\right)\right]\left[2J_2\left(S-\alpha_2\right)+J_1\left(S-\alpha_1\right)\right]} \tag{5.22a}$$

$$v_b = 2\sqrt{\left[2J_2\left(S-\alpha_2\right)+J_1\left(S-\alpha_1\right)+J_c\left(S-\alpha_c\right)\right]\left[2J_2\left(S-\alpha_2\right)-J_1\left(S-\beta\right)\right]} \tag{5.22b}$$

$$v_c = 2\sqrt{\left[2J_2\left(S-\alpha_2\right)+J_1\left(S-\alpha_1\right)+J_c\left(S-\alpha_c\right)\right]J_c\left(S-\alpha_c\right)}. \tag{5.22c}$$

Hence, their ratios with respect to v_a read

$$\frac{v_b}{v_a} = \sqrt{\frac{2\left(S-\alpha_2\right)-x\left(S-\beta\right)}{2\left(S-\alpha_2\right)+x\left(S-\alpha_1\right)}} \tag{5.23a}$$

$$\frac{v_c}{v_a} = \sqrt{\frac{x\mu\left(S-\alpha_c\right)}{2\left(S-\alpha_2\right)+x\left(S-\alpha_1\right)}}. \tag{5.23b}$$

These ratios are important quantities for fitting the model to experimentally measured spin wave velocities. Mind the expression $2(S-\alpha_2)-x(S-\beta)$ in v_b because it might lead to unphysical imaginary spin wave velocities in b-direction.

5.1.3. Self-consistency equations

The self-consistency equations for the quantum correction parameters $\alpha_1, \alpha_2, \alpha_c$ and β are given by

$$\frac{1}{N}\frac{\partial E^{\mathrm{MF}}}{\partial \alpha_1} = -2J_1\alpha_1 \tag{5.24a}$$

$$\frac{1}{N}\frac{\partial E^{\mathrm{MF}}}{\partial \alpha_1} = 2J_1\beta \tag{5.24b}$$

$$\frac{1}{N}\frac{\partial E^{\mathrm{MF}}}{\partial \alpha_c} = -2J_c\alpha_c \tag{5.24c}$$

$$\frac{1}{N}\frac{\partial E^{\mathrm{MF}}}{\partial \alpha_2} = -4J_2\alpha_2. \tag{5.24d}$$

By differentiating the mean field energy per spin with respect to the parameters, we obtain the following set of self-consistency equations

$$\alpha_1 = \frac{1}{2}\frac{1}{(2\pi)^3}\iiint_{\mathrm{BZ}} \mathrm{d}^3k\, \frac{\bar{A}_k - \bar{B}_k \cos k_a}{\sqrt{\bar{A}_k^2 - \bar{B}_k^2}} - \frac{1}{2} \tag{5.25a}$$

$$\beta = -\frac{1}{2}\frac{1}{(2\pi)^3}\iiint_{\mathrm{BZ}} \mathrm{d}^3k\, \frac{\bar{A}_k \left(\cos k_b - 1\right)}{\sqrt{\bar{A}_k^2 - \bar{B}_k^2}} - \frac{1}{2} \tag{5.25b}$$

$$\alpha_c = \frac{1}{2}\frac{1}{(2\pi)^3}\iiint_{\mathrm{BZ}} \mathrm{d}^3k\, \frac{\bar{A}_k - \bar{B}_k \cos k_c}{\sqrt{\bar{A}_k^2 - \bar{B}_k^2}} - \frac{1}{2} \tag{5.25c}$$

$$\alpha_2 = \frac{1}{2}\frac{1}{(2\pi)^3}\iiint_{\mathrm{BZ}} \mathrm{d}^3k\, \frac{\bar{A}_k - \bar{B}_k \cos k_a \cos k_b}{\sqrt{\bar{A}_k^2 - \bar{B}_k^2}} - \frac{1}{2}, \tag{5.25d}$$

where $\int_{-\pi}^{\pi} \mathrm{d}u \cos u = 0$ was used to simplify the equation for β. Note that the numerators always vanish when the dispersion is gapless. Thus, the integrands never diverge.

5.1.4. Staggered magnetization

The *staggered magnetization* m_{st} is defined[1] as the expectation value of the spin operator S_i^z

$$m_{\mathrm{st}} := \langle S_i^z \rangle \, (-1)^{\sigma}\,, \tag{5.26}$$

where $\sigma = 0$ for $i \in A$ and $\sigma = 1$ for $i \in B$. The spins on sublattice B are rotated by an angle of π about the x-axis so that $S_i^z \to -S_i^z \;\forall\, i \in B$. Since the system is translationally invariant after the rotation on sublattice B, the prefactor of $(-1)^{\sigma}$ is not required anymore and the staggered magnetization simply reads

$$m_{\mathrm{st}} = S - \langle \hat{n}_i \rangle\,. \tag{5.27}$$

The expectation value $n := \langle \hat{n}_i \rangle$ is given by

$$\begin{aligned} n &= \frac{1}{N}\sum_i \left\langle b_i^\dagger b_i \right\rangle \\ &= \frac{1}{N}\sum_k \left\langle b_k^\dagger b_k \right\rangle \\ &= \frac{1}{N}\sum_k \left\langle \left(\beta_k^\dagger \cosh\theta_k + \beta_{-k} \sinh\theta_k\right)\left(\beta_k \cosh\theta_k + \beta_{-k}^\dagger \sinh\theta_k\right)\right\rangle. \end{aligned} \tag{5.28}$$

[1] Consistently, we would have to define $m_{\mathrm{st}} := |\langle S_i^z \rangle| \, (-1)^{\sigma}$ because of the definition $S_i^z = -S + \hat{n}_i$ in the Dyson-Maleev representation (3.7).

At zero temperature, $\langle \ldots \rangle$ is the ground state expectation value and only the highlighted operators contribute. Thus, the average occupation number per site is

$$\begin{aligned} n &= \frac{1}{N} \sum_k \sinh^2 \theta_k \\ &= \frac{1}{2N} \sum_k \Big(\underbrace{\sinh^2 \theta_k + \cosh^2 \theta_k}_{\cosh 2\theta_k} + \underbrace{\sinh^2 \theta_k - \cosh^2 \theta_k}_{-1} \Big) \\ &= \frac{1}{2N} \sum_k \left(\cosh 2\theta_k - 1 \right). \end{aligned} \tag{5.29}$$

The value of $\cosh 2\theta_k$ has already been determined in (5.15b). Therewith, the staggered magnetization (5.27) in thermodynamic limit reads

$$m_{\mathrm{st}} = S + \frac{1}{2} - \frac{1}{2} \frac{1}{(2\pi)^3} \iiint_{\mathrm{BZ}} \mathrm{d}^3 k \, \frac{\bar{A}_k}{\sqrt{\bar{A}_k^2 - \bar{B}_k^2}}. \tag{5.30}$$

In contrast to the set of self-consistency equations (5.25), the integrand of the staggered magnetization diverges at $k = (0,0,0)$ and $k = (1,0,1)$.

5.2. Numerics

The set of self-consistency equations (5.25) as well as the staggered magnetization (5.30) have to be evaluated numerically. The evaluation is implemented in a `C++` program, which uses standard Numerical recipes [82] routines. During the entire runtime of the program, the value of μ is fixed.

The multidimensional integration is broken up into repeated one dimensional integrations, which are realized either with Gaussian quadrature or Romberg's integration. In general, the integration in the Brillouin zone is reduced by symmetry to a cube with $0 \leq k_a \leq 1$, $0 \leq k_b \leq 1$ and $0 \leq k_c \leq 1$ because $\cos k_i$ is symmetric about $k_i = 0$. Furthermore, B_k^2 (5.20) is point symmetric about $(0.5, k_b, 0.5)$ in the k_a-k_c-plane so that the integration for k_c can be limited to $0 \leq k_c \leq (1 - k_a)$. The complete domain of integration is sketched in Fig. 5.2.

The nonlinear system of self-consistency equations is solved via a multi-dimensional root finding routine, more precisely *Broyden's multidimensional secant method*.

The program always starts with $x = 0$ in the two dimensional collinear phase, where $\alpha_1 = \alpha_c = \beta = n$ and the integration is reduced to two dimensions. In addition, it is sufficient to integrate k_a and k_b from 0 to 0.5 because the k-dependence of the integrand is $\propto (\cos k_a \cdot \cos k_b)^2$. The integral for α_2 is non-critical, whereas the integrand of the other parameters and the staggered magnetization m_{st} diverges at $k = (0,0)$. Thus, it has to be expanded and integrated analytically around $(0,0)$. The domain of integration is then split up in the expanded part and two rectangles, which are handled as usual with the numerical integration routines. For the expansion, a cube with side length $\Delta k = 10^{-3}$

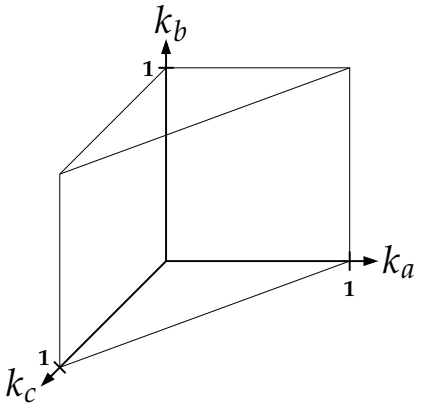

Fig. 5.2.: Domain of integration for the self-consistency equations and the staggered magnetization in the three dimensional collinear phase.

has proven to be suitable. A detailed description of the expansion and the decomposition of the domain of integration in two dimensions is given in Appendix D.1.

Then, the frustration x is de- or increased with a common increment of 10^{-3}. The procedure in each step is the following:

At first, the quantum correction parameters α_1, α_2, α_c and β are determined by Broyden's method. This requires an initial guess for the solutions for which the values from the previous step are used. Since there are no divergences in the integrands of the self-consistency equations (5.25), a special treatment of the equations is not required. After that, the staggered magnetization is calculated by numerical integration. The domain of integration is split into five parts and the integrand has to be expanded for small momenta. In contrast to the case for $x = 0$, the integration of the expansion is now also done numerically. Therefore, k is substituted by k^2 to eliminate the divergence. The complete description of the decomposition of the domain of integration and the expansion of the integrand of the staggered magnetization can be found in Appendix D.2. It is checked if the calculation of m_{st} was successful because the magnetization is strongly renormalized for higher values of x and thus vanishes very fast. If the numerics fails, the increment is decreased and the program jumps back to the previous value of x and continues with the new increment. Otherwise, it simply proceeds.

The calculations are stopped either when the program exceeds the predefined maximum value of x or the maximal number of steps, or when the magnetization cannot be calculated anymore. Furthermore, the spin wave velocity v_b (5.22) can vanish, which also causes the program to quit. Physically, this is related to the break down of the collinear phase driven by the vanishing spin wave velocity v_b. In detail, this is discussed in Section 5.4.

In each step, all exchange constants, the quantum correction parameters, the ratios of the spin wave velocities and the staggered magnetization are saved. In general, the visualization of the data is realized with `gnuplot`.

The correctness of the results is verified in various ways. At first, the program has to reproduce the results for the two dimensional collinear phase for $\mu = 0$. Secondly, the results of the two and three dimensional Néel phases are obtained when the frustration is switched off and all other exchange constants are set equal. Furthermore, the two dimensional result is independent of the chosen plane. This means that the result for the *a*-*b*-plane is identical to the one in the *a*-*c*-plane and so on in the isotropic case.

In addition, we implemented the same program in the Schwinger bosons representation. The deviation in the staggered magnetization between both representations is usually in the order of $10^{-12} - 10^{-8}$ due to numerical inaccuracies and a different handling of the diverging integrands. As expected, the deviation increases when the coupling ratio x approaches its critical value where the numerical calculations are stopped because of the growing influence of quantum fluctuations. This is a very nice proof of the equivalence of the equations derived with the Dyson-Maleev representation and the Schwinger bosons for the three dimensional collinear phase. For the two dimensional Néel phase (Chapter 4), the equivalence of both representations can easily be seen by comparing the renormalization of the exchange constant in the dispersion for the Dyson-Maleev (4.17) and Schwinger bosons representation (4.53a). One obtains the result

$$2\,(S - \alpha) \equiv A.$$

By inserting the corresponding equation for α (4.25) and A (4.50), it is verified that both equations are equivalent. The same equivalence can be obtained for the three dimensional collinear phase, which is not shown here.

5.3. Results & discussion

We now present and discuss the results for $S = 1/2$ and $S = 1$ for different interlayer couplings $\mu = J_c/J_1$.

For a better understanding of the upcoming results, some results of Section 5.4 are now anticipated. We define the *critical point* x_{crit} as the point where our spin wave theory for the collinear phase breaks down. We stress that our definition of the critical point does not necessarily have to be identical to the analytical point of the phase transition. Very likely, our spin wave theory breaks down before. The exact phase transition can be determined by a direct analysis of the Hamiltonian (5.1). We underline that the resolution of our numerics is limited. Hence, our program is only able to calculate all parameters up to close proximity to the critical point x_{crit} and not up to the point where the three dimensional collinear phase breaks down entirely. At the critical point, the three dimensional collinear phase is destabilized because of two different scenarios, which are indicated by the solid and dashed lines in all plots.

We call the first scenario, indicated by the solid lines, the *magnetization-driven scenario* where the staggered magnetization vanishes first and the spin wave velocities (5.22) always obtain finite values.

Due to the very sensitive numerics and the strongly growing renormalization of m_{st}, it is only possible to drive the staggered magnetization close to the point where it vanishes. However, m_{st} can be extrapolated to zero in the magnetization-driven scenario, which is explained in Section 5.4.

In the second scenario, the spin wave velocity v_b (5.22) vanishes first while the staggered magnetization (5.30) always stays finite. Thus, it is called the *velocity-driven scenario*, which is indicated by dashed lines in the upcoming plots.

Which scenario occurs depends on the interlayer coupling μ and the value of the spin S. In general, the magnetization-driven scenario is relevant for small values of μ and $S = 1/2$ or $S = 1$. In the case of strong interlayer couplings or $S \geq 1$, the velocity-driven scenario occurs. A more detailed discussion of the critical point follows in Section 5.4.

5.3.1. Spin $S = 1/2$

At first, we discuss the results for $S = 1/2$. The staggered magnetization (Fig. 5.3) first increases with growing $x = J_1/J_2$. While it approaches the critical point, the influence of the quantum fluctuations grows. Close to x_{crit}, the staggered magnetization is strongly renormalized and steeply descends. In the magnetization-driven scenario (solid lines), the curves are extrapolated to zero. The dashed curves, which belong to the velocity-driven scenario, end at a finite value of m_{st}. The transition between the magnetization- (solid lines) and velocity-driven (dashed lines) scenario can roughly be estimated between $\mu \approx 0.130$-0.135. For $\mu = 0.135$, the staggered magnetization (Fig. 5.3) as well as the ratio v_b/v_a (Fig. 5.4a) are both very close to zero when the calculation is stopped. This is an indicator for the transition between both scenarios.

With increasing interlayer coupling μ, the maximum value of the staggered magnetization increases and the critical point is shifted towards higher values of x. Thus, an increasing interlayer coupling μ stabilizes the collinear ordered phase, so that it persists over a wider range of x.

The ratios of the spin wave velocities are plotted in Fig. 5.4. The ratio v_b/v_a (Fig. 5.4a) decreases almost linearly and stays finite in the magnetization-driven scenario (solid lines), while it vanishes in the velocity-driven scenario (dashed lines). The interlayer coupling only influences the behavior close to x_{crit}. In the most part of the collinear ordered phase, the influence of μ is very small because v_a and v_b are dominated by the frustration $x = J_1/J_2$. The ratio v_c/v_a in Fig. 5.4b shows a square root like behavior $\propto \sqrt{x\mu}$, which is expected from Eq. (5.22c). The ratio v_c/v_a always stays finite and is only decreased due to fluctuations close to the critical point. In the velocity-driven scenario (dashed lines), an upturn of the curves can be observed which is likely caused by deficiencies in the numerics.

In Fig. 5.5, the quantities $(S - \tau)$ are plotted where τ are the quantum correction parameters α_1, α_2, α_c and β. The quantities $(S - \tau)$ correspond to the renormalization of the exchange constants $J_{1,2,c}$, which can be seen in the spin wave dispersion (5.14). The exchange perpendicular to the spin stripes (Fig. 5.5a) is only slightly influenced by the interlayer coupling. With increasing x, the renormalization increases monotonically. In contrast, the renormalization of the next nearest neighbor exchange (Fig. 5.5b) decreases monotonically. The influence of the interlayer coupling on the next nearest neighbor

exchange is very small throughout the most part of the collinear phase and is only important when x approaches the critical point. As expected, the renormalization of the interlayer exchange (Fig. 5.5c) is affected mostly by the interlayer coupling. The influence of the quantum fluctuations decreases with increasing x and the renormalization of the interlayer exchange becomes more constant. Parallel to the spin stripes (Fig. 5.5d), the exchange is strongly renormalized which leads to the vanishing spin wave velocity v_b in the velocity-driven scenario. We stress that in both scenarios the renormalization of all exchange constants obtains a finite value at the critical point. Only when both, the staggered magnetization and the spin wave velocity, vanish at the same value of x, one could assume that some exchange constants are renormalized to zero.

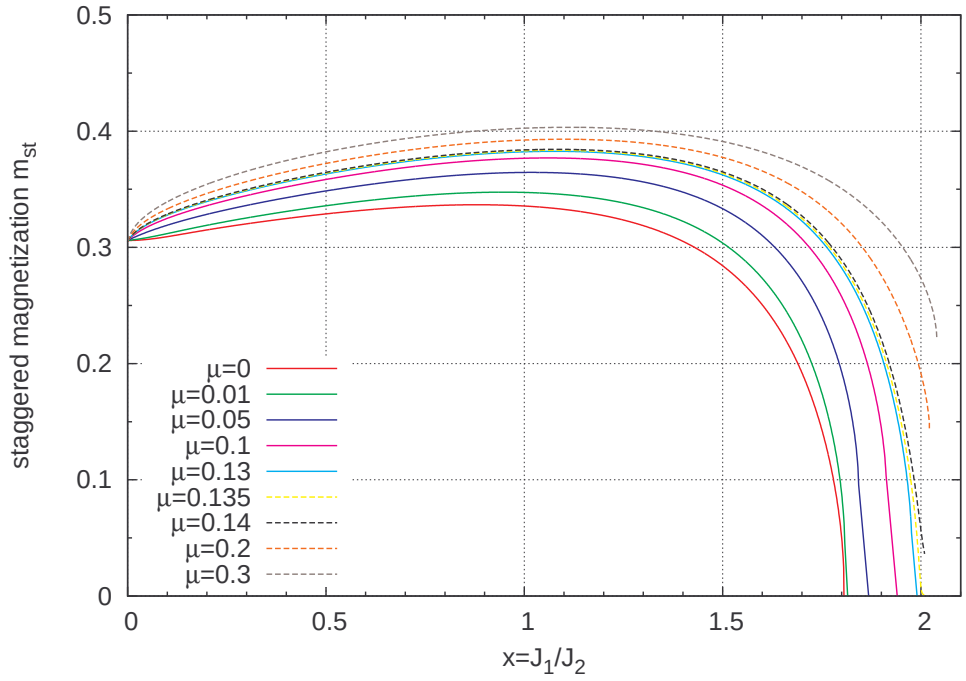

Fig. 5.3.: Staggered magnetization m_{st} as a function of x for $S = 1/2$. The solid lines corresponds to the magnetization-driven scenario and are extrapolated to zero. In the velocity-driven scenario (dashed lines), the staggered magnetization m_{st} always stays finite and positive.

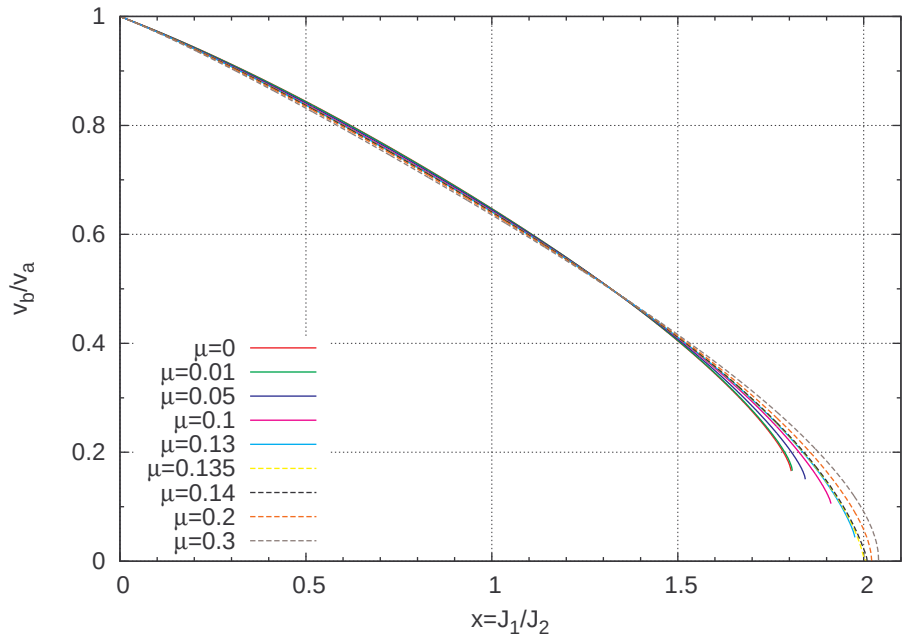

(a) v_b/v_a

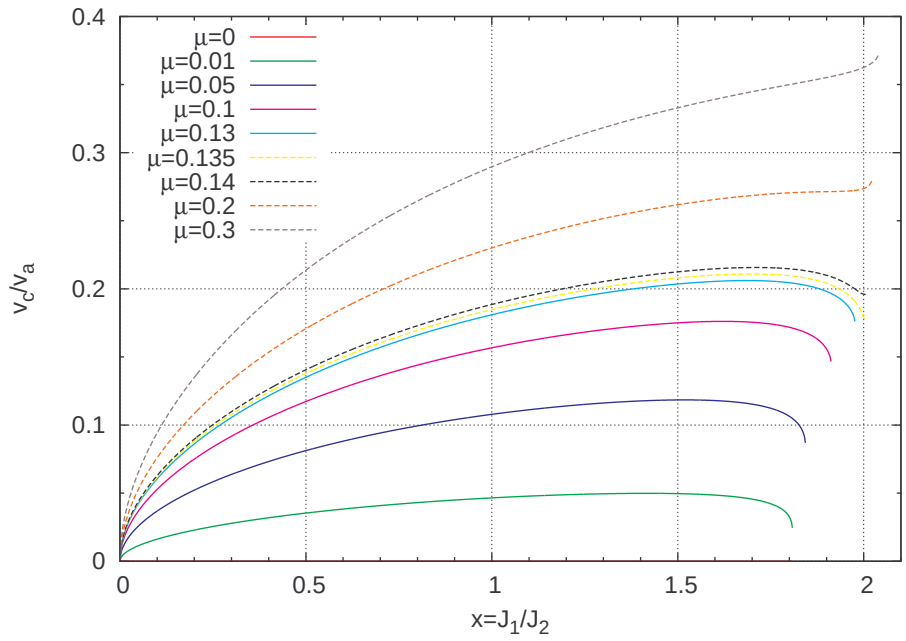

(b) v_c/v_a

Fig. 5.4.: Ratios of the spin wave velocities as a function of x for $S = 1/2$. The magnetization-driven scenario (solid lines) can clearly be distinguished from the velocity-driven scenario where the spin wave velocity v_b vanishes.

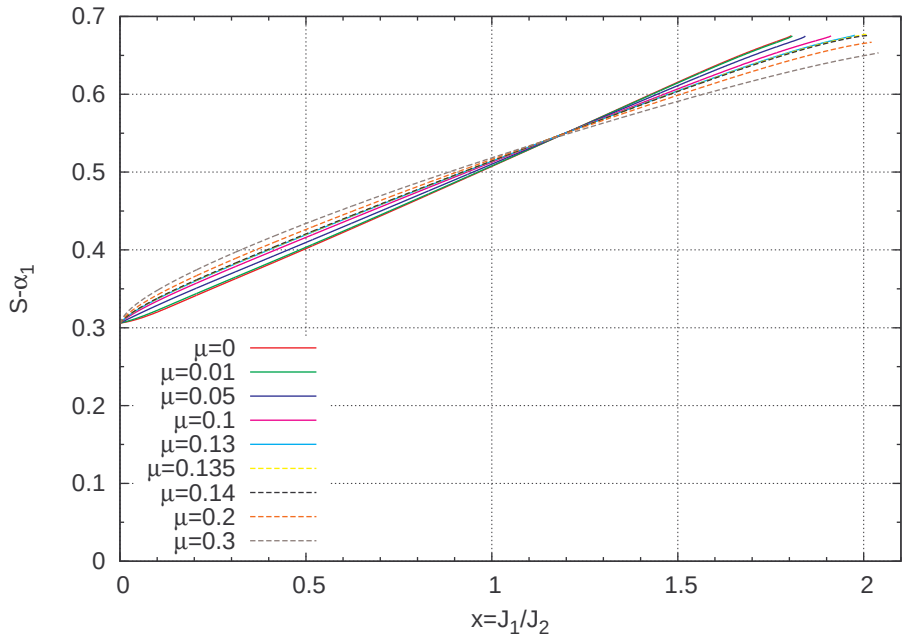

(a) Renormalization of the exchange perpendicular to the spin stripes.

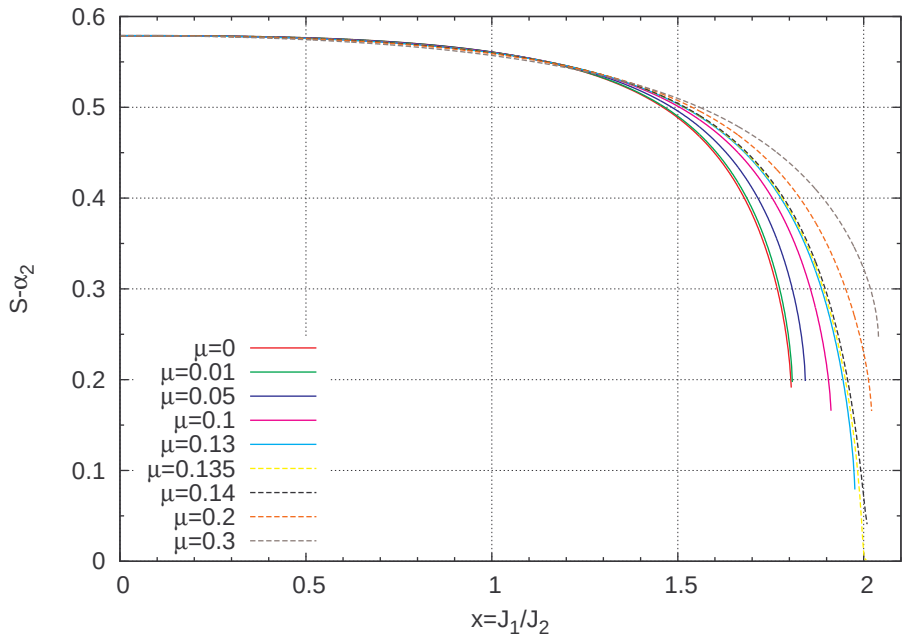

(b) Renormalization of the next nearest neighbor exchange.

Fig. 5.5.: Renormalization of the exchange constants as a function of x for $S = 1/2$. The solid lines correspond to the magnetization-driven scenario, the dashed lines to the velocity-driven scenario. All curves stop at finite values.

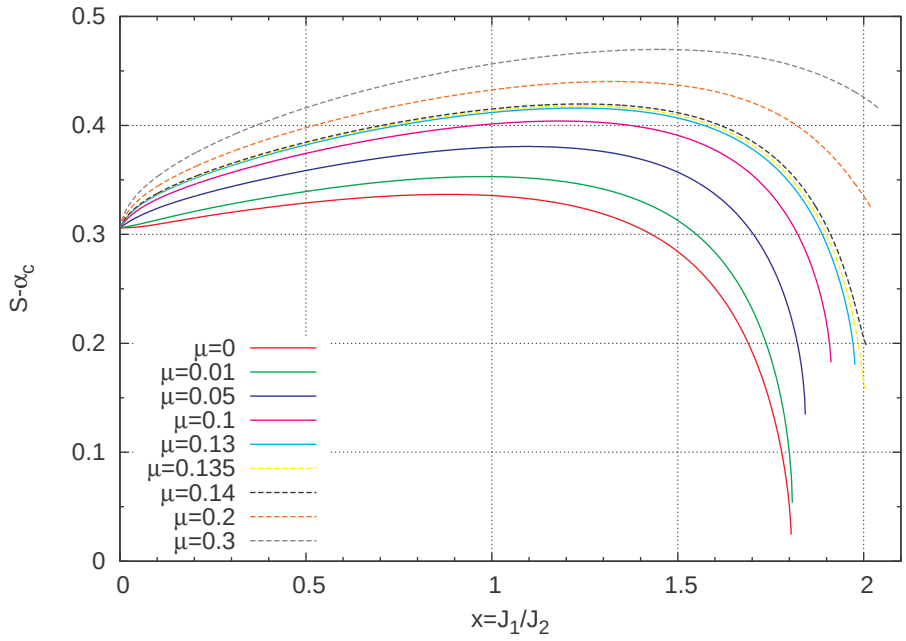

(c) Renormalization of the interlayer exchange.

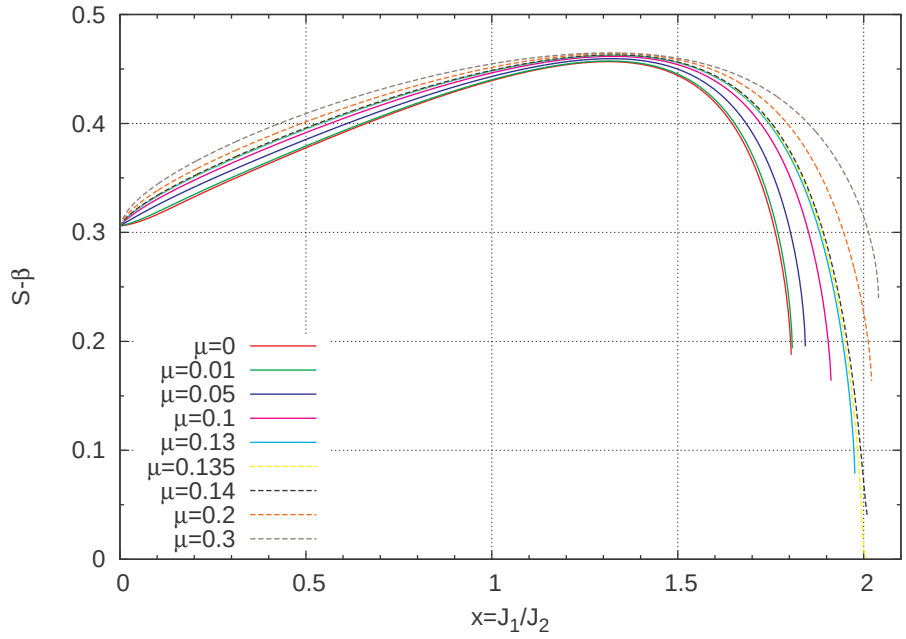

(d) Renormalization of the exchange parallel to the spin stripes.

Fig. 5.5.: (Continued) Renormalization of the exchange constants as a function of x for $S = 1/2$. The solid lines correspond to the magnetization-driven scenario, the dashed lines to the velocity-driven scenario. All curves stop at finite values.

5.3.2. Spin $S = 1$

Now we present the results for $S = 1$ for various interlayer couplings μ. The qualitatively behavior is identical to the one found for $S = 1/2$. Of course, the quantities are larger due to the larger value of the spin. As before, the magnetization-driven (solid lines) and velocity-driven scenario (dashed lines) are present.

The staggered magnetization in Fig. 5.6 is almost constant for the most part of the collinear phase. However, when the frustration x approaches its critical value, the staggered magnetization is strongly renormalized. Under the influence of an interlayer coupling, the staggered magnetization slightly increases and becomes stabilized even more for a wider range of x, but it drops faster upon approaching the critical point. Compared to the case of $S = 1/2$, the critical point is shifted less with increasing μ.

By regarding the staggered magnetization in Fig. 5.6 as well as the ratio v_b/v_a in Fig. 5.7a, the transition between the magnetization-driven and velocity-driven scenario can be estimated to occur close to $\mu \approx 0.01$. This is a much smaller value compared to $\mu \approx 0.13$ - 0.14 for $S = 1/2$. A detailed discussion follows in the next section.

The ratios v_b/v_a and v_c/v_a of the spin wave velocities are plotted in Fig. 5.7. No qualitatively difference compared to the case of $S = 1/2$ is observed. The ratio v_c/v_a (Fig. 5.7b) resembles the square root like behavior $\sim \sqrt{x\mu}$ as expected from Eq. (5.22c).

In Fig. 5.8, the renormalization of the exchange due to the quantum correction parameters α_1, α_2, α_c and β is plotted. While the exchange perpendicular to the spin stripes (Fig. 5.8a) is very stable and strictly monotonically increasing with increasing x, the exchange parallel to the stripes (Fig. 5.8b) is strongly renormalized, which causes that the spin wave velocity v_b vanishes in the velocity-driven scenario. As expected, the next nearest neighbor exchange (Fig. 5.8d) is also strongly renormalized with increasing frustration. In contrast to the exchange perpendicular to the spin stripes, it is strictly monotonically decreasing. For small interlayer couplings μ, the exchange along the c-direction (Fig. 5.8c) is still strongly renormalized, but it adopts a more and more constant value for stronger interlayer couplings.

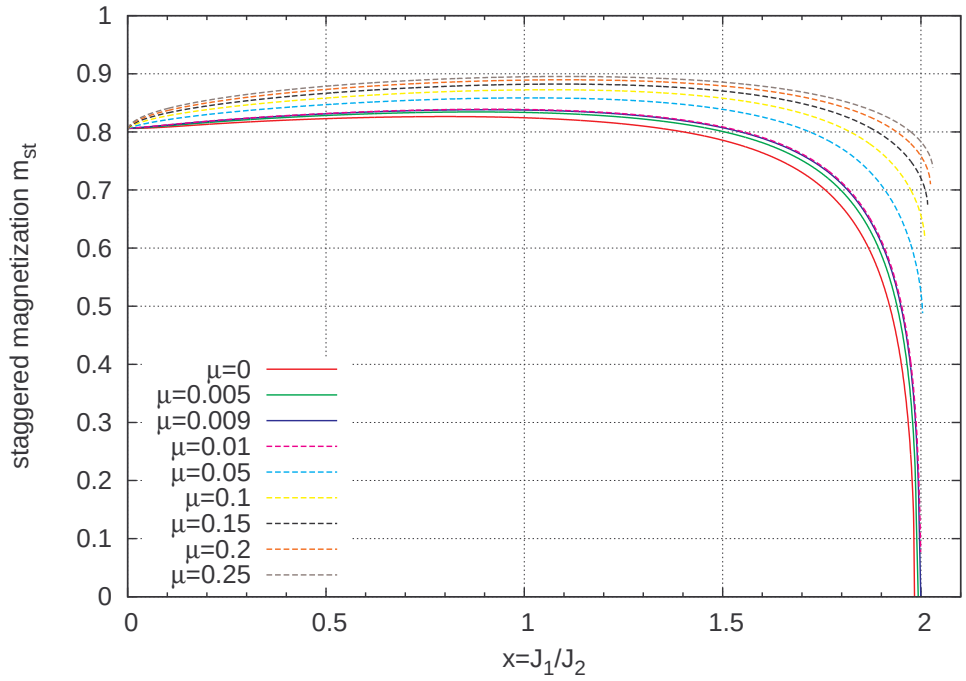

Fig. 5.6.: Staggered magnetization m_{st} as a function of x for $S = 1$. The solid lines belong to the magnetization-driven scenario and are extrapolated to zero. In the velocity-driven scenario (dashed lines), the staggered magnetization m_{st} always stays finite and positive.

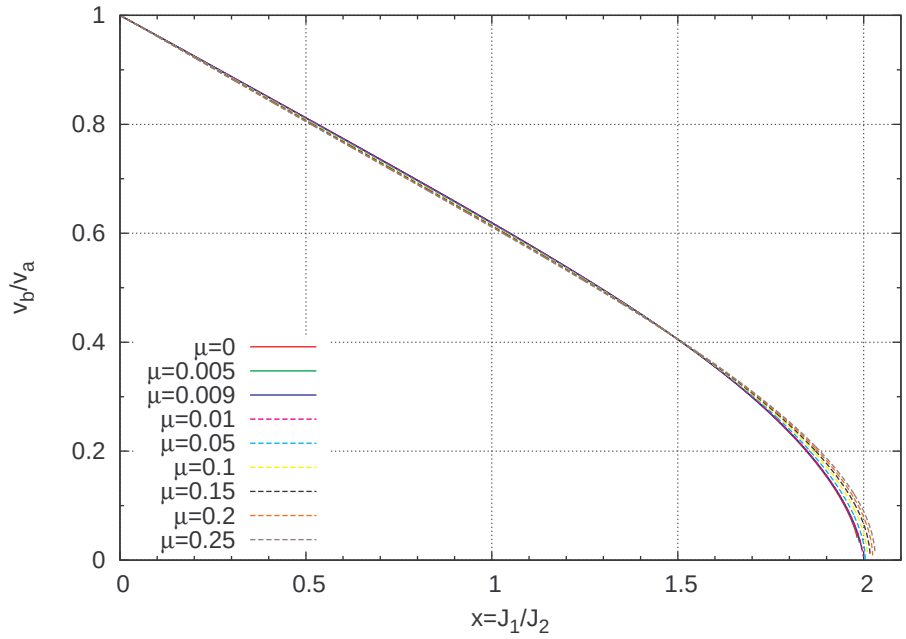

(a) v_b/v_a

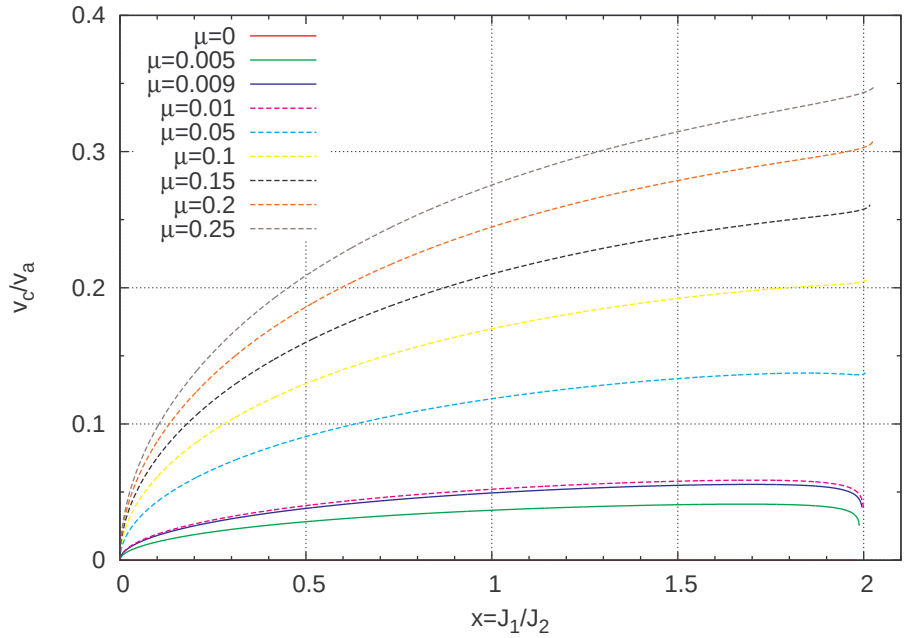

(b) v_c/v_a

Fig. 5.7.: Ratios of the spin wave velocities as a function of x for $S = 1$. The solid lines correspond to the magnetization-driven scenario, the dashed lines to the velocity-driven scenario.

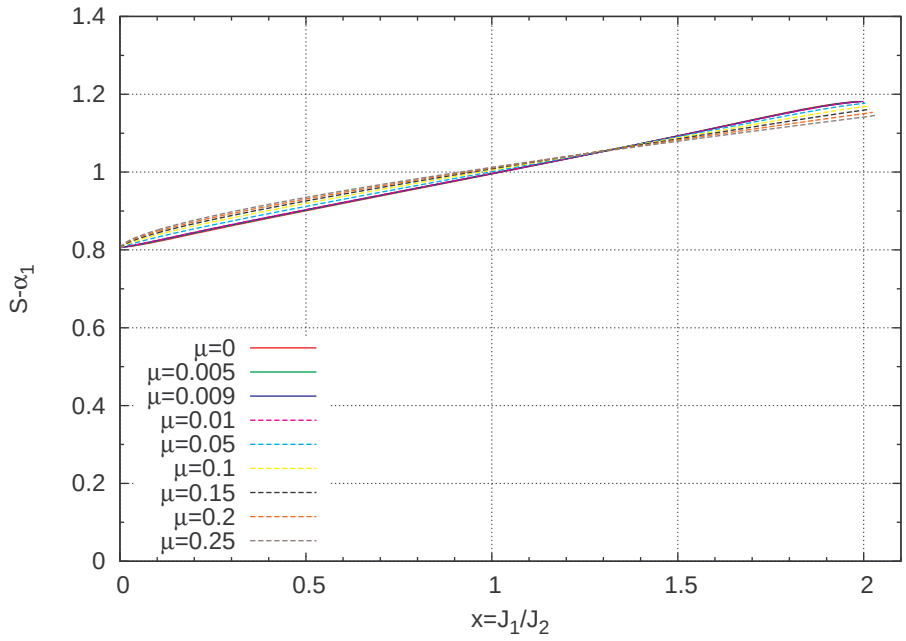

(a) Renormalization of the exchange perpendicular to the spin stripes.

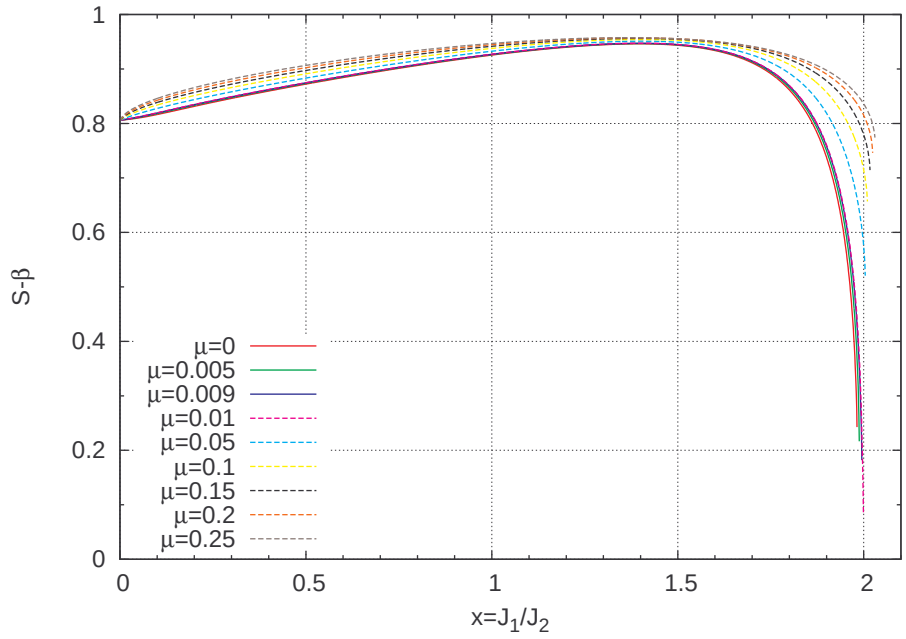

(b) Renormalization of the exchange parallel to the spin stripes.

Fig. 5.8.: Renormalization of the exchange constants as a function of x for $S = 1$. The solid lines correspond to the magnetization-driven scenario, the dashed lines to the velocity-driven scenario. All curves stop at finite values.

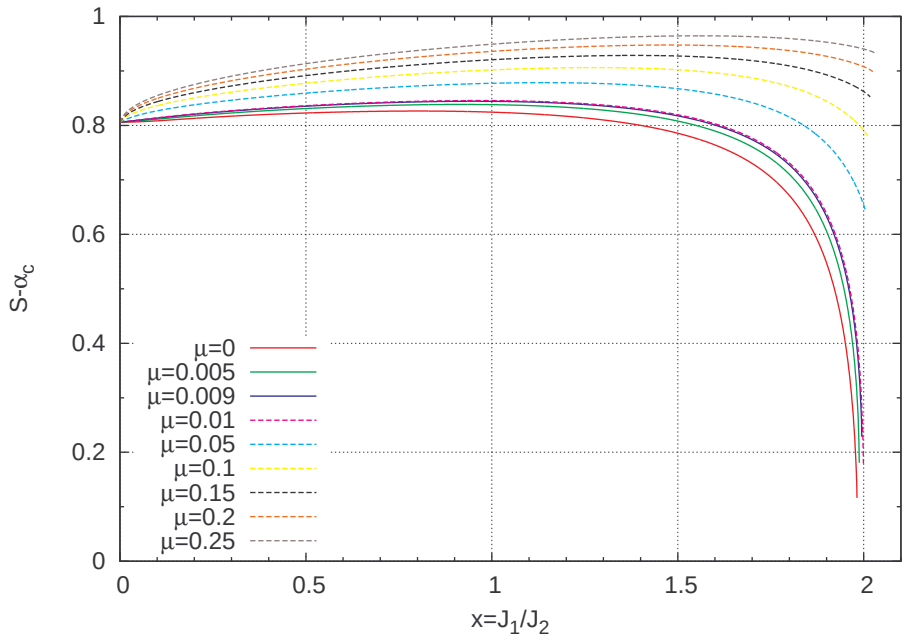

(c) Renormalization of the interlayer exchange.

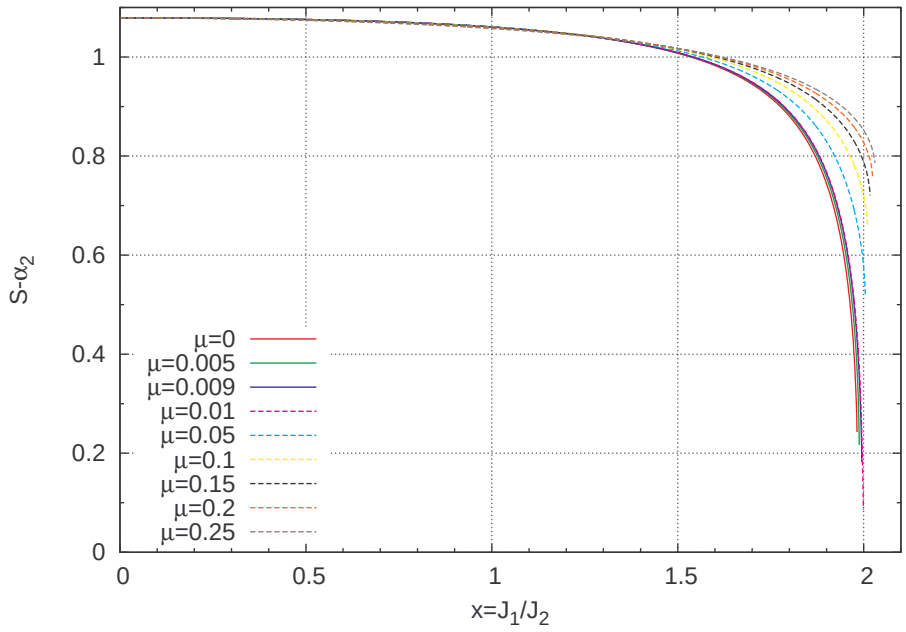

(d) Renormalization of the next nearest neighbor exchange.

Fig. 5.8.: (Continued) Renormalization of the exchange constants as a function of x for $S = 1$. The solid lines correspond to the magnetization-driven scenario, the dashed lines to the velocity-driven scenario. All curves stop at finite values.

5.4. Critical point

We discuss the critical point x_{crit}, more precisely the value of x where the spin wave theory for our model (5.1) breaks down. During the discussion of the numerical results in the previous section, it has already been mentioned that two scenarios depending on the coupling ratio $\mu = J_c/J_1$ exist. While in the magnetization-driven scenario the staggered magnetization vanishes first and the spin wave velocities stay finite and positive, the situation is vice versa in the velocity-driven scenario. At first, we tried to study the critical point numerically with multidimensional root finding, which failed because of the very sensitive numerics. The following results are based on a detailed study of the magnetization curves in dependence of different sets of parameters.

The existence of the two scenarios can easily be seen when the ratio v_b/v_a of the spin wave velocities is plotted as a function of the staggered magnetization. The results for $S = 1/2$ are shown in Fig. 5.9 and the results for $S = 1$ are shown in Fig. 5.10. The lower plots in these figures are magnifications of the upper plots for small values of v_b/v_a and m_{st}. To determine the value of $\mu = J_c/J_1$ where the transition between both scenarios occurs, curves for additional values of μ have been added to the lower plots. As before, curves belonging to the magnetization-driven scenario are represented by solid lines and curves in the velocity-driven scenario are represented by dashed lines.

We now discuss the result for $S = 1/2$ in detail. In terms of the parameter $x = J_1/J_2$, the plots have to be read from right to left. All curves in Fig. 5.6 decrease monotonically in the ratio v_b/v_a, while m_{st} first increases and then decreases. The scenarios are simply distinguished by the endpoint of the curves.

In the first scenario (solid lines), the ratio v_b/v_a always stays finite and positive and the staggered magnetization m_{st} goes to zero. Thus, we call this scenario the magnetization-driven scenario because the breakdown of the collinear phase is connected to the vanishing magnetic long range order. However, the influence of quantum fluctuations rapidly grows in the vicinity of the phase transition, which leads to a strong renormalization of the exchange. This fast renormalization lies beyond the resolution of our numerics. Broyden's algorithm fails to determine the correct quantum correction parameters, which results in unphysical dispersions where $\omega_k^2 < 0$ for some k-values. We stress that these k-values are not the gapless Goldstone modes. Thus, the numerics fails and the calculation is stopped before the staggered magnetization m_{st} drops to zero. Hence, we are only able to calculate the staggered magnetization up to a finite positive value. The curves of the magnetization-driven scenario in Fig. 5.9 are extrapolated to zero magnetization by fitting a polynomial of degree three to the last data points of the curves. Once more, we underline that the finite positive value of m_{st} is a consequence of the deficiencies in the numerics. Physically, the staggered magnetization has to drop to zero. In the two dimensional collinear phase ($\mu = 0$), the staggered magnetization can adopt any possible value due to the strong renormalization and the integral in (5.30) diverges logarithmically for $x \to x_{\text{crit}}$.

Following a suggestion of Smerald and Shannon [83], an additional coupling between the collinear ordered planes cuts the logarithmic divergence. Thus, in three dimensions the staggered magnetization at the critical point x_{crit} cannot adopt any arbitrary value anymore. Instead, the staggered magnetization adopts a finite value depending on the interlayer coupling μ. If the value of μ is not too

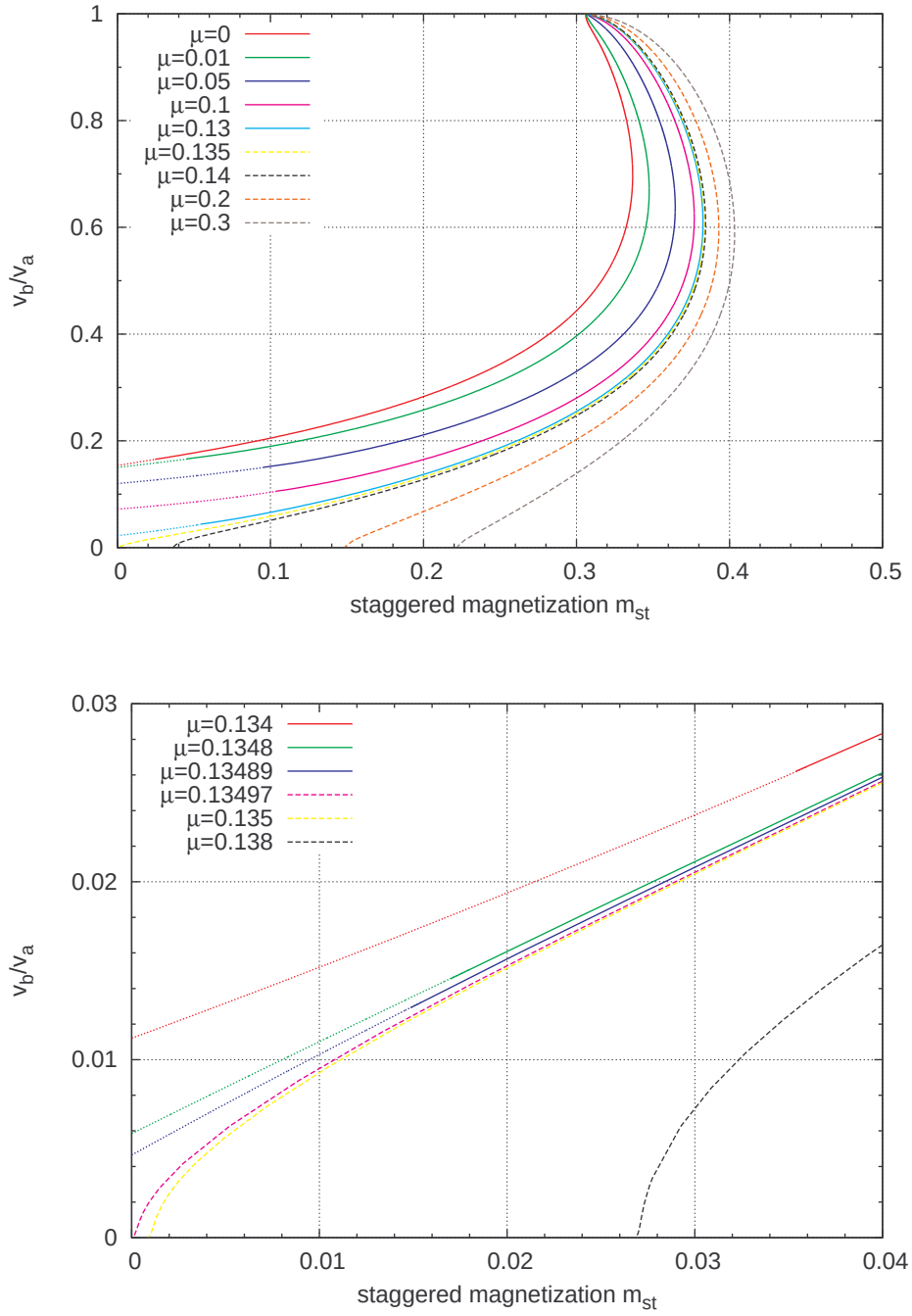

Fig. 5.9.: Ratio v_b/v_a as a function of the staggered magnetization for $S = 1/2$. The solid lines correspond to the magnetization-driven scenario, the dashed lines to the velocity-driven scenario. The dotted lines are extrapolations in the magnetization-driven scenario. The kinks in the dashed lines occur when the increment of x is decreased during the numerical calculation.

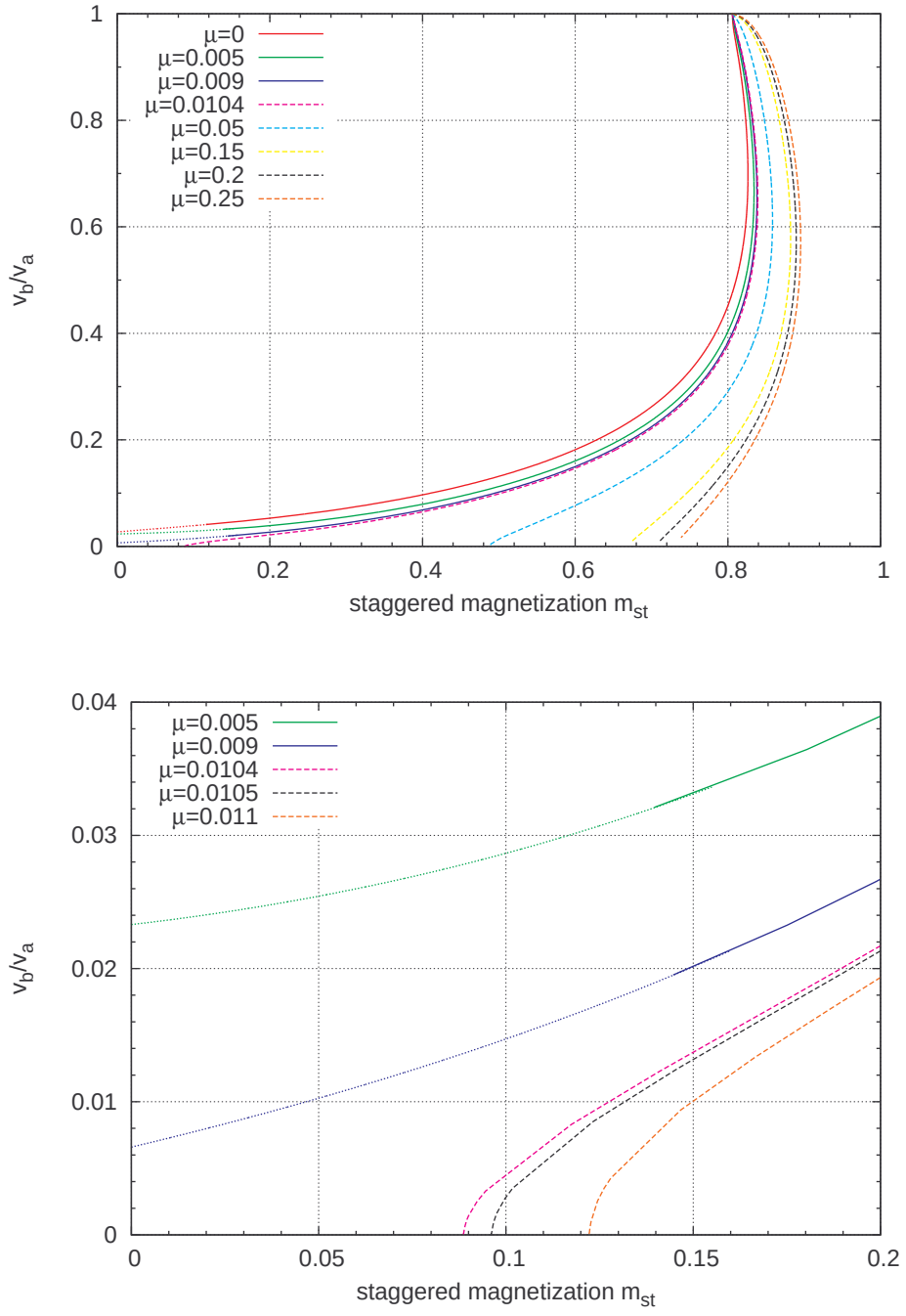

Fig. 5.10.: Ratio v_b/v_a as a function of the staggered magnetization for $S = 1$. The solid lines correspond to the magnetization-driven scenario, the dashed lines to the velocity-driven scenario. The dotted lines are extrapolations in the magnetization-driven scenario. The kinks in the dashed lines occur when the increment of x is decreased during the numerical calculation.

large, it will still be possible to drive the magnetization to zero. According to Smerald and Shannon, the minimum value of the staggered magnetization at the critical point is connected to the maximum possible interlayer coupling ratio μ_{max} via the relation

$$\mu_{\text{max}} = C \cdot \exp\left(\xi m_{\text{st}}\right). \tag{5.31}$$

This relation can be derived by expanding the integrand in the staggered magnetization (5.30) because the integral is dominated by the spin waves near the magnetic ordering vector for antiferromagnetic $J_1 > 0$. The expanded integrand is integrated in three dimensions up to a large momentum cutoff. Therewith, one obtains the relation (5.31) which can be used to extrapolate the curves in the magnetization-driven scenario to zero.

We want to determine the interlayer coupling μ so that the staggered magnetization m_{st} vanishes at x_{crit}. Therefore, m_{st} and μ are plotted for this fixed value of x_{crit} and the relation (5.31) is fitted to the last four or five data points. The value of μ, for which the staggered magnetization at x_{crit} vanishes, is determined by (5.31) to $\mu(m_{\text{st}} = 0) = C$. By repeating this procedure for different values of x, one obtains data points (x_{crit}, μ) which resemble the dependence of the critical point on the interlayer coupling μ. The data pairs (x_{crit}, μ) are plotted for $S = 1/2$ in Fig. 5.11a. The observed dependence is almost linear.

Returning to Fig. 5.9, we now discuss the dashed lines which correspond to the second scenario. We call it the velocity-driven scenario because the spin wave velocity v_b vanishes first and the calculation of the staggered magnetization m_{st} is truncated at a finite positive value. The phase transition is driven by the vanishing spin wave velocity, which leads to the breakdown of the collinear phase. The finite positive value of the staggered magnetization is somehow surprising because a magnetic long range order still persists when the collinear phase ceases to exist. The possibility of a vanishing v_b can also be expected from Eq. (5.22b). In the velocity-driven scenario, the numerics is not as sensitive as in the magnetization-driven scenario. The dashed curves in Fig. 5.9 are calculated down to small values of v_b/v_a. As $v_b^2 \propto 2J_2(S - \alpha_2) - J_1(S - \beta)$, imaginary values for v_b are possible which cause the numerics to abort. We stress that the velocity-driven scenario only occurs in three dimensions because in the two dimensional system m_{st} diverges for $x \to x_{\text{crit}}$.

In the case of $S = 1/2$, the transition from the magnetization- to the velocity-driven scenario seems to occur between $0.134 \lesssim \mu \lesssim 0.135$, which can roughly be estimated in the lower plot of Fig. 5.9. Starting from the magnetization-driven scenario with $\mu = 0.134$, one observes that the curves move down the y-axis and approach the origin with increasing μ. Thus, the magnetization-driven scenario stretches across the range of approximately $0 \leq \mu \lesssim 0.134$. The exact value of μ where the transition occurs, could be captured by the curve ending in the origin. If the interlayer coupling is further increased, the curves enter the velocity-driven scenario where they stop on the x-axis.

In addition, we briefly discuss the plots for $S = 1$ which are shown in Fig. 5.10. The qualitatively behavior is identical to the case of $S = 1/2$. The difference is observed in the range of the magnetization-driven scenario. By tracing the curves in the lower plot of Fig. 5.10, the transition between both scenarios can be estimated roughly at $\mu \approx 0.01$. Thus, the magnetization-driven scenario for $S = 1$ persists in the range of $0 \leq \mu \lesssim 0.01$, which is much smaller compared to the case for $S = 1/2$. The

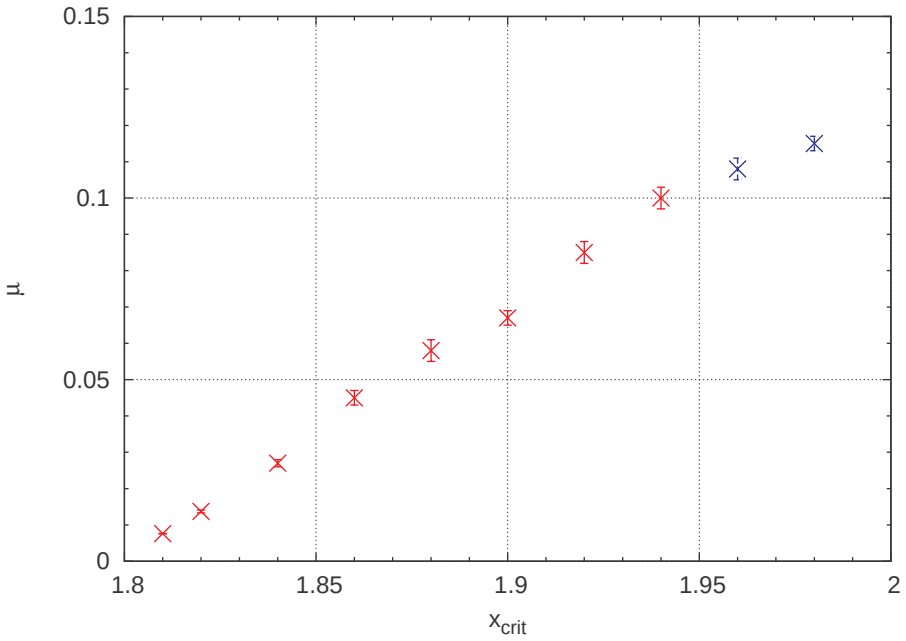

(a) $S = 1/2$

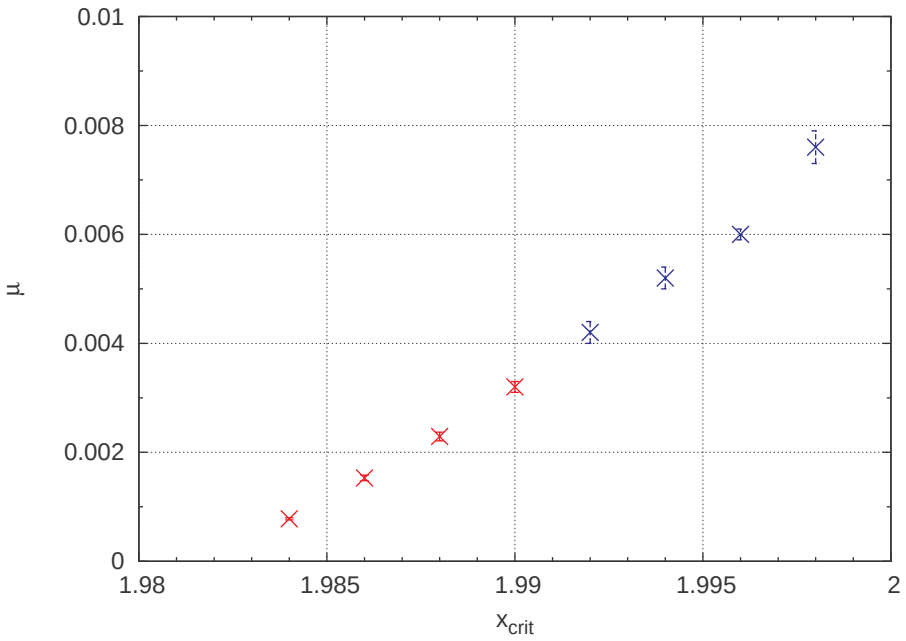

(b) $S = 1$

Fig. 5.11.: Dependence of the critical point x_{crit} on the interlayer coupling μ. For extracting the blue data points, curves from the velocity-driven scenario had to be used. The error bars are the standard deviation determined by the fit of the relation (5.31).

extrapolated dependence of the critical point x_{crit} on the interlayer coupling μ in the magnetization-driven scenario is shown in Fig. 5.11. As in the case of $S = 1/2$, the dependence is almost linear.

Keeping the staggered magnetization curves 5.6 and 5.3 in mind, it is peculiar that the transition between the scenarios is in both cases located at values of μ where the critical point crosses $x \approx 2.0$. Although we cannot provide a satisfying reason for the observed behavior, we underline that in the classical limit of the two dimensional frustrated Heisenberg model on the square lattice a phase transition is located at $x = 2$ [84].

The question arises, what happens for larger spins $S > 1$. Therefore, the ratio v_b/v_a in the two dimensional collinear phase is again plotted as a function of m_{st} in Fig. 5.12, this time for various values of the spin. We observe for $S \geq 3/2$ that the magnetization-driven scenario does not appear and the velocity-driven scenario becomes the standard scenario. Hence, the breakdown of the collinear phase is always driven by the vanishing spin wave velocity v_b for $S \geq 3/2$. At first, this might be surprising, but it can merely be seen as a consequence of the shrinking range of the magnetization-driven scenario, which even reduces strongly from $S = 1/2$ to $S = 1$.

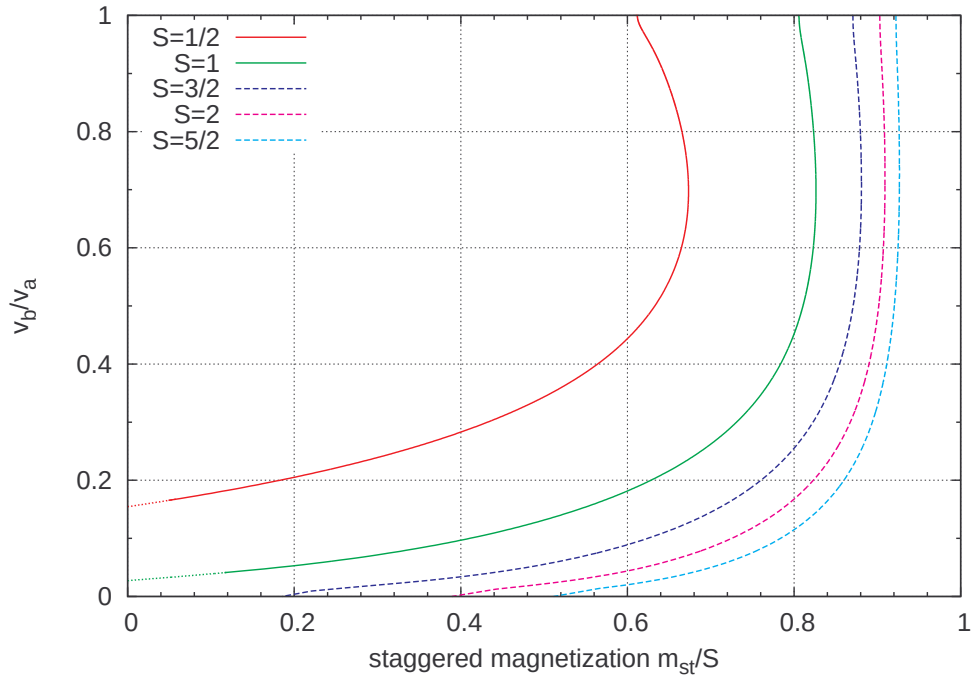

Fig. 5.12.: Ratio v_b/v_a as a function of m_{st} renormalized to the spin S. The dominance of the velocity-driven scenario is obvious. The solid lines correspond to the magnetization-driven scenario, the dashed lines to the velocity-driven scenario. The dotted lines are extrapolations in the magnetization-driven scenario.

6. 3D collinear phase with biquadratic exchange

The general existence of a biquadratic exchange term for $S \geq 1$ and its relevance for the iron pnictides has been discussed in the introduction in Section 2.7. In the last chapter, it was shown that the renormalization due to quantum mechanical fluctuations leads to an anisotropic exchange within the *a*-*b*-plane. Perpendicular to the spin stripes, the effective exchange is strengthened up to 20%, while parallel to the spin stripes the effective exchange is weakened. But in case of the iron pnictides, neutron scattering studies [9, 10] revealed a much stronger anisotropy within the collinear ordered layers.

Thus, we now study the Hamiltonian

$$H = J_1 \sum_{\langle i,j \rangle} \mathbf{S}_i \cdot \mathbf{S}_j + J_2 \sum_{\langle\langle i,j \rangle\rangle} \mathbf{S}_i \cdot \mathbf{S}_j + J_c \sum_{[i,j]} \mathbf{S}_i \cdot \mathbf{S}_j - J_{\mathrm{bq}} \sum_{\langle i,j \rangle} \left(\mathbf{S}_i \cdot \mathbf{S}_j \right)^2 , \tag{6.1}$$

where an in-plane biquadratic exchange ($J_{\mathrm{bq}} > 0$) has been introduced. The biquadratic exchange is well known from the previously discussed Néel phase in Chapter 4. Based on these result, we now have to decouple the exchange for ferromagnetic bonds parallel to the spin stripes. Luckily, no further analytical calculations are required. Hence, we can directly discuss the results, which show an increasing anisotropy for the effective in-plane exchange constants (6.22).

6.1. Model

6.1.1. Mean field approximation

The decoupling of the biquadratic exchange for antiferromagnetic bonds in terms of the Dyson-Maleev representation has already been discussed in Chapter 4. With (4.10) and (4.11), the mean field Hamiltonian for nearest neighbor exchange perpendicular to the spin stripes is written as

$$H_{\perp}^{\mathrm{MF}} = J_{1a}\left(\alpha_1\right)\left(S - \alpha_1\right) \sum_{\langle i,j \rangle} \left(\hat{n}_i + \hat{n}_j + b_i^{\dagger} b_j^{\dagger} + b_i \, b_j \right) , \tag{6.2}$$

where

$$J_{1a}\left(\alpha_1\right) := J_1 + J_{\mathrm{bq}} \frac{2S^3 - 2S^2(1 + 5\alpha_1) + S(18\alpha_1^2 + 8\alpha_1 + 1) - 12\alpha_1^3 - 9\alpha_1^2 - 2\alpha_1}{S - \alpha_1} \tag{6.3}$$

has been introduced for convenience. We use the same expectation values as defined in Section 5.1.1.

In addition, we introduce the decoupling for ferromagnetic bonds parallel to the spin stripes. In the Dyson-Maleev representation (3.7), the biquadratic term reads

$$\begin{aligned}\left(\mathbf{S}_i \cdot \mathbf{S}_j\right)^2\Big|_{\parallel} &= S^4 \\ &\quad - 2S^3\left(\hat{n}_i + \hat{n}_j - \hat{F}_0\right) \\ &\quad + S^2\left[\hat{n}_i^2 + \hat{n}_j^2 + 4\hat{n}_i\hat{n}_j + \hat{F}_0^2 - \left(\hat{n}_i + \hat{n}_j\right)\hat{F}_0 - \hat{F}_0\left(\hat{n}_i + \hat{n}_j\right) - \hat{F}_0'\right] \\ &\quad + S\left[-2\left(\hat{n}_i\hat{n}_j^2 + \hat{n}_i^2\hat{n}_j\right) + \hat{n}_i\hat{n}_j\hat{F}_0 + \hat{F}_0\hat{n}_i\hat{n}_j\right. \\ &\quad \left. + \frac{1}{2}\left(-\hat{F}_0\,\hat{F}_0' - \hat{F}_0'\hat{F}_0 + \left(\hat{n}_i + \hat{n}_j\right)\hat{F}_0' + \hat{F}_0'\left(\hat{n}_i + \hat{n}_j\right)\right)\right] \\ &\quad + \hat{n}_i^2\hat{n}_j^2 + \frac{1}{4}\hat{F}_0'^2 - \frac{1}{2}\left(\hat{n}_i\,\hat{n}_j\,\hat{F}_0' + \hat{F}_0'\hat{n}_i\,\hat{n}_j\right),\end{aligned} \tag{6.4}$$

where

$$\hat{F}_0 := b_i^\dagger b_j + b_j^\dagger b_i \tag{6.5a}$$

$$\hat{F}_0' := b_i^\dagger \hat{n}_i\, b_j + b_j^\dagger \hat{n}_j\, b_i\,. \tag{6.5b}$$

Wick's theorem is applied to all terms of order S^2 and lower. Consequently, the biquadratic exchange term decouples as

$$\begin{aligned}\left(\mathbf{S}_i \cdot \mathbf{S}_j\right)^2\Big|^{\mathrm{MF}} &= -\left[2S^3 - 2S^2\left(1 + 5\beta\right) + S(18\beta^2 + 8\beta) - 12\beta^3 - 9\beta^2 - \beta\right] \\ &\quad \cdot\left(\hat{n}_i + \hat{n}_j - \hat{F}_0\right) + \text{const.}\,.\end{aligned} \tag{6.6}$$

The single prefactors of each term are listed in Appendix B.2. Besides the parameter β, the decouplings of the antiferromagnetic and ferromagnetic terms are very similar. In the case of a ferromagnet, the term $+1$ in $S(18\beta^2 + 8\beta)$ is lacking and the linear contribution of β in $\mathcal{O}(S^0)$ does not have the prefactor two in Eq. (6.6).

In case of the antiferromagnet, the data from the exact diagonalization and the series expansion provided a welcomed check of the mean field approximation. Unfortunately, there is no data available to perform the same check for the ferromagnet. However, the lack of the term $+1$ in order S can roughly be checked by regarding the energy difference between an ideal ferromagnetic ground state where all spins are parallel and an excited state with $\Delta m = 1$. For bilinear and biquadratic exchange, the Dyson-Maleev formalism reproduces the exact result, which is

$$\Delta E = JS + J_{\mathrm{bq}}\left(2S^3 - 2S^2\right) \tag{6.7}$$

for a bond with one excitation. The exact result is obtained by simply applying the spin ladder operators (3.1a) to the states. The ground state of a ferromagnet is free from fluctuations. Hence, $\beta = 0$ leads to the same result within the Dyson-Maleev representation and the existence of a constant term in $\mathcal{O}(S)$, precisely in $S(18\beta^2 + 8\beta)$, is excluded.

By inserting the decoupling of the bilinear and biquadratic exchange, one derives the mean field Hamiltonian for the ferromagnetic exchange parallel to the spin stripes

$$H_{\parallel}^{\mathrm{MF}} = J_{1b}\left(\beta\right)\left(S-\beta\right)\sum_{\langle i,j\rangle}\left(\hat{n}_i + \hat{n}_j - b_i^{\dagger}b_j - b_j^{\dagger}b_i\right), \tag{6.8}$$

where

$$J_{1b}\left(\beta\right) := J_1 + J_{\mathrm{bq}}\frac{2S^3 - 2S^2\left(1+5\beta\right) + S(18\beta^2+8\beta) - 12\beta^3 - 9\beta^2 - \beta}{S-\beta} \tag{6.9}$$

has been introduced.

No further steps are required. We simply write down the diagonal Hamiltonian by replacing the nearest neighbor exchange constant J_1 by the effective couplings $J_{1a}\left(\alpha_1\right)$ and $J_{1b}\left(\beta\right)$, respectively. Thus, we obtain the diagonal Hamiltonian as

$$H^{\mathrm{MF}} = \sum_k \omega_k \beta_k^{\dagger}\beta_k + E^{\mathrm{MF}}, \tag{6.10}$$

where

$$\omega_k := 2\sqrt{A_k^2 - B_k^2} \tag{6.11}$$

$$E^{\mathrm{MF}} := \sum_k \left(\sqrt{A_k^2 - B_k^2} - A_k\right) \tag{6.12}$$

with

$$A_k := 2J_2\left(S-\alpha_2\right) + J_{1a}\left(\alpha_1\right)\left(S-\alpha_1\right) + J_c\left(S-\alpha_c\right) + J_{1b}\left(\beta\right)\left(S-\beta\right)\left(\cos k_b - 1\right) \tag{6.13a}$$

$$B_k := J_{1a}\left(\alpha_1\right)\left(S-\alpha_1\right)\cos k_a + J_c\left(S-\alpha_c\right)\cos k_c + 2J_2\left(S-\alpha_2\right)\cos k_a \cos k_b. \tag{6.13b}$$

As expected, the Goldstone modes are still located at $(0,0,0)$ and $(1,0,1)$.

For convenience, it is once again helpful to express all quantities in units of J_2. Therefore, the relative exchange constants

$$x_{1a}\left(\alpha_1\right) := x + x\nu\frac{2S^3 - 2S^2(1+5\alpha_1) + S(18\alpha_1^2 + 8\alpha_1 + 1) - 12\alpha_1^3 - 9\alpha_1^2 - 2\alpha_1}{S-\alpha_1} \tag{6.14a}$$

$$x_{1b}\left(\beta\right) := x + x\nu\frac{2S^3 - 2S^2\left(1+5\beta\right) + S(18\beta^2+8\beta) - 12\beta^3 - 9\beta^2 - \beta}{S-\beta} \tag{6.14b}$$

with

$$\nu := \frac{J_{\mathrm{bq}}}{J_1} \tag{6.15}$$

are introduced. Consequently, A_k and B_k are mapped to

$$\bar{A}_k := 2\left(S-\alpha_2\right) + x_{1a}\left(\alpha_1\right)\left(S-\alpha_1\right) + x\mu\left(S-\alpha_c\right) + x_{1b}\left(\beta\right)\left(S-\beta\right)\left(\cos k_b - 1\right) \tag{6.16a}$$

$$\bar{B}_k := x_{1a}\left(\alpha_1\right)\left(S-\alpha_1\right)\cos k_a + x\mu\left(S-\alpha_c\right)\cos k_c + 2\left(S-\alpha_2\right)\cos k_a \cos k_b. \tag{6.16b}$$

6.1.2. Spin wave velocities

The spin wave velocities along the crystal axis are obtained by replacing the exchange constant J_1 in Eq. (5.22) by the effective couplings $J_{1a}(\alpha)$ (6.3) or $J_{1b}(\beta)$ (6.9), respectively:

$$v_a = 2\sqrt{\left[2J_2\left(S-\alpha_2\right) + J_{1a}\left(\alpha_1\right)\left(S-\alpha_1\right) + J_c\left(S-\alpha_c\right)\right]\left[2J_2\left(S-\alpha_2\right) + J_{1a}\left(\alpha_1\right)\left(S-\alpha_1\right)\right]} \tag{6.17a}$$

$$v_b = 2\sqrt{\left[2J_2\left(S-\alpha_2\right) + J_{1a}\left(\alpha_1\right)\left(S-\alpha_1\right) + J_c\left(S-\alpha_c\right)\right]\left[2J_2\left(S-\alpha_2\right) - J_{1b}\left(\beta\right)\left(S-\beta\right)\right]} \tag{6.17b}$$

$$v_c = 2\sqrt{\left[2J_2\left(S-\alpha_2\right) + J_{1a}\left(\alpha_1\right)\left(S-\alpha_1\right) + J_c\left(S-\alpha_c\right)\right]J_c\left(S-\alpha_c\right)}. \tag{6.17c}$$

Therewith, the ratios of the velocities with respect to v_a result in

$$\frac{v_b}{v_a} = \sqrt{\frac{2\left(S-\alpha_2\right) - x_{1b}\left(\beta\right)\left(S-\beta\right)}{2\left(S-\alpha_2\right) + x_{1a}\left(\alpha_1\right)\left(S-\alpha_1\right)}} \tag{6.18a}$$

$$\frac{v_c}{v_a} = \sqrt{\frac{x\mu\left(S-\alpha_c\right)}{2\left(S-\alpha_2\right) + x_{1a}\left(\alpha_1\right)\left(S-\alpha_1\right)}}. \tag{6.18b}$$

6.1.3. Self-consistency equations

The self-consistency equations are unchanged, but one has to be aware that the effective exchange constants are functions of the quantum correction parameters. In contrast to (5.24), the two self-consistency equations for α_1 and β are given as

$$\frac{1}{N}\frac{\partial E^{\mathrm{MF}}}{\partial \alpha_1} = -2\alpha_1 \frac{\partial}{\partial \alpha_1}\left(J_{1a}\left(\alpha_1\right)\left(S-\alpha_1\right)\right) \tag{6.19a}$$

$$\frac{1}{N}\frac{\partial E^{\mathrm{MF}}}{\partial \alpha_1} = 2J_1\beta \frac{\partial}{\partial \alpha_1}\left(J_{1b}\left(\beta\right)\left(S-\beta\right)\right), \tag{6.19b}$$

while the equations for α_2 and α_c remain unchanged. The partial derivatives cancel out anyway and the full set of self-consistency equations reads

$$\alpha_1 = \frac{1}{2}\frac{1}{(2\pi)^3}\iiint_{\mathrm{BZ}} \mathrm{d}^3k\, \frac{\bar{A}_k - \bar{B}_k \cos k_a}{\sqrt{\bar{A}_k^2 - \bar{B}_k^2}} - \frac{1}{2} \tag{6.20a}$$

$$\alpha_c = \frac{1}{2}\frac{1}{(2\pi)^3}\iiint_{\mathrm{BZ}} \mathrm{d}^3k\, \frac{\bar{A}_k - \bar{B}_k \cos k_c}{\sqrt{\bar{A}_k^2 - \bar{B}_k^2}} - \frac{1}{2} \tag{6.20b}$$

$$\alpha_2 = \frac{1}{2}\frac{1}{(2\pi)^3}\iiint_{\mathrm{BZ}} \mathrm{d}^3k\, \frac{\bar{A}_k - \bar{B}_k \cos k_a \cos k_b}{\sqrt{\bar{A}_k^2 - \bar{B}_k^2}} - \frac{1}{2} \tag{6.20c}$$

$$\beta = -\frac{1}{2}\frac{1}{(2\pi)^3}\iiint_{\mathrm{BZ}} \mathrm{d}^3k\, \frac{\bar{A}_k \left(\cos k_b - 1\right)}{\sqrt{\bar{A}_k^2 - \bar{B}_k^2}} - \frac{1}{2}, \tag{6.20d}$$

with $\bar{A}_k, \bar{B}_k$ defined in Eq. (6.16). We underline once more, that the self-consistency equations (6.20) are very similar to the ones for the three dimensional collinear phase without biquadratic exchange (5.25). Only the parameter $x = J_1/J_2$ for the in-plane nearest neighbor exchange is to be replaced by $x_{1a}(\alpha)$ (6.14a) or $x_{1b}(\beta)$ (6.14b), respectively.

6.1.4. Staggered magnetization

Carrying out the well known replacements in (5.30), we obtain the staggered magnetization

$$m_{\mathrm{st}} = S + \frac{1}{2} - \frac{1}{2}\frac{1}{(2\pi)^3}\iiint_{\mathrm{BZ}} \mathrm{d}^3k\, \frac{\bar{A}_k}{\sqrt{\bar{A}_k^2 - \bar{B}_k^2}} \tag{6.21}$$

with biquadratic exchange.

6.2. Numerics

The adaption in the numerics is just as easy as the analytical derivation. One simply has to implement the effective exchange constants as functions of the quantum correction parameters and do all the replacements correctly. Further adjustments are not required. During numerical evaluation, the parameters μ and ν are now fixed, while x, starting at $x = 0$, is again de-/increased.

The program was also implemented within the Schwinger bosons formalism. In agreement with the results from Chapter 4, the influence of the biquadratic exchange is very much stronger than in the Dyson-Maleev representation. Based on our previous finding, we do not give any results for the Schwinger bosons because we think that the mean field approximation is insufficient in this case.

6.3. Results & Discussion for spin $S = 1$

We discuss the results for $S = 1$ and $\mu = 0.25$, which is a generic choice for the interlayer coupling. The values of ν are chosen as a result of the discussion of the spin spiral calculations in Section 2.7.2. For comparison, we also show the results without biquadratic exchange.

Starting with the staggered magnetization in Fig. 6.1, the influence of the biquadratic exchange destabilizes the collinear phase and drives the critical point towards lower values of $x = J_1/J_2$. There is only a negligible influence on the maximum value of m_{st}, which is also pushed further left.

Of great interest is the effect of the biquadratic exchange on the renormalization of the exchange parameters, shown in Fig. 6.2. While the exchange perpendicular to the spin stripes (Fig. 6.2a) is strongly renormalized and thereby strengthened by a factor > 2, the exchange parallel to the spin stripes (Fig. 6.2b) almost stays constant, except for small frustrations and in proximity to the critical point. Because the biquadratic exchange in the Hamiltonian (6.1) is restricted to in-plane next nearest neighbor sites, the only effect on the renormalization of the interlayer (Fig. 6.2c) and next nearest neighbor exchange (Fig. 6.2d) is the shift of the critical point to smaller values of x.

For our model of the three dimensional collinear phase with biquadratic exchange, the effective exchange constants are given by

$$\tilde{J}_{1a} := J_{1a}\left(\alpha_1\right)\left(S - \alpha_1\right) \tag{6.22a}$$
$$\tilde{J}_{1b} := J_{1b}\left(\beta\right)\left(S - \beta\right) \tag{6.22b}$$
$$\tilde{J}_{c} := J_{c}\left(S - \alpha_c\right) \tag{6.22c}$$
$$\tilde{J}_{2} := J_{2}\left(S - \alpha_2\right). \tag{6.22d}$$

In Fig. 6.3, the effective exchange in a- and b-direction is plotted in units of the exchange constant J_2. The exchange perpendicular to the spin stripes (Fig. 6.3a) is strengthened because of the biquadratic term. Parallel to the spin stripes (Fig. 6.3b), the effective exchange lies only slightly above the identity x. Consequently, the influence of an in-plane biquadratic exchange stresses the anisotropy as desired.

The ratios of the spin wave velocities (Fig. 6.4) are weakened, since the strengthening of the exchange perpendicular to the stripes leads to a greater spin wave velocity v_a. In general, the qualitative behavior of the ratios is very similar to the one observed without biquadratic exchange (Fig. 5.4 and 5.7).

All in all, a biquadratic exchange acting on in-plane nearest neighbor sites strengthens the anisotropy of the exchange parallel and perpendicular to the spin stripes. The growing anisotropy with increasing biquadratic exchange $\nu = J_{\mathrm{bq}}/J_1$ is caused by the very strong renormalization of the exchange perpendicular to the spin stripes. The exchange parallel to the spin stripes experiences a marginal strengthening and is only weakened in proximity to the critical point. Hence, the biquadratic exchange never induces an effective ferromagnetic exchange $\tilde{J}_{1b} < 0$ in b-direction.

In addition, we note that at the critical point the spin wave velocities (Fig. 6.4) as well as the staggered magnetization (Fig. 6.1) always obtain finite values. A detailed study of the numerics shows that the

all curves in Fig. 6.4a stop at the last value of x where $(v_b/v_a)^2 > 0$. For the next regular value of x, the parameter $(v_b/v_a)^2$ is already negative which results in $\omega_k^2 < 0$ and the numerical calculation is aborted. The very steep descend of the ratio v_b/v_a lies beyond the resolution of our numerics. Thus, calculations with a very small increment for the coupling x did not bring much improvement to drive the curves closer to zero. All together, we suggest the all curves are located in the velocity-driven scenario, where the collinear phase ceases to exist because of the vanishing spin wave velocity v_b. The magnetization always obtains finite positive values. The occurrence of the velocity-driven scenario is also stressed by the value of the interlayer coupling $\mu = 0.25$ which corresponds to the velocity-driven scenario, see Section 5.4 for details.

In the next chapter, our model is fitted to experimentally measured spin wave dispersions. Thus, we display the spin wave dispersions in units of J_2 in Fig. 6.5. Along the high-symmetric a- and c-direction (Fig. 6.5a), the maximum values of the dispersion grow with increasing biquadratic exchange, while the line shape is unchanged. In contrast, the local minimum at $k = (0, 1, 0)$ along the b-direction (Fig. 6.5b) rises. The minimum would vanish for an effective ferromagnetic exchange which can bee seen in the dispersion (6.11). For $\tilde{J}_{1b} < 0$, the component A_k (6.13a) of ω_k has its maximum at $k = (0, 1, 0)$. An effective ferromagnetic exchange parallel to the spin stripes would imply unfrustrated magnetism.

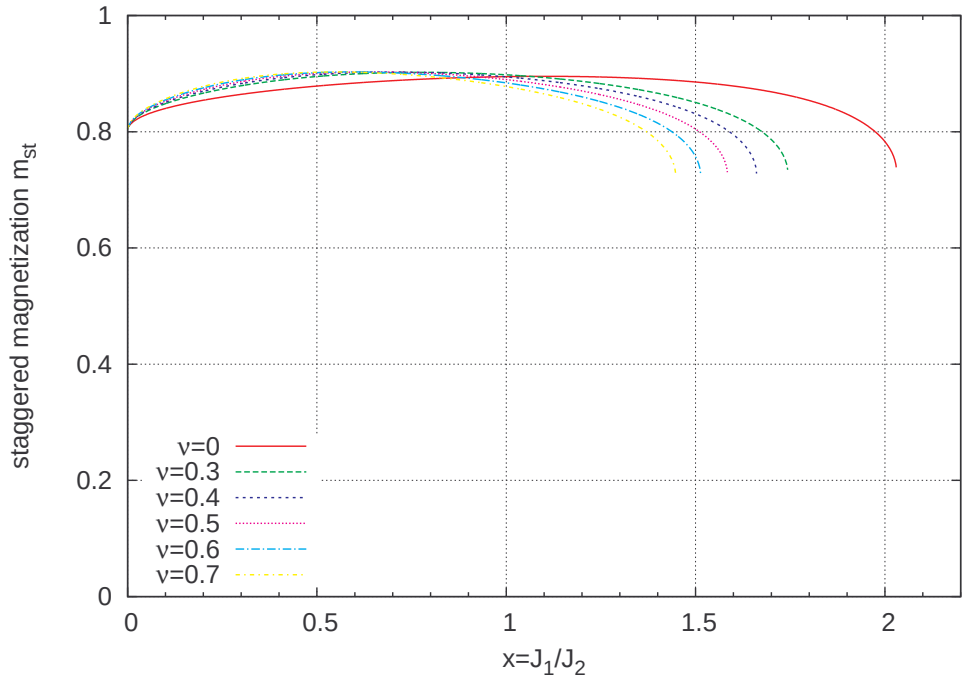

Fig. 6.1.: Staggered magnetization as a function of x for $S = 1$ and $\mu = 0.25$. All curves are in the velocity-driven scenario and the magnetization always obtains finite positive values.

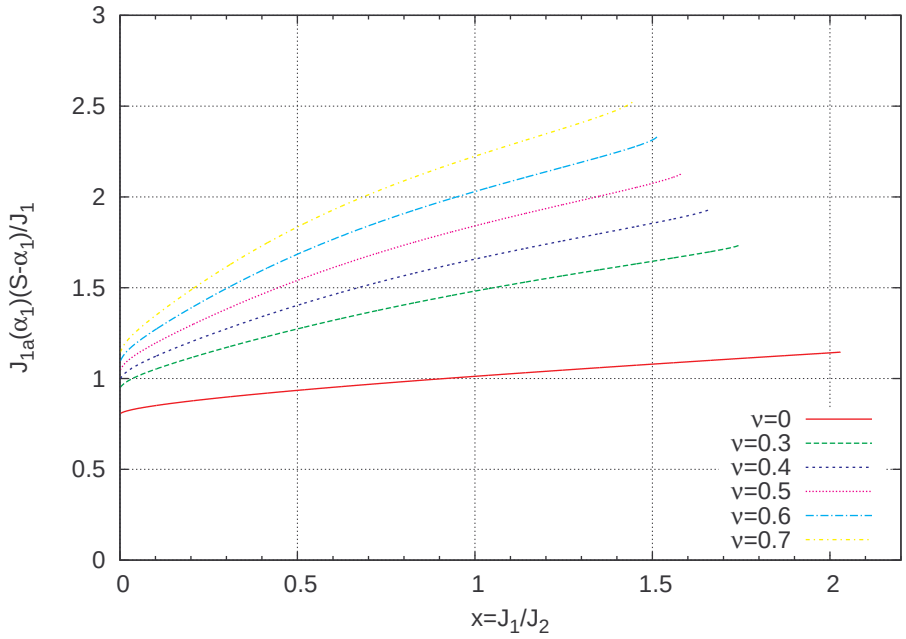

(a) Renormalization of the exchange perpendicular to the spin stripes.

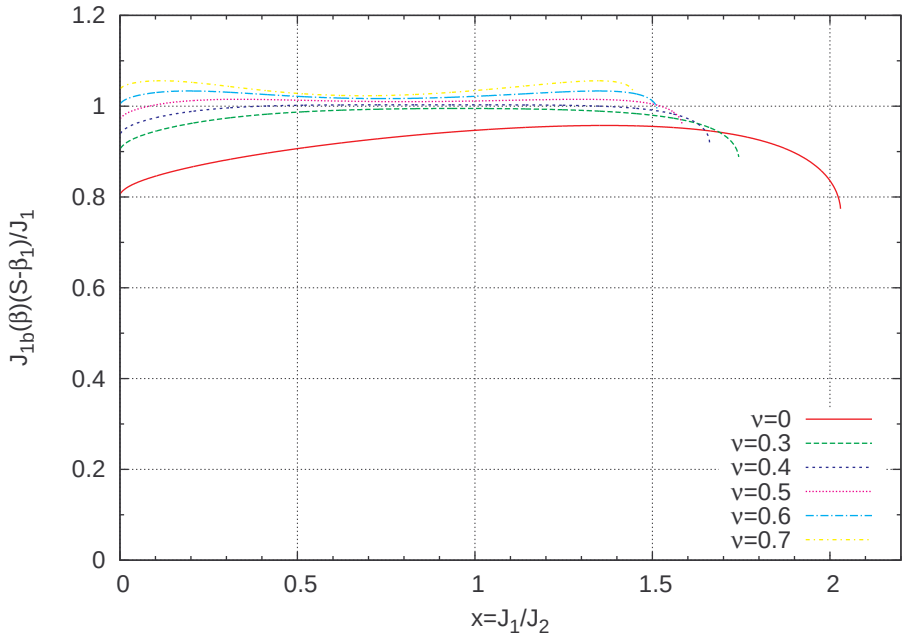

(b) Renormalization of the exchange parallel to the spin stripes.

Fig. 6.2.: Renormalization due to quantum fluctuations as a function of x for $S = 1$ and $\mu = 0.25$. All curves are in the velocity-driven scenario.

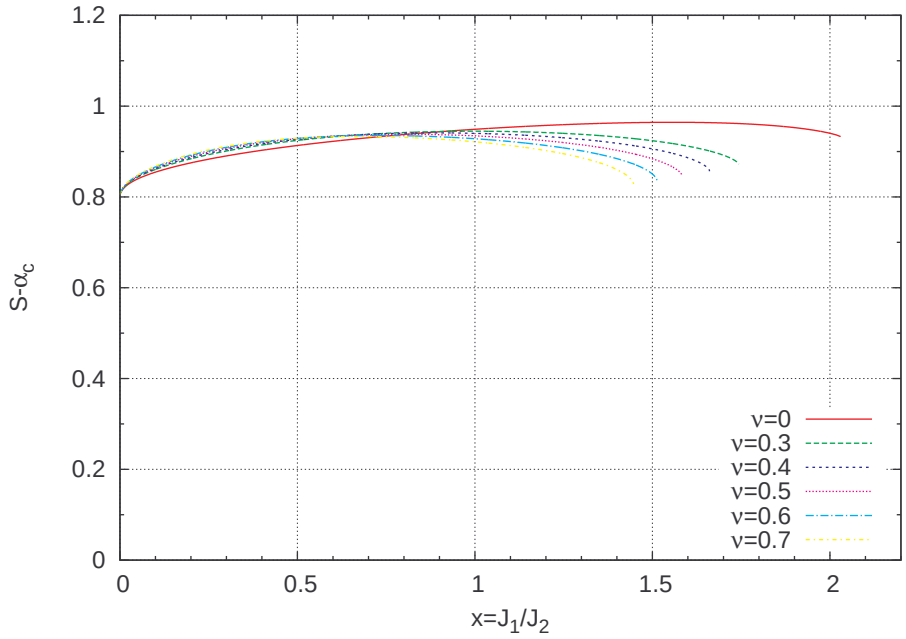

(c) Renormalization of the interlayer exchange.

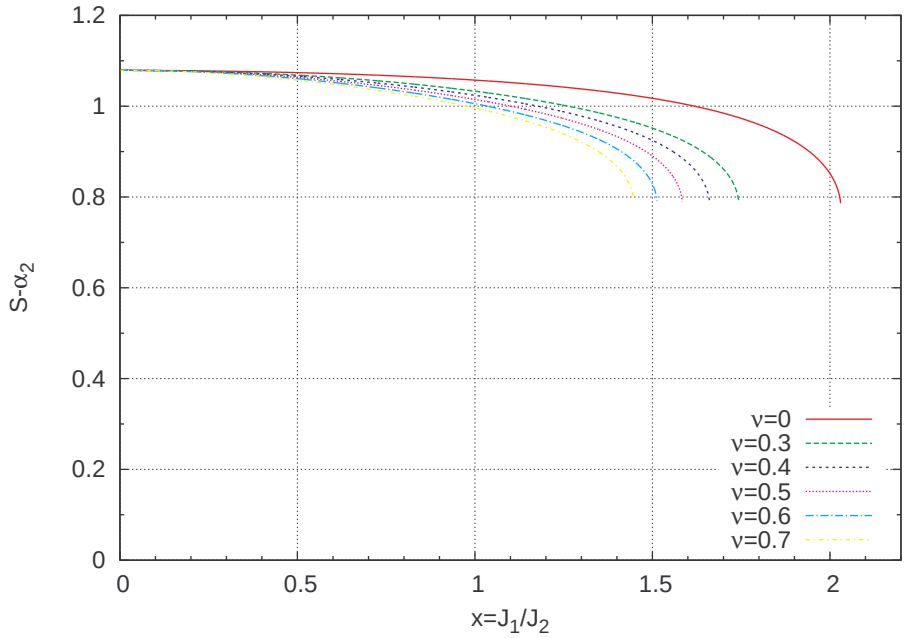

(d) Renormalization of the next nearest neighbor exchange.

Fig. 6.2.: Renormalization due to quantum fluctuations as a function of x for $S = 1$ and $\mu = 0.25$. All curves are in the velocity-driven scenario.

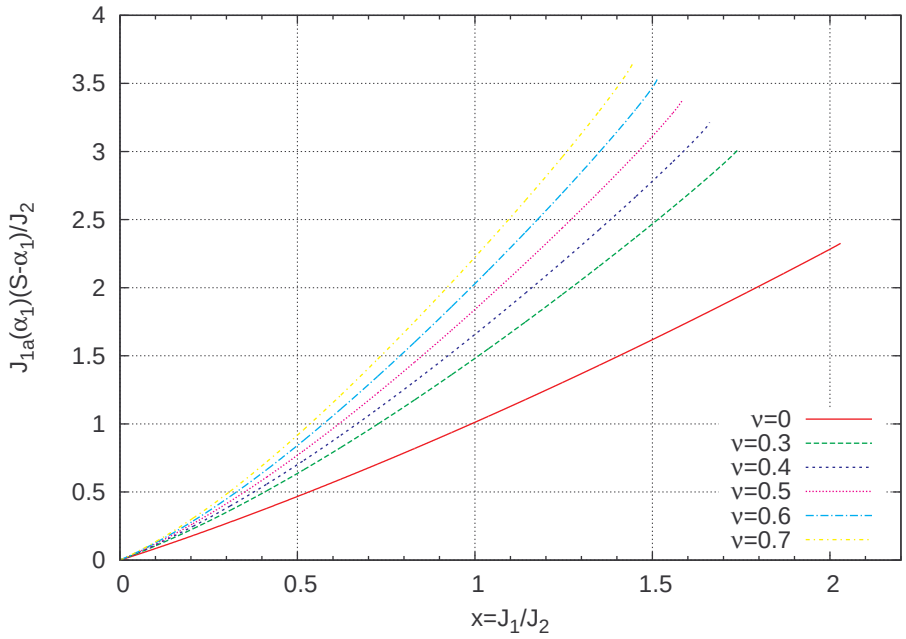

(a) Perpendicular to the spin stripes.

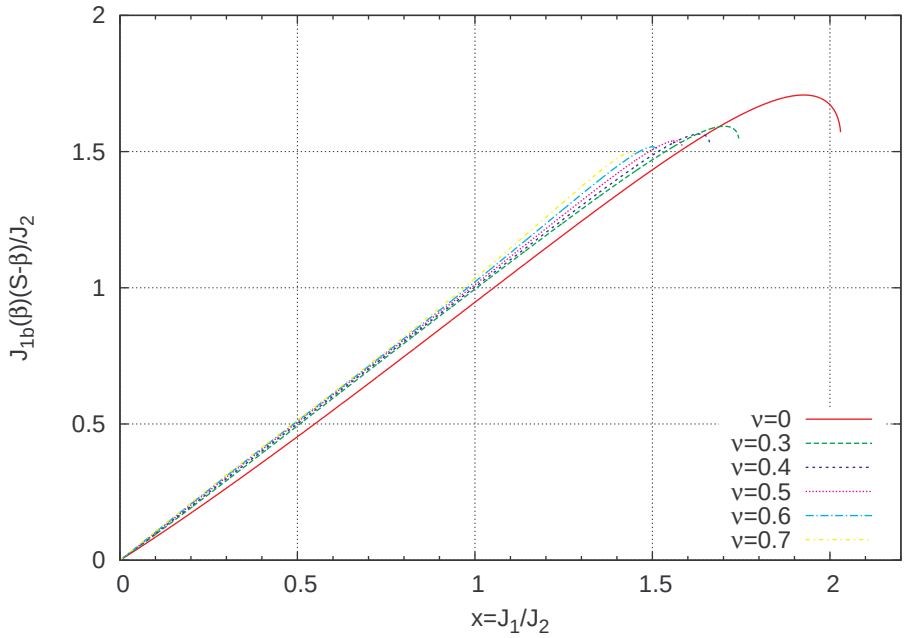

(b) Parallel to the spin stripes.

Fig. 6.3.: Effective in-plane exchange constants in units of J_2 as a function of x for $S = 1$ and $\mu = 0.25$. All curves are in the velocity-driven scenario.

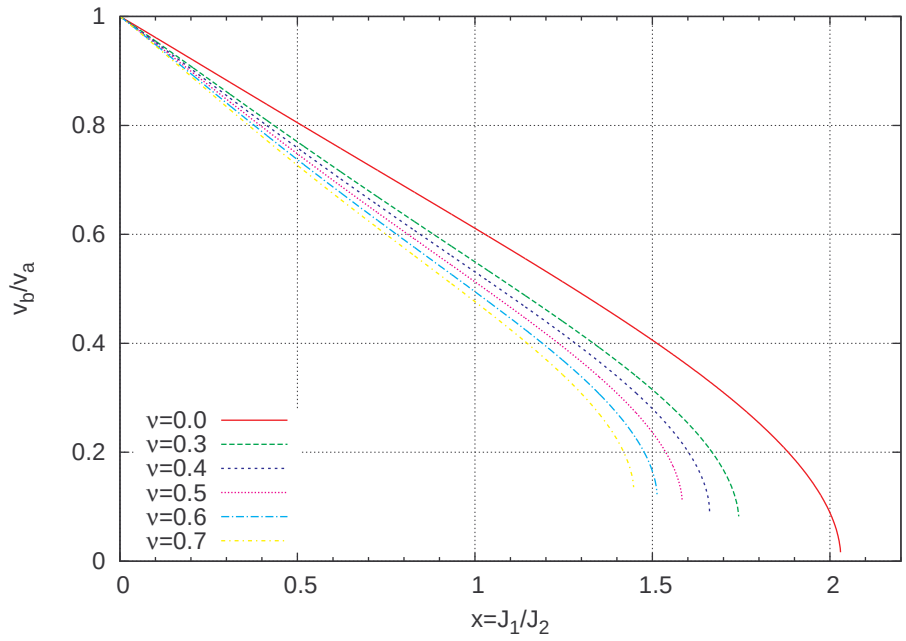

(a) v_b/v_a

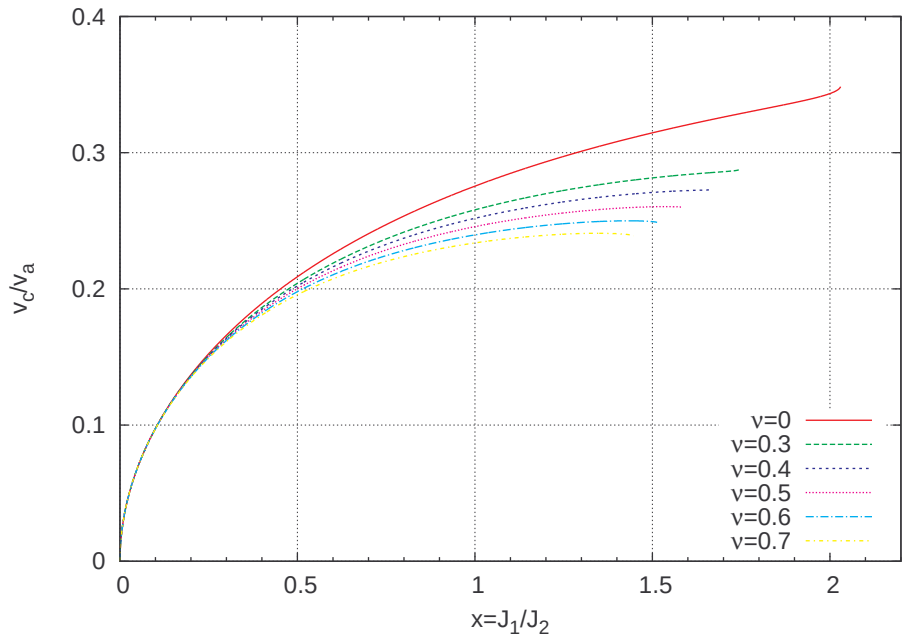

(b) v_c/v_a

Fig. 6.4.: Ratios of the spin wave velocities as a function of x for $S = 1$ and $\mu = 0.25$. All curves are in the velocity-driven scenario. The ratio v_b/v_a vanishes, which lies beyond the resolution of our numerics.

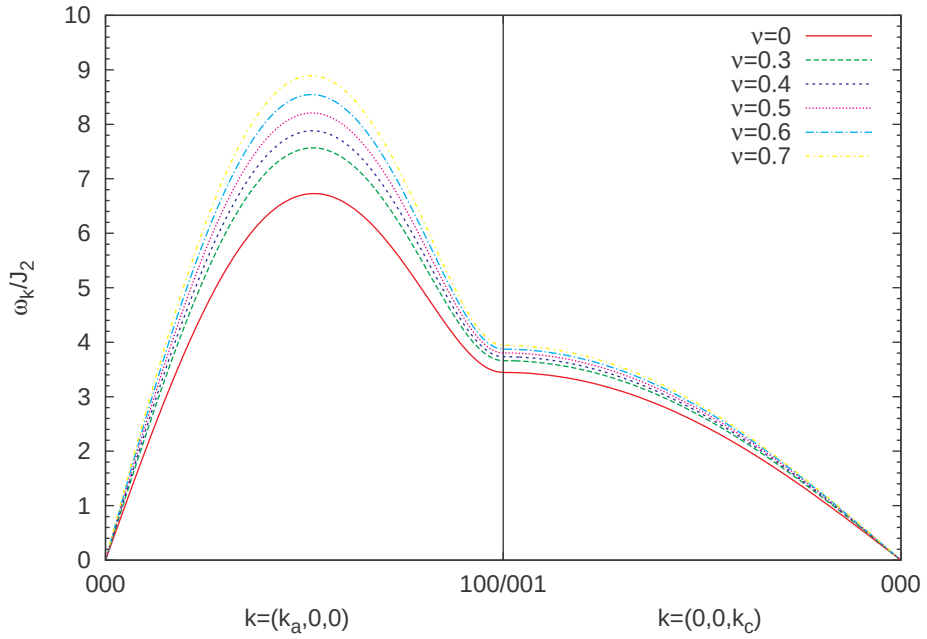

(a) Perpendicular to the spin stripes and between the layers.

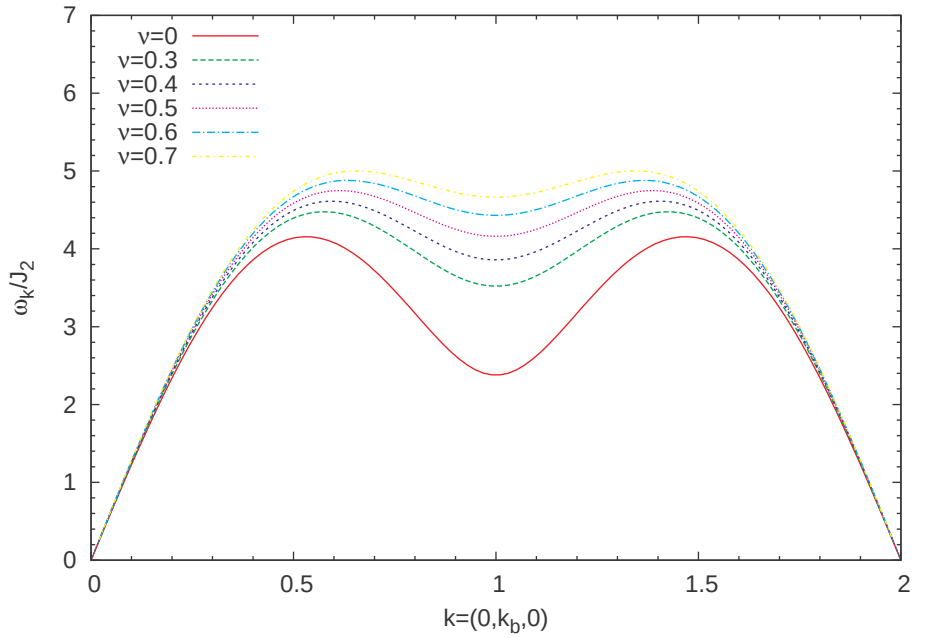

(b) Parallel to the spin stripes.

Fig. 6.5.: Dispersion in units of J_2 along high-symmetry directions in the Brillouin zone for $S = 1$, $x = 1$ and $\mu = 0.25$.

7. Iron pnictides

This chapter deals with the application of our previously discussed models to iron pnictides. The iron pnictides have been introduced in Section 2.1. In Section 2.2, the extended and frustrated Heisenberg model has been motivated to study the magnetic excitations in these iron-based compounds. We choose $S = 1$ as an appropriate value for the spin [11]. This choice is based on successful studies of two-band models [85]. Furthermore, iron has an even number of electrons in its outer shell, which results in an integer spin. The values $S = 0$ and $S = 1$ are also possible, but the resulting local moment would be too weak or too strong compared to the measured local moment.

We now discuss different experimental results for the 122 compounds and fit our model with and without biquadratic exchange to spin wave velocities measured by inelastic neutron scattering. Most of the experimental studies concentrate on the 122 pnictides because high-quality samples are available for this family of the iron pnictide.

Alternatively, it is also possible to determine the value of $x = J_1/J_2$ by reproducing the local magnetic moment. But this is very ambiguous, since the local moment can depend on a variety of effects, such as itineracy and hybridization, while the spin wave velocities only depend on the Hamiltonian.

The determined frustration x reveals, whether the strong reduction of the local magnetic moment can be explained by quantum fluctuations, as it was the case for the two dimensional collinear phase [11].

As already mentioned, the best method for studying magnons is inelastic neutron scattering. Hence, we also discuss the dynamical structure factor for one scenario, which is then compared to measured neutron scattering intensities.

7.1. Results for the 3D collinear phase

At first, we discuss the three dimensional collinear phase without biquadratic exchange. This extends the study of the two dimensional collinear phase by Uhrig *et al*. [11] to a higher dimension. Our model (Chapter 5) is based on self-consistent spin wave theory, which is an improvement compared to the work by Yao and Carlson [53, 54]. Their studies are based on linear spin wave theory. In addition, we do not introduce an ab-initio anisotropic exchange within the collinear ordered layers. In our studies, the anisotropy is induced by quantum fluctuations.

7.1.1. $SrFe_2As_2$ & $BaFe_2As_2$

Early neutron scattering studies for $SrFe_2As_2$ [8] and $BaFe_2As_2$ [37] were not able to extract the spin wave dispersion along all crystal axis. No measurement for the spin wave velocity v_b was available. For the velocities perpendicular to the stripes and between the layers, the values

$$v_a \approx 205 \text{ meV}$$
$$v_c \approx 45 \text{ meV}$$

were determined. Due to the lack of experimental data, Ong *et al*. [86] suggested

$$v_b \approx 10 - 30 \text{ meV}.$$

The determined range is based on an analysis of experimental data on the temperature dependence of the staggered magnetization, which is based on a non-linear σ-model. Thus, the ratios of the spin wave velocities

$$\frac{v_b}{v_a} = 0.049\text{-}0.146$$
$$\frac{v_c}{v_a} = 0.220$$

were obtained, where two decimal places should be accurate.

Now, we fit our model of the three dimensional collinear phase (Chapter 5) to the spin wave velocities presented above. The fitting is done numerically via a two dimensional root finding, based on Broyden's multidimensional secant method. The coupling ratios x and μ of our model are determined by the ratios v_b/v_a and v_c/v_a of the spin wave velocities. In addition, a second Broyden routine which determines the quantum correction parameters, is called within the first one. Both routines need initial guesses for all parameters, which are taken from the corresponding plots in Section 5.3.2. For our analysis, we restrict ourselves to $v_b = 20$ meV, which leads to $v_b/v_a = 0.098$. Therewith, we numerically determined the ratios

$$x = 1.974$$
$$\mu = 0.114.$$

The first two decimal places should be accurate. In addition, we give the third decimal place.

Consequently, the iron pnictides are close to a quantum phase transition for the range of v_b determined by Ong *et al*. and the reduction of the static local magnetic moment can be explained by quantum fluctuations. The determined value of x agrees with previous results from the two dimensional collinear phase by Uhrig *et al*. [11].

	v_a	v_b	v_c	v_b/v_a	v_c/v_a
Zhao *et al.*	181	127	44	0.704	0.246
Diallo *et al.*	187	135	42	0.722	0.222
Ong *et al.*	205	10-30	45	0.049-0.146	0.220

Tab. 7.1.: Extracted spin wave velocities (in meV) from neutron scattering studies by Zhao *et al.* [10] and Diallo *et al.* [9]. For completeness, we also display the velocities for $Ba/SrFe_2As_2$ proposed by Ong *et al.* [86]. Diallo's velocities are very accurate because they fitted only three parameters to the measured dispersion. Zhao *et al.* fitted all four exchange parameters J_{1a}, J_{1b}, J_2 and J_c and received greater standard deviations. Thus, the standard deviation is much higher for Zhao's velocities. For the ratios, two decimal places should be exact. The the third decimal place is given in addition.

7.1.2. $CaFe_2As_2$

The latest neutron scattering studies in iron pnictides concentrate on the 122 pnictide $CaFe_2As_2$. We discuss the data obtained by Zhao *et al.* [10] and Diallo *et al.* [9]. The experimentalists fit a dispersion obtained within linear spin wave theory (see Section. 3.1.1) to the experimental data. In order to obtain proper results, they have to assume anisotropic exchange constants J_{1a} and J_{1b} for the in-plane nearest neighbor exchange. To extract the spin wave velocities, we expand the fitted dispersion for small momenta. The velocities can easily be calculated by inserting the fitted exchange constants, which are given in the papers. We neglect the single ion anisotropy, which leads to a small gap in the order of 5 meV in the measured dispersions. The extracted spin wave velocities for Zhao's and Diallo's data are listed in Tab. 7.1.

Both experimental results are in very good agreement. In sharp contrast to the value of v_b suggested by Ong *et al.*, both measured values are of a much higher magnitude. Thus, this leads to an entirely different scenario than the one by Ong *et al.*.

The parameters x and μ of our model in three dimensional collinear phase are again determined numerically, as described in the previous section. The determined coupling ratios of our model are listed in Tab. 7.2. Accordingly, both results are located deep in the frustrated phase. This agrees with previous results (Fig. 5.7 and 6.4), which indicate that a system with a high ratio v_b/v_a cannot reside close to a quantum phase transition. As expected, the interlayer coupling is much smaller than the nearest neighbor coupling. It is stronger for Zhao's data than for Diallo's data, since they measured a higher value for v_c.

7.1.3. Discussion

The results of the two previous sections yield an inconsistent picture. When we adjust our model to the spin wave velocities proposed by Ong *et al.*, we reproduce the result from the two dimensional collinear phase [11] that the iron pnictides are in the vicinity of a quantum phase transition. In contrast, we obtain $x \approx 0.7$-0.8 for the complete sets of experimentally measured spin wave velocities

	$x = J_1/J_2$	$\mu = J_c/J_1$
Zhao *et al.*	0.760	0.245
Diallo *et al.*	0.716	0.211
Ong *et al.*	1.974	0.114

Tab. 7.2.: Obtained parameters for our model of the three dimensional collinear phase (Chapter 5). To determine the parameters, our model was fitted to experimental ratios of the spin wave velocities measured by Zhao *et al.* [10] and Diallo *et al.* [9]. For completeness, we also display the results for the scenario proposed by Ong *et al.* [86]. The first two decimal places of the parameters should be exact.

	J_1	J_c	J_2	$\tilde{J}_{1a}$	$\tilde{J}_{1b}$	$\tilde{J}_c$	$\tilde{J}_2$	J_{1a}^{LSW}	J_{1b}^{LSW}	J_c^{LSW}	J_2^{LSW}
Ong *et al.*	50.8	5.8	25.7	59.0	40.2	4.8	20.6	-	-	-	-
Zhao *et al.*	23.2	5.7	30.5	22.6	21.6	5.3	32.5	49.9	-5.7	5.3	18.9
Diallo *et al.*	23.1	4.9	32.3	22.4	21.4	4.5	34.6	-	-	-	-

Tab. 7.3.: Exchange constants and effective exchange constants (7.1) in meV for our model of the three dimensional collinear phase. The values are determined so that the spin wave velocities in Tab. 7.1 are reproduced. In addition, the exchange constants J_i^{LSW} obtained in linear spin wave theory by Zhao *et al.* [10] are given. These exchange constants are not available for Ong's and Diallo's data. Diallo fitted three parameters which are linear combinations of the four exchange constants appearing in the Hamiltonian.

for $CaFe_2As_2$. Hence, the experimental data from Zhao *et al.* and Diallo *et al.* leads to the conclusion that the iron pnictides reside deeply in the frustrated phase.

In order to decide which set of spin wave velocities is to be preferred for further investigations, we now discuss the whole spin wave dispersion.

Therefore, we have to determine the value of the next nearest neighbor coupling J_2 in the dispersion (5.14). This is simply done by adapting the proposed values of the spin wave velocity v_b (see Tab. 7.1). After that, the values of the couplings J_1 and J_c can be calculated with the values of $x = J_1/J_2$ and $\mu = J_c/J_1$ (see Tab. 7.2). In addition, we calculate the effective exchange constants, given as

$$\tilde{J}_{1a} := J_1 (S - \alpha_1) \tag{7.1a}$$
$$\tilde{J}_{1b} := J_1 (S - \beta) \tag{7.1b}$$
$$\tilde{J}_c := J_c (S - \alpha_c) \tag{7.1c}$$
$$\tilde{J}_2 := J_2 (S - \alpha_2) . \tag{7.1d}$$

The results can be found in Tab. 7.3.

In Fig. 7.1, the dispersion of the three dimensional collinear phase (5.14) is plotted for the parameters in Tab. 7.3 along a highly symmetric path through the Brillouin zone. In addition, the dispersion is compared with inelastic neutron scattering data from Zhao *et al.* [10].

The results along k_a and k_c (Fig. 7.1a) agree very well for all results. No big difference in the qualitative behavior can be seen. The maximum values for Ong *et al*. are a bit higher because the measurements for $Sr/BaFe_2As_2$ yield higher spin wave velocities along the *a*-direction. The parameters obtained by the fits of our model to Zhao's and Diallo's data reproduce the corresponding inelastic neutron scattering data for $CaFe_2As_2$ very well.

In contrast, discrepancies along the *b*-direction (Fig. 7.1b) are observed. Due to the very small spin wave velocity v_b, Ong's scenario differs enormously from the other results. A deviation similar to the other high-symmetric directions would rather be acceptable. However, there is also the possibility that a magnetic mode located at very low energies along k_b has been missed by the experimentalists. The neutron scattering studies for the iron pnictides concentrate rather on higher energies. In Fig. 7.1b, the data point with the lowest energy for $CaFe_2As_2$ is already located above the mode with $v_b \approx 20$ meV.

For the parameters determined from Zhao's and Diallo's data, our dispersion reproduces the inelastic neutron scattering data very well for small momenta, but it fails for high spin wave energies and momenta. This is caused by the lack of anisotropy in our results (see Tab. 7.3). For $\tilde{J}_{1b} < 0$, the k_b-dependent term in the spin wave dispersion (5.14) changes its sign which converts the minimum at $k = (0, 1, 0)$ into a maximum. Thus, an effective ferromagnetic exchange $\tilde{J}_{1b} < 0$ parallel to the spin stripes is necessary to describe the maximum at $k = (0, 1, 0)$. The appropriate value for Zhao's data is $\tilde{J}_{1b} \approx -5.7$ meV [10].

We stress that Zhao's paper [10] is the only source of neutron scattering data at very high energies available to our knowledge. Due to heavy damping, Diallo *et al*. [9] only provide data up to 125 meV, where our model is still in very good agreement with the experimental data. Consequently, they are not able to identify the dispersion close to $k = (0, 1, 0)$ and their best fit agrees with our current result. However, they also discuss a scenario where the energy at $k = (0, 1, 0)$ is raised, but always lower than at $k = (0, 0.5, 0)$. Thus, further inelastic neutron scattering studies at very high energies would be welcomed to prove the results by Zhao *et al*.. The scattering intensities at high energies are very low and modes might have been missed.

Han *et al*. [34] used first-principles density functional theory calculations to determine the magnetic interactions in the iron pnictides. They proposed a universal trend of $\tilde{J}_{1a} \approx 2\tilde{J}_2$, in particular $\tilde{J}_{1a}/2\tilde{J}_2 = 0.95$ for $CaFe_2As_2$, 1.31 for $SrFe_2As_2$ and 1.51 for $BaFe_2As_2$. Our results for $Ba/SrFe_2As_2$, where $\tilde{J}_{1a}/2\tilde{J}_2 = 0.91$, still show a similar trend, while there is a huge deviation in our results for $CaFe_2As_2$ with $\tilde{J}_{1a}/2\tilde{J}_2 = 0.32 - 0.35$ due to the strong next nearest neighbor exchange. Furthermore, Han *et al*. also obtained a slightly ferromagnetic exchange parallel to the spin stripes for $CaFe_2As_2$, which fits to the results by Zhao *et al*..

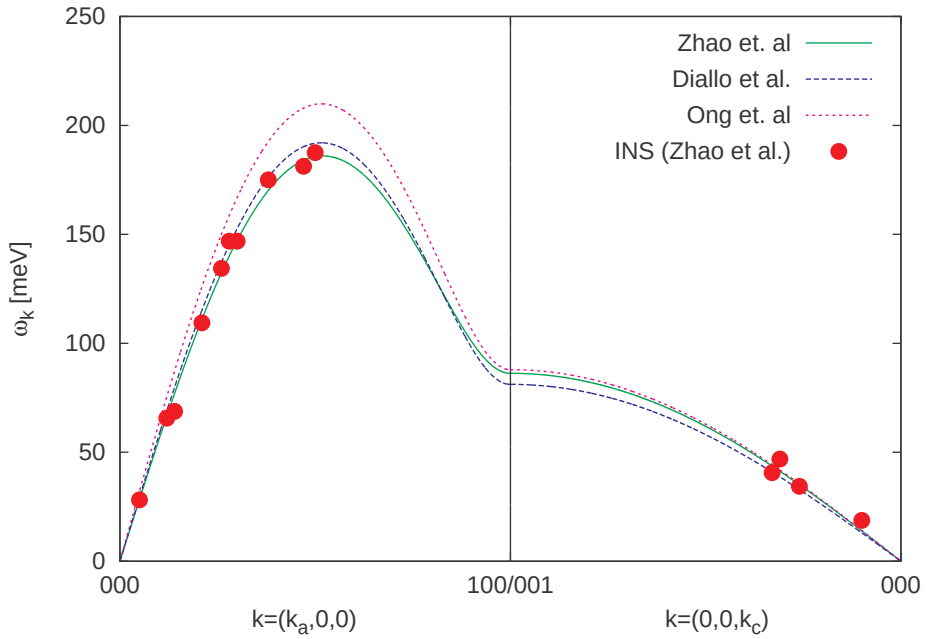

(a) Perpendicular to the spin stripes and between the layers.

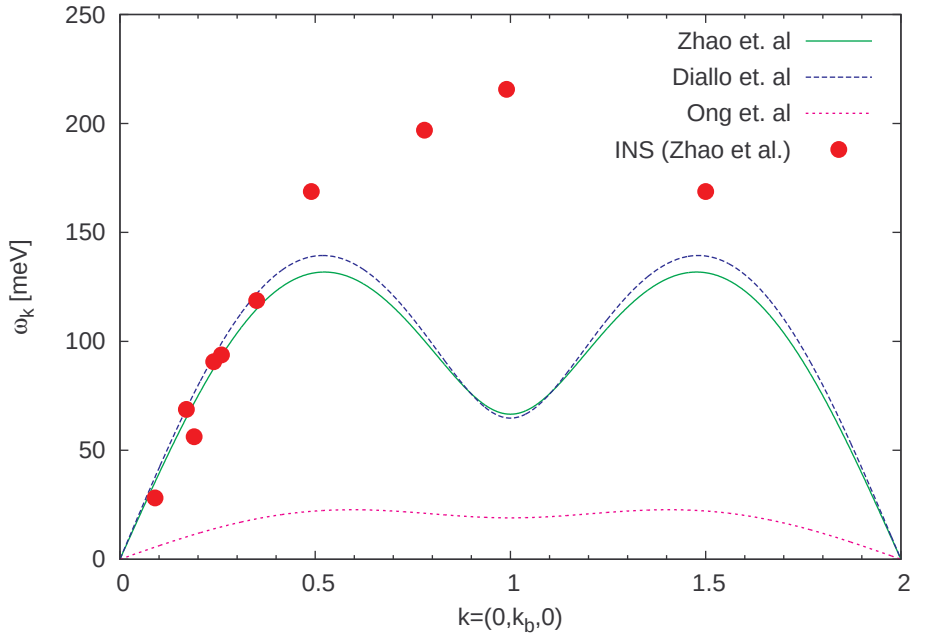

(b) Parallel to the spin stripes.

Fig. 7.1.: Spin wave dispersion (5.14) of our model of the three dimensional collinear phase. The dispersion (lines) is plotted for the corresponding sets of parameters given in Tab. 7.3. The red dots are experimental data points extracted from inelastic neutron scattering for $CaFe_2As_2$ [10].

7.2. Results with biquadratic exchange for $CaFe_2As_2$

The results with biquadratic exchange for Diallo's and Zhao's data are given in Tab. 7.4. A couple of reasonable values for $\nu = J_{\mathrm{bq}}/J_1$, based on the spin spiral calculations by Yaresko *et al*. [22], have been chosen. Yaresko's results are presented in Section 2.7.2 in detail. Otherwise, a third independent information from experiment would be necessary to determine the additional parameter ν. This would probably be the energy at $k = (0,1,0)$ taken from Zhao's data, but the influence of the biquadratic exchange is not strong enough to reproduce the dispersion at this momentum. The parameters $x = J_1/J_2$ and $\mu = J_c/J_1$ of our model of the three dimensional collinear phase with biquadratic exchange (Chapter 6) are determined as before. In addition, a set of parameters has been calculated for a rather unlikely strength of the biquadratic exchange with $\nu = 3.0$.

As a consequence of our analysis in the last section, we now concentrate on Zhao's and Diallo's measured spin wave velocities for $CaFe_2As_2$ (see Tab. 7.1). The spin wave velocities proposed by Ong *et al*. are not discussed any further.

The influence of the biquadratic exchange strengthens the anisotropy between the exchange parallel and perpendicular to the spin stripes. As before, the results for both data sets are very similar. In addition, there is no impact on the interlayer coupling and the dispersion along the *a*- and *b*-direction, which is plotted in Fig. 7.2a and 7.2c. The agreement between the neutron scattering data and our model is again very nice. As before, the interlayer coupling for Zhao's data is higher.

The improvement of the dispersion along k_b, plotted in Fig. 7.2b and 7.2d, is not very significant. It still matches the scattering data only for small momenta, while the energy at $k = (0,1,0)$ is lifted

ν	0.3	0.4	0.5	0.6	3.0
x	0.645	0.616	0.589	0.565	0.284
μ	0.297	0.314	0.332	0.349	0.793
J_1	18.9	17.9	16.9	16.0	7.1
J_c	5.6	5.6	5.6	5.6	5.6
J_2	29.4	29.0	28.7	28.4	24.9
J_{bq}	5.7	7.1	8.5	9.6	21.2
$\tilde{J}_{1a}$	25.4	26.3	27.1	27.9	36.2
$\tilde{J}_{1b}$	18.8	17.9	17.0	16.3	8.0
$\tilde{J}_c$	5.3	5.3	5.3	5.3	5.3
$\tilde{J}_2$	31.1	30.7	30.3	29.9	25.8

(a) Parameters of our model obtained for Zhao's spin wave velocities.

ν	0.3	0.4	0.5	0.6	3.0
x	0.606	0.578	0.553	0.530	0.265
μ	0.255	0.269	0.284	0.299	0.676
J_1	18.9	17.9	16.9	16.0	7.1
J_c	4.8	4.8	4.8	4.8	4.8
J_2	31.3	30.9	30.6	30.3	26.8
J_{bq}	5.7	7.1	8.5	9.6	21.3
$\tilde{J}_{1a}$	25.0	25.9	26.7	27.4	35.7
$\tilde{J}_{1b}$	18.8	17.9	17.1	16.4	8.1
$\tilde{J}_c$	4.5	4.5	4.5	4.5	4.5
$\tilde{J}_2$	33.2	32.8	32.4	32.0	27.9

(b) Parameters of our model obtained for Diallo's spin wave velocities.

Tab. 7.4.: Parameters of our model of the three dimensional collinear phase with fixed values of the biquadratic exchange $\nu = J_{\mathrm{bq}}/J_1$. The parameters were determined by fitting our model to experimental spin wave velocities in $CaFe_2As_2$ measured by Zhao et al. [10] and Diallo *et al.* [9]. For the ratios of the couplings, two decimal places should be accurate.

up to approximately 20%. Hence, we have arrived at a scenario, which is located between the one without biquadratic exchange and Zhao's scattering data. As mentioned before, a similar scenario without biquadratic exchange has shortly been suggested by Diallo *et al.*.

In addition, we calculated the parameters with a very strong and unlikely biquadratic exchange with $\nu = 3.0$. While the dispersion perpendicular to the spin stripes and between the layers is again unaffected (Fig. 7.2a and 7.2c), the minimum along k_b (Fig. 7.2b and 7.2d) has almost vanished. It seems that a plateau is emerging around $k = (0, 1, 0)$, but the dispersion is still far away from the measured maximum at $k = (0, 1, 0)$.

In general, the ratio $x = J_1/J_2$ decreases with increasing ν. The reason for this behavior is simple: The biquadratic exchange leads to an increasing spin wave velocity v_a. To keep the ratio v_b/v_a constant, the coupling ratio $x = J_1/J_2$ has to be decreased. Analogously, the interlayer coupling $\mu = J_c/J_1$ has to increase to keep the ratio v_c/v_a constant. The calculated values of x indicate that the system resides on the plateau of the staggered magnetization. Thus, other effects are likely to be responsible for the small static local moment measured in experiment.

Compared to the decreasing effective next nearest neighbor exchange $\tilde{J}_2$, the effective exchange perpendicular to the stripes $\tilde{J}_{1a}$ is increasing. Thus, the ratio $\tilde{J}_{1a}/2\tilde{J}_2$ increases up to 0.47, but we cannot confirm the trend of $\tilde{J}_{1a}/2\tilde{J}_2 \sim 1$ proposed by Han *et al.*.

All in all, the additional biquadratic exchange is able to influence the dispersion parallel to the spin stripes and to strengthen the anisotropy of the effective in-plane nearest neighbor exchange constants. However, it is not possible to reproduce the whole experimental dispersion measured by Zhao *et al.*. Nice agreement is found for not too large energies and momenta. An extension of the biquadratic exchange to next nearest neighbor sites could bring further improvement.

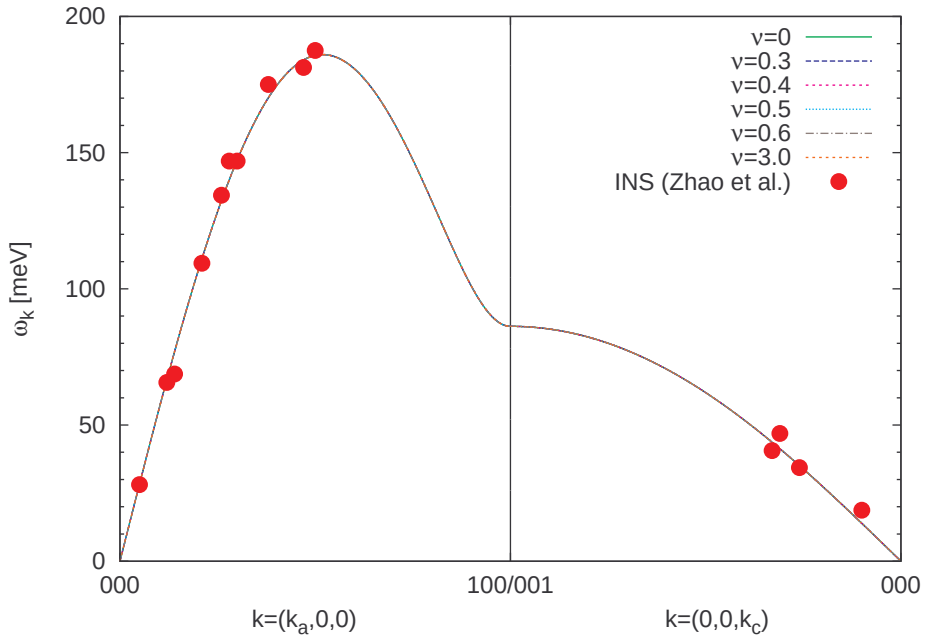

(a) Perpendicular to the spin stripes and between the layers.

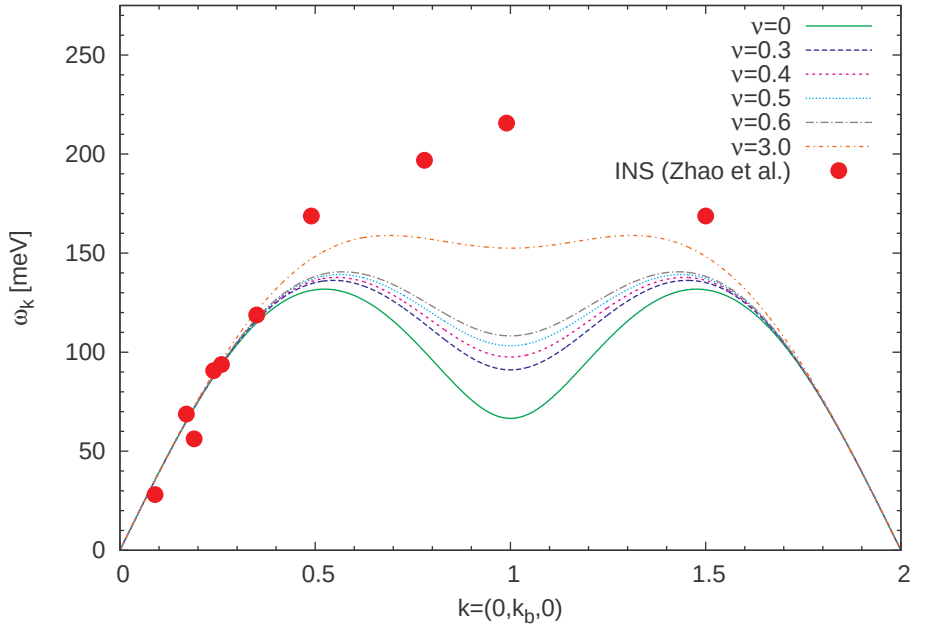

(b) Parallel to the spin stripes.

Fig. 7.2.: Spin wave dispersion (6.11) of our model of the three dimensional collinear phase with biquadratic exchange for various values of $\nu = J_{bq}/J_1$. The dispersion (lines) is plotted for the corresponding sets of parameters given in Tab. 7.4a, which were obtained by adjusting our model to Zhao's spin wave velocities. The red dots are experimental data points extracted from inelastic neutron scattering for $CaFe_2As_2$ [10].

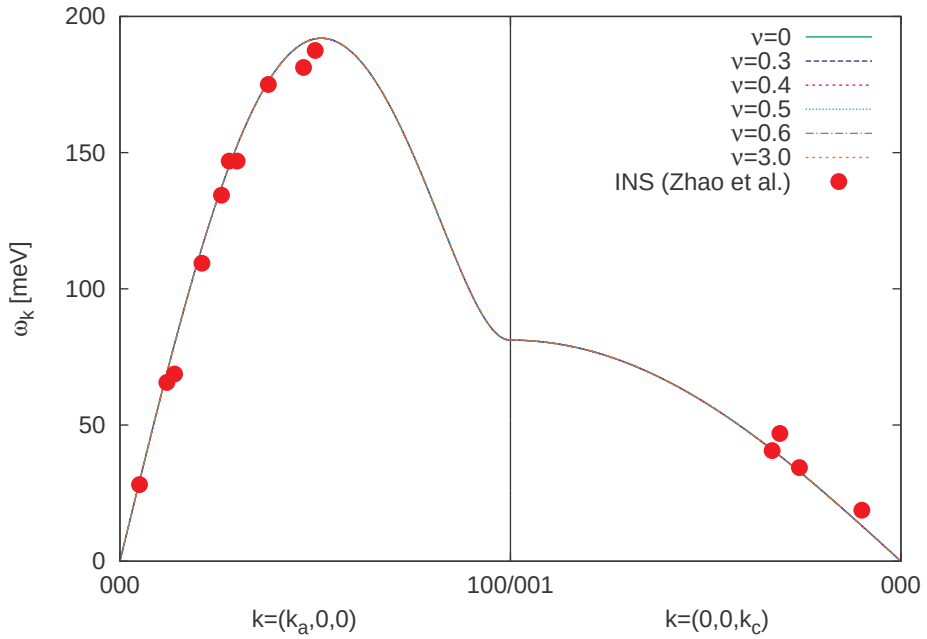

(c) Perpendicular to the spin stripes and between the layers.

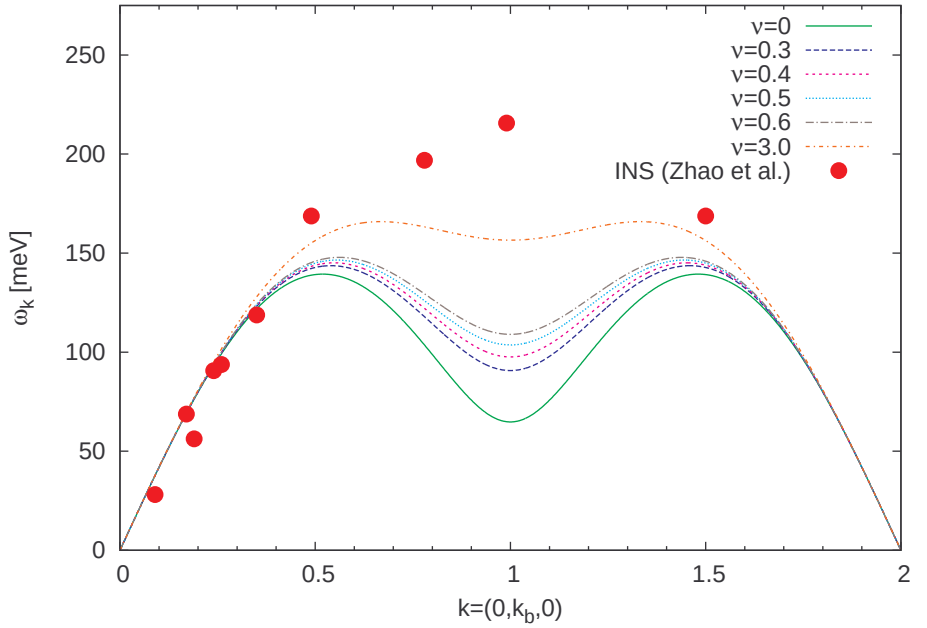

(d) Parallel to the spin stripes.

Fig. 7.2.: Spin wave dispersion (6.11) of our model of the three dimensional collinear phase with biquadratic exchange for various values of $\nu = J_{bq}/J_1$. The dispersion (lines) is plotted for the sets of parameters given in Tab. 7.4b, which were obtained by adjusting our model to Diallo's spin wave velocities. The red dots are experimental data points extracted from inelastic neutron scattering for $CaFe_2As_2$ [10].

7.3. Scattering intensities

The question arises whether and how the dispersion of our model of the three dimensional collinear phase with biquadratic exchange and the dispersion fitted by Zhao *et al*. [10], where the exchange parallel to the spin stripes is ferromagnetic, can be experimentally distinguished. Looking for further information we compare the scattering intensities.

The scattering intensities are proportional to the dynamical structure factor derived in Section 3.2.2. We still have to determine the θ_k-dependent prefactor in (3.29). Recalling the diagonalization condition $\tanh 2\theta_k = -A_k/B_k$, it can easily be verified that

$$\begin{aligned}\left(\cosh\theta_k + \sinh\theta_k\right)^2 &= \cosh^2\theta_k + \sinh^2\theta_k + 2\cosh\theta_k \sinh\theta_k \\ &= \cosh 2\theta_k + \sinh 2\theta_k \\ &= \frac{A_k - B_k}{\sqrt{A_k^2 - B_k^2}},\end{aligned} \tag{7.2}$$

where we have used our previous results from (5.15b),

$$\begin{aligned}\cosh 2\theta_k &= \frac{A_k}{\sqrt{A_k^2 - B_k^2}} \\ \sinh 2\theta_k &= -\frac{B_k}{\sqrt{A_k^2 - B_k^2}}.\end{aligned}$$

Thereby, the inelastic part of the dynamical structure factor at $T = 0$ reads

$$S_0^{xx}\left(k,\omega\right) = N\pi\left(S - n\right)\frac{A_k - B_k}{2\sqrt{A_k^2 - B_k^2}}\delta\left(\omega - \omega_k\right), \tag{7.4}$$

where $\omega_k := 2\sqrt{A_k^2 - B_k^2}$. In the limit of $\omega_k \to 0$, the dynamical structure factor (7.4) vanishes because $A_k = B_k$ for $\omega_k \to 0$.

7.3.1. Numerics

The dynamical structure factor in Eq. (7.4) can be visualized in various ways. We choose constant energy-cuts in order to compare our results with experimentally measured scattering intensities.

The data for the constant-energy cuts is obtained with a very simple `C++` program.

At first, the Dirac delta function in (7.4) is substituted by a Gaussian distribution, which is centered at ω_k with a standard deviation of σ_ω. A Gaussian distribution is a good replacement for the energy resolution of a detector triggered at energy ω. Reasonable values for the full width at half maximum

(FWHM), which is related to σ_ω via FWHM $= 2\sigma_\omega\sqrt{2\ln 2}$, can be extracted from experimental data and lie in the order of a few meV. The inelastic part of the dynamical structure factor per spin is given by

$$S^{xx}\left(k,\omega\pm\Delta\omega\right) = \pi\left(S-n\right)\frac{A_k - B_k}{2\sqrt{A_k^2 - B_k^2}}\cdot\frac{1}{\sigma_\omega\sqrt{2\pi}}\int\limits_{\omega-\Delta\omega}^{\omega+\Delta\omega}\mathrm{d}\omega'\,\exp\left[-\frac{1}{2}\left(\frac{\omega'-\omega_k}{\sigma_\omega}\right)^2\right]. \tag{7.5}$$

To extract a constant-energy cut with an energy window of $\omega\pm\Delta\omega$, the Brillouin zone is discretized and Eq. (7.5) is evaluated and integrated over the energy window for each value of k. The numerical integration is done using Romberg's method [82], which is quite fast and gives very accurate results. Alternatively, a pre-implemented error function could be used. The average occupation number n has already been calculated as a part of the staggered magnetization. The results are not normalized, i.e., they are displayed as shown in Eq. (7.5).

Furthermore, the effect of twinning is included. This effect occurs because no preferred direction exists at the structural transition from a tetragonal to an orthorhombic lattice, where the lattice constants a and b become unequal. Thus, the whole sample consists of equally distributed domains with randomly swapped a- and b-axis. Consequently, the structure factor at $k = (k_a, k_b, k_c)$ is simply the mean of the structure factor at $k = (k_a, k_b, k_c)$ and $k = (k_b, k_a, k_c)$.

7.3.2. Results & discussion

For all further evaluation of the dynamical structure factor, we stick to our parameters with a fixed value of $\nu = 0.5$ obtained by the fit to Zhao's measured spin wave velocities (see Tab. 7.4a). The visualization is realized with MATLAB. General results within the k_a-k_b plane with a fixed FWHM of 2 meV are shown in Fig. 7.3. All energy windows and values of k_c are identical to the ones chosen by Zhao *et al*. [10]. The reciprocal lattice vectors k_i are still given in units of π/(lattice constant).

For low energies (Fig. 7.3a and 7.3b), concentric spin wave rings emerge at the magnetic ordering vector $Q = (1, 0, 3)$. The rings are broadened for higher energies. In addition, less intensive spots $(1, 1, k_c)$ appear for $E = 100$ meV and $E = 115$ meV (Fig. 7.3c and 7.3d) which melt together with the concentric spin wave rings for higher energies (Fig. 7.3e and 7.3f). For high excitation energies, the situation is almost inverted to the one found at low energies. At the highest energy (Fig. 7.3h), only a very broad ring remains. In general, one observes the trend of decreasing intensity for increasing energy because $S(k,\omega) \propto 1/\omega_k$, see Eq. (7.4).

For a better comparison with constant-energy cuts extracted from neutron scattering data, we additionally extracted cuts of the dynamical structure factor with varying values of the FWHM, which are taken from Diallo *et al*. [9] (see Fig. 7.4). The constant-energy cuts are shown in Fig. 7.5 and are directly compared with the experimental results by Zhao *et al*.. As a reminder, our model does not include the spin wave gap, so deviations for small energies are expected. Although we have adopted the values of the FWHM from experiment, the excitations in our theoretical constant-energy cuts are

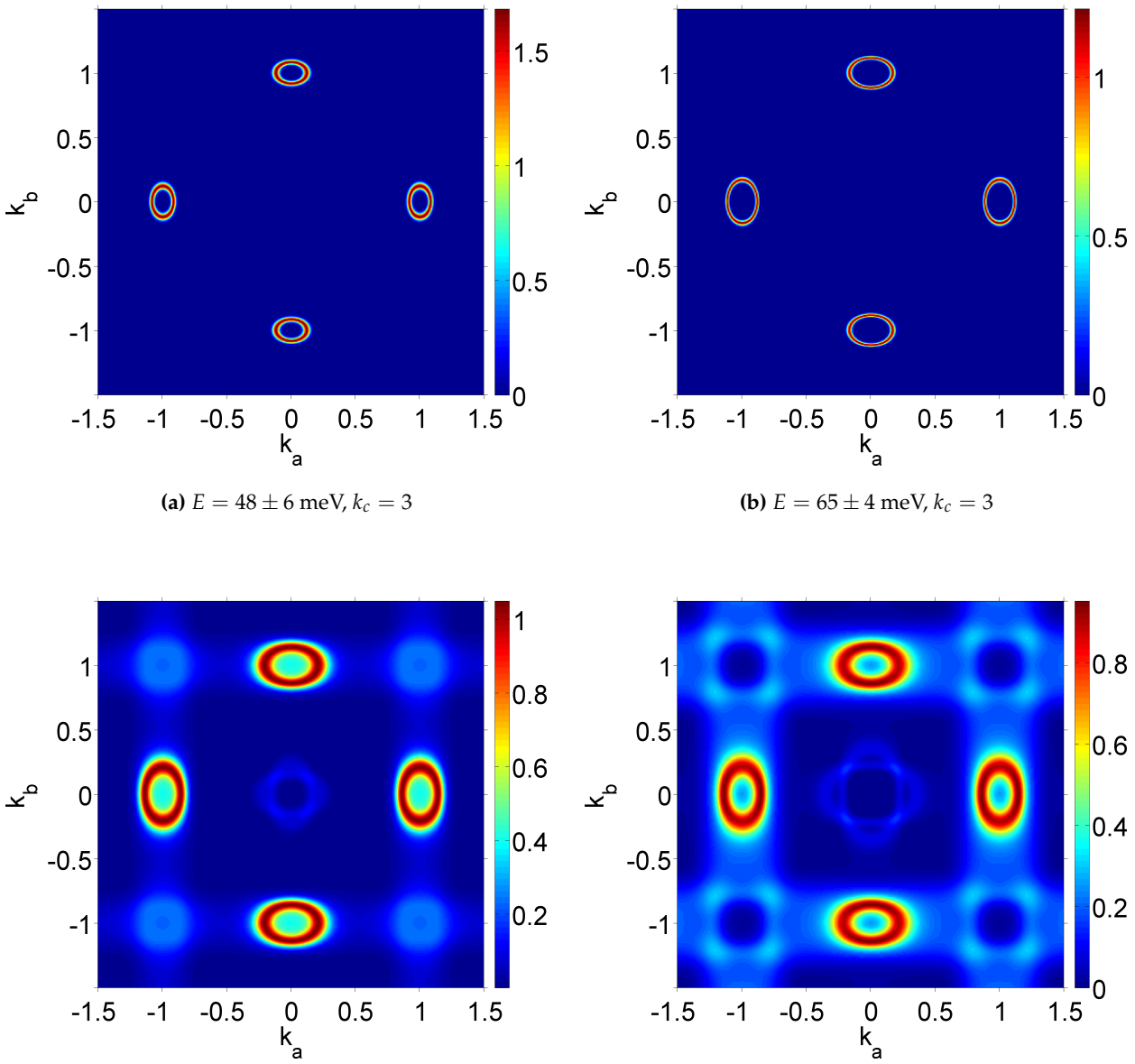

(a) $E = 48 \pm 6$ meV, $k_c = 3$

(b) $E = 65 \pm 4$ meV, $k_c = 3$

(c) $E = 100 \pm 10$ meV, $k_c = 3.5$

(d) $E = 115 \pm 10$ meV, $k_c = 4$

Fig. 7.3.: Constant-energy cuts (twinned) of the dynamical structure factor per spin (7.5). FWHM is 2 meV for all cuts.

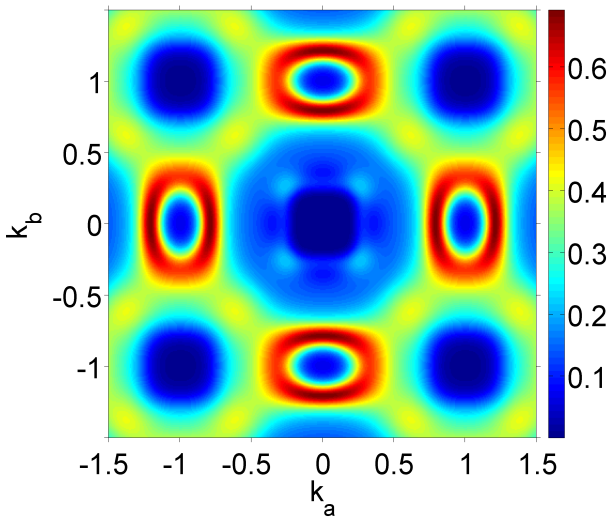

(e) $E = 137 \pm 15$ meV, $k_c = 4$

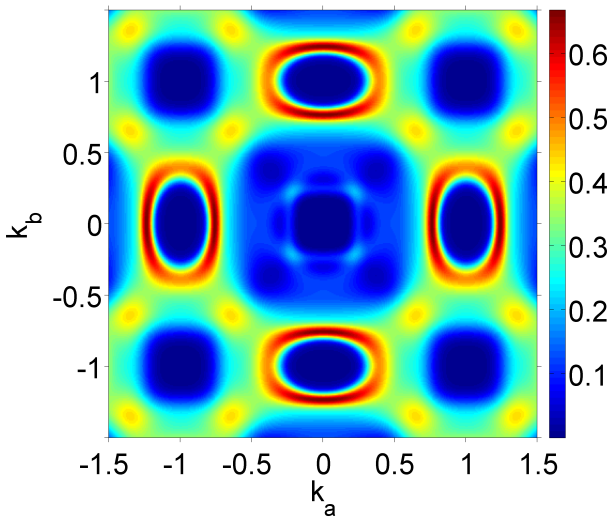

(f) $E = 135 \pm 10$ meV, $k_c = 4.5$

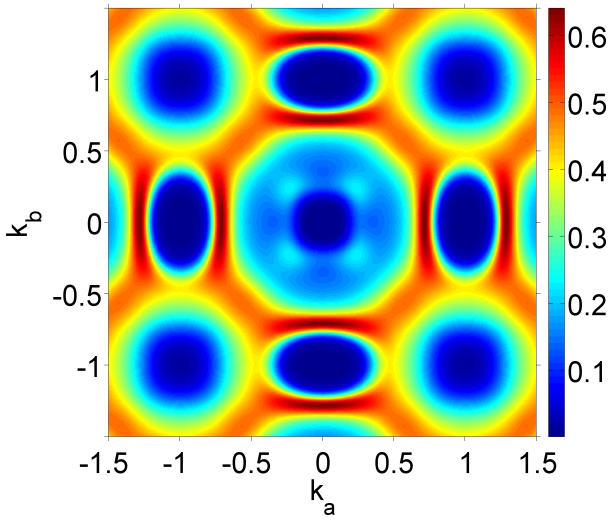

(g) $E = 144 \pm 15$ meV, $k_c = 5$

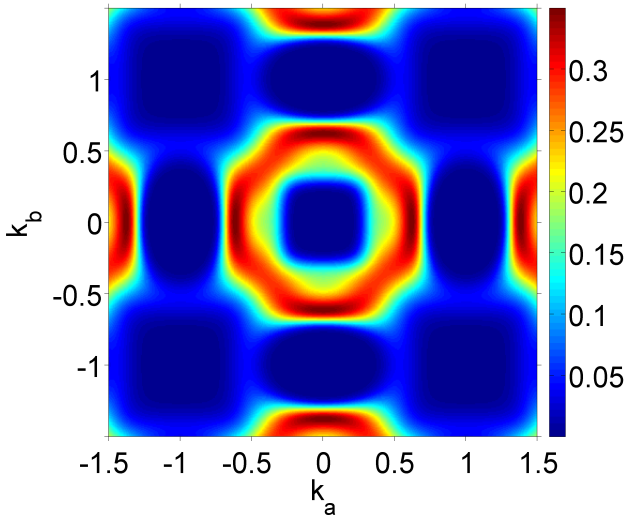

(h) $E = 175 \pm 15$ meV, $k_c = 5.2$

Fig. 7.3.: (Continued) Constant-energy cuts (twinned) of the dynamical structure factor per spin (7.5). FWHM is 2 meV for all cuts.

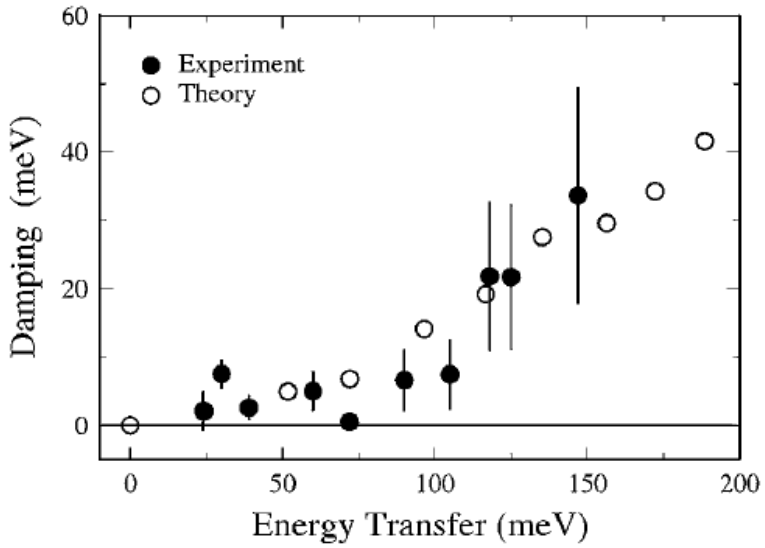

Fig. 7.4.: Values for the FWHM: Spectral half width at half maximum derived from band-structure calculated peaks and spin wave relaxation rate (Figure taken from Diallo *et al*. [9]).

still very well defined. This is caused by our resolution in momentum space which is almost infinite compared to the limited momentum resolution in experiment.

Our theoretical predictions agree with the measurements in certain aspects. The concentric rings arising from the magnetic ordering vector can clearly be identified in the experimental results. However, high scattering intensities are detected which are not part of our theoretical predictions. In particular, this effect is very strong at $k = (1.5, 3, 4)$ in the plot for $E = 137 \pm 15$ meV (Fig. 7.5e). The scattering intensities centered in $k = (1.5, 3, 4)$ are as high as the intensities of the concentric ring in the middle. In our calculations, high intensities are predicted for the concentric spin wave ring, whereas the spot close to $k = (1.5, 3, 4)$ shows medium intensity. The measured intensities are not symmetric around $k_b = 2$ because of blind spots in the detector.

The effect also occurs in the cuts for $E = 100 \pm 10$ (Fig. 7.5c) and $E = 135 \pm 10$ (Fig. 7.5f), but it is less distinct. In the constant-energy cut for $E = 144 \pm 15$ (Fig. 7.5g), the agreement is better, because all other spots show a intensity similar to the concentric ring. However, the measured intensities are not symmetric, which is surprising.

In Fig. 7.6, the fitted dispersion for $\nu = 0.5$ is plotted in the k_a-k_b-plane for $k_c = 4$. It is obvious that the medium ranged intensities of the legs in Fig. 7.5e are caused by the local maximum at $k = (1.5, 3, 4)$. Because the extrema close to $k = (3, 1.5, 4)$ has a higher energy > 150 meV, the intensity is smaller due to the twinned domains. Thus, higher intensities would be predicted if the dispersion was symmetric in these momenta.

In the constant-energy cut with $E = 175 \pm 15$ meV (Fig. 7.5h), small intensities located in the center of the cut are measured while they are not expected from our theoretical calculation. Since the deviation in momentum from the gapless Goldstone mode is very small at $k = (1, 0, 5.2)$, the excitations are

located at low energies. For the twinned case, we observe a local minimum at $k = (0, 1, 5.2)$ with $\omega_k \approx 100$ meV (see Fig. 7.7). Hence, we do not observe any intensity in our model. In case of a ferromagnetic exchange parallel to the spin stripes, the local minimum at $k = (0, 1, 5.2)$ should vanish and the excitation energy should increase to higher energies, see previous sections. Consequently, scattering intensities should be measurable.

The rectangle with the highest intensities in Fig. 7.5h is probably related to our calculated structure. But one must be aware, that the difference between the maximal and minimal intensities is quite small in experiment as well as in our calculations. Thus, it could be quite hard to distinguish the magnetic modes from the background when analyzing the experimental data.

Due to the effect of twinning, it would rather be difficult to distinguish the modes at $k = (0, 1, 0)$ and $k = (1, 0, 0)$ in our model, because they are of similar magnitude. Consequently, our theoretical scenario would require a deeper and more detailed analysis of experimental data to distinguish between the existence of these two modes.

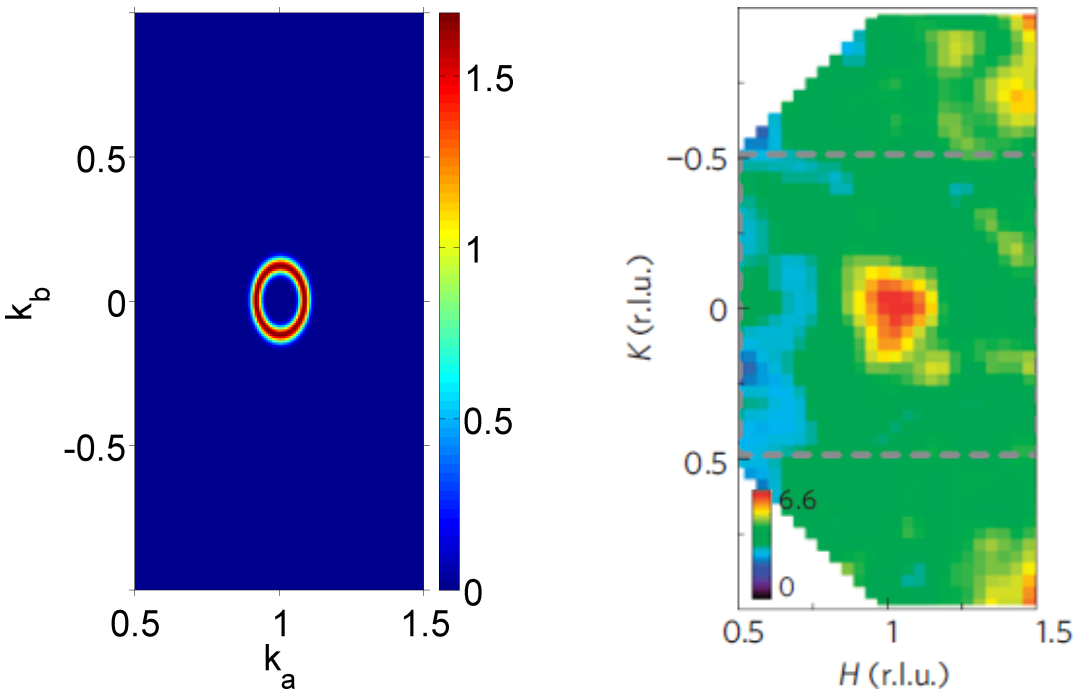

(a) $E = 48 \pm 6$ meV, $k_c = 3$, FWHM $= 4$ meV

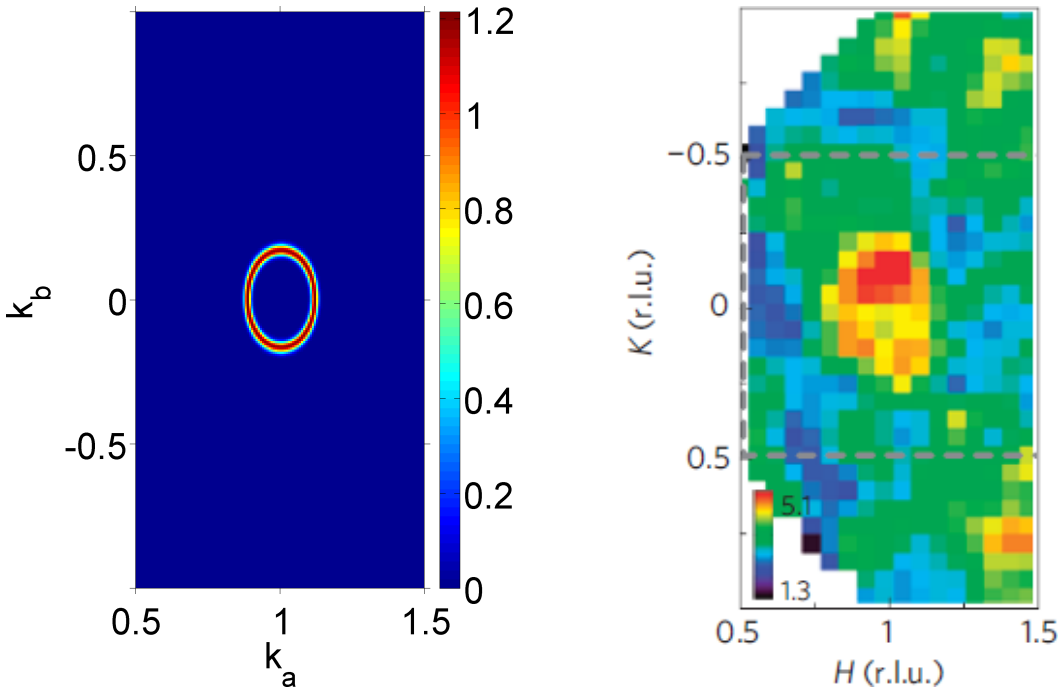

(b) $E = 65 \pm 4$ meV, $k_c = 3$, FWHM $= 5$ meV

Fig. 7.5.: Constant-energy cuts (twinned) with varying values of the FWHM (left) and experimental results (right) taken from Ref. [10].

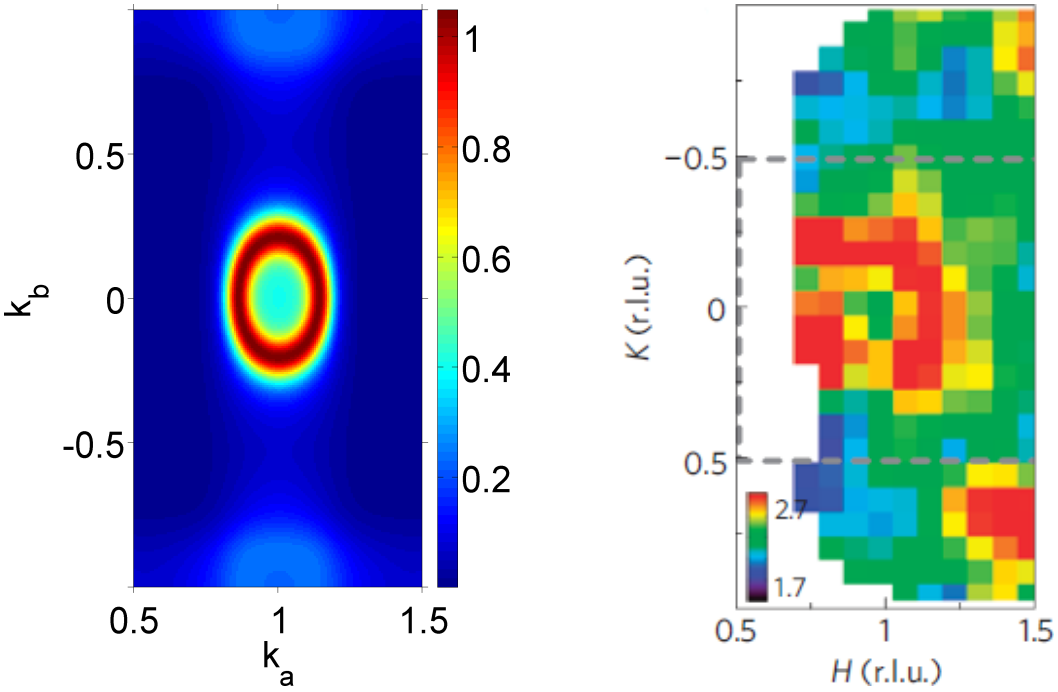

(c) $E = 100 \pm 10$ meV, $k_c = 3.5$, FWHM $= 7$ meV

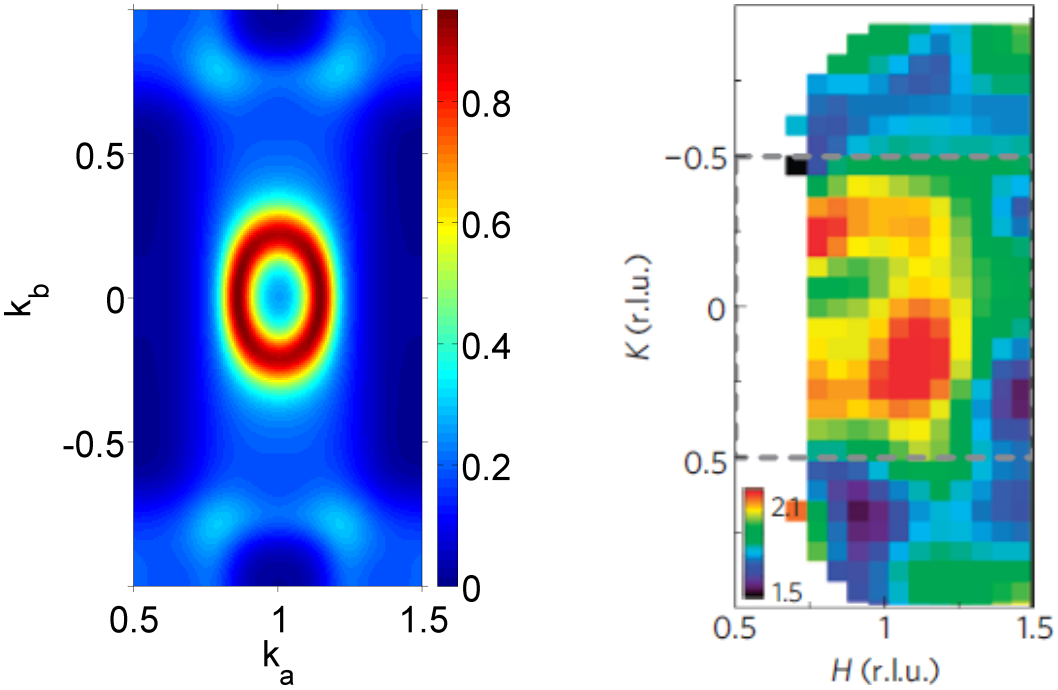

(d) $E = 115 \pm 10$ meV, $k_c = 4$, FWHM $= 18$ meV

Fig. 7.5.: (Continued) Constant-energy cuts (twinned) with varying values of the FWHM (left) and experimental results (right) taken from Ref. [10].

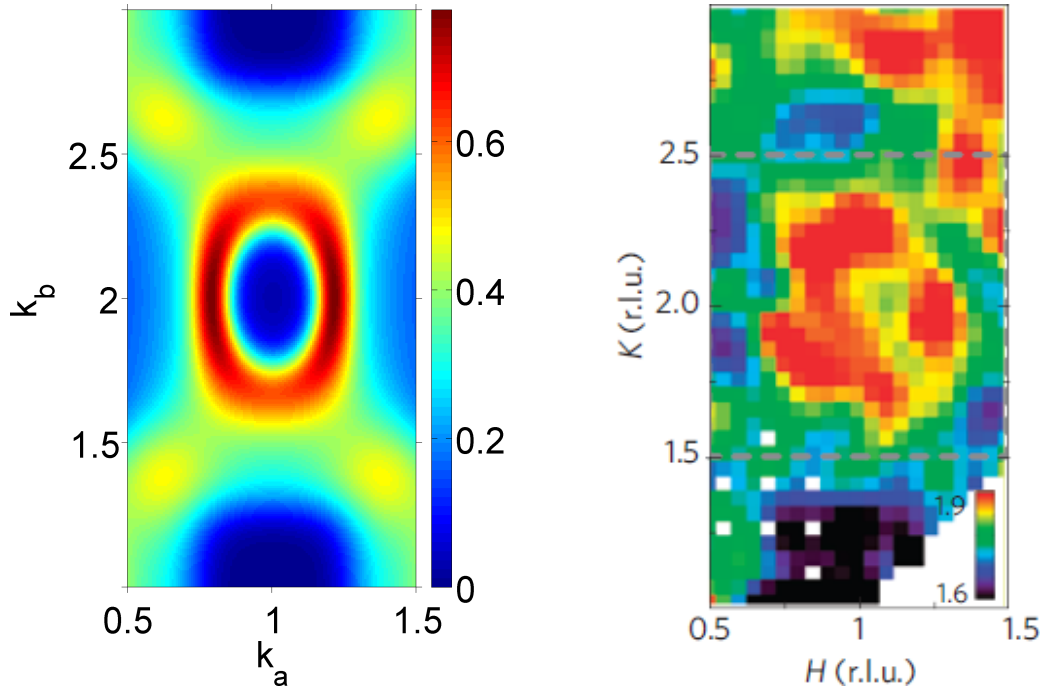

(e) $E = 137 \pm 15$ meV, $k_c = 4$, FWHM $= 28$ meV

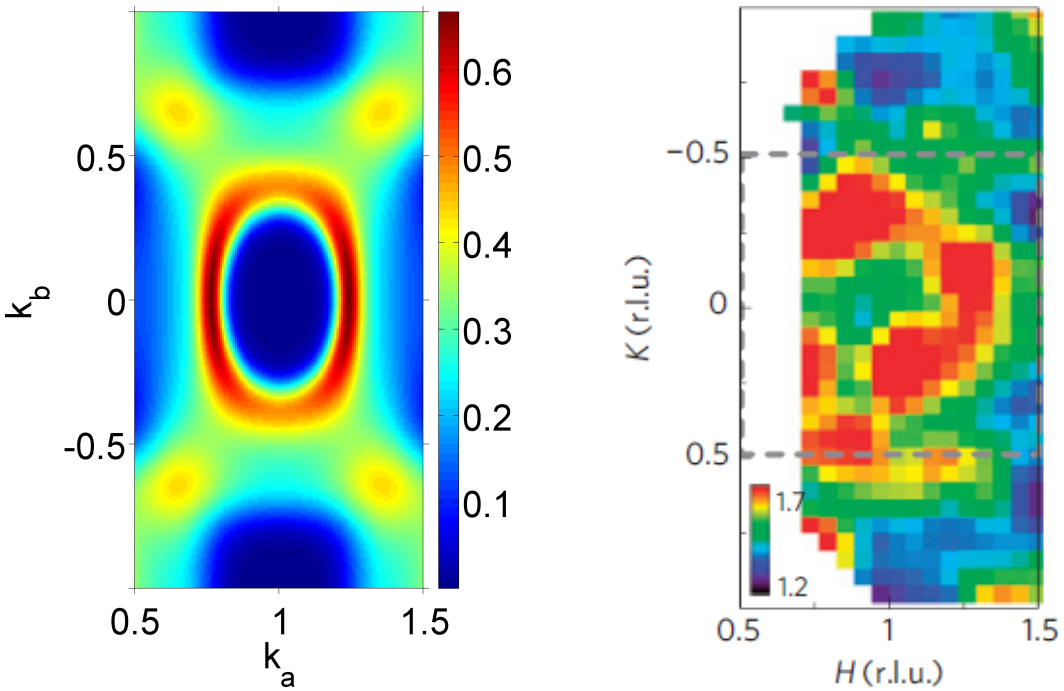

(f) $E = 135 \pm 10$ meV, $k_c = 4.5$, FWHM $= 28$ meV

Fig. 7.5.: (Continued) Constant-energy cuts (twinned) with varying values of the FWHM (left) and experimental results (right) taken from Ref. [10].

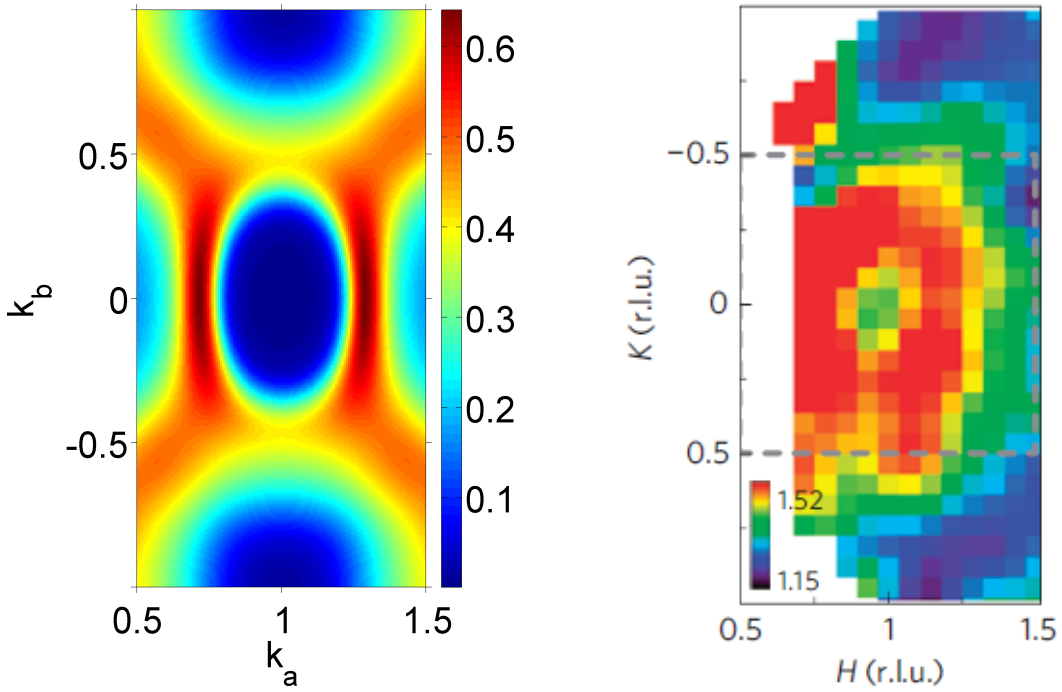

(g) $E = 144 \pm 15$ meV, $k_c = 5$, FWHM $= 32$ meV

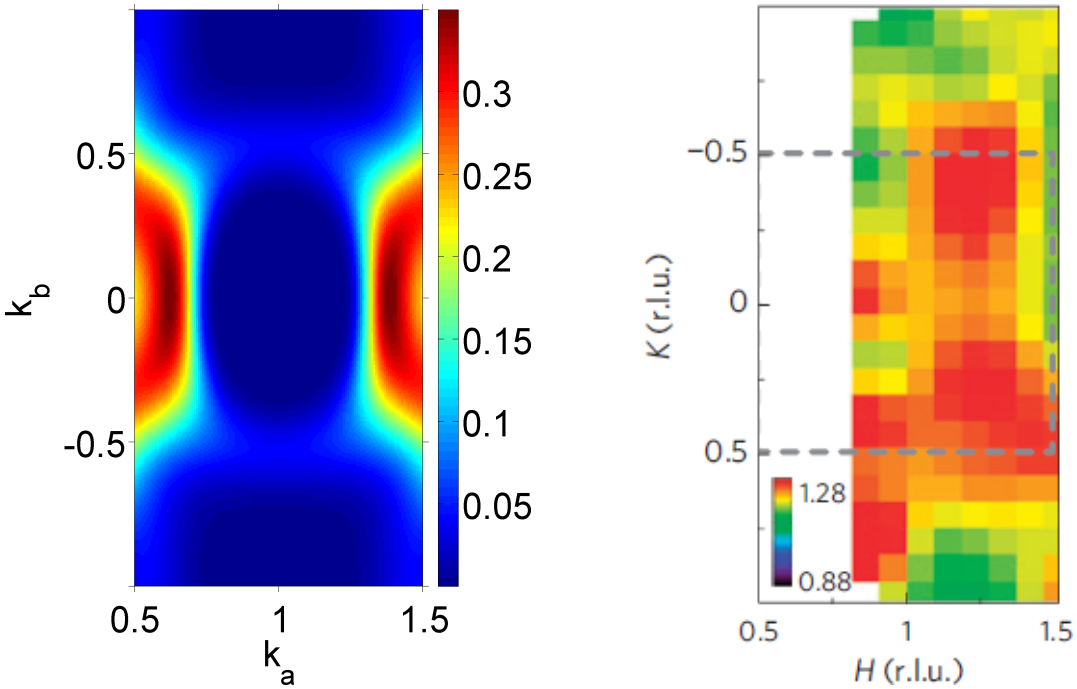

(h) $E = 175 \pm 15$ meV, $k_c = 5.2$, FWHM $= 39$ meV

Fig. 7.5.: (Continued) Constant-energy cuts (twinned) with varying values of the FWHM (left) and experimental results (right) taken from Ref. [10].

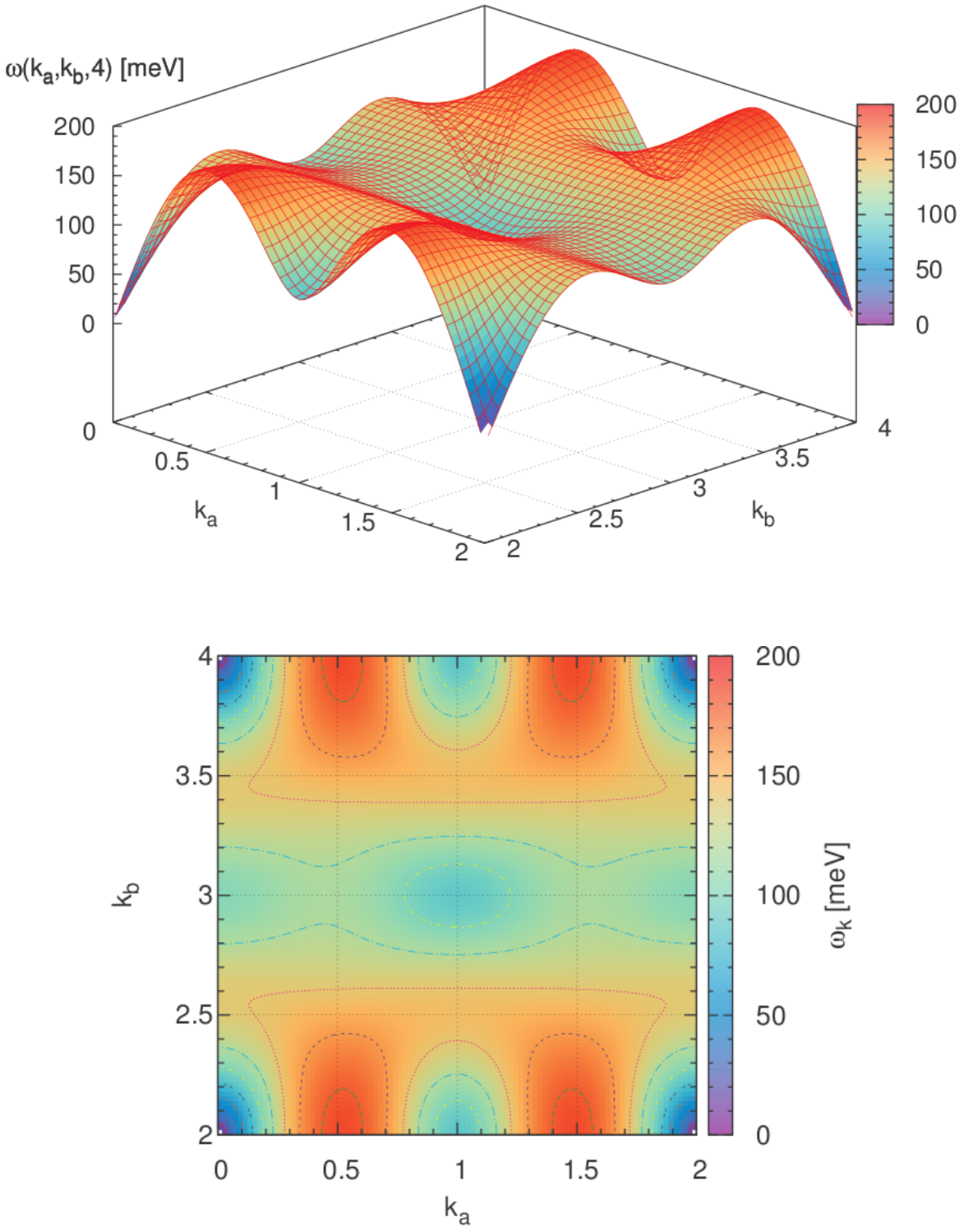

Fig. 7.6.: Fitted dispersion for $\nu = 0.5$ and $k_c = 4$.

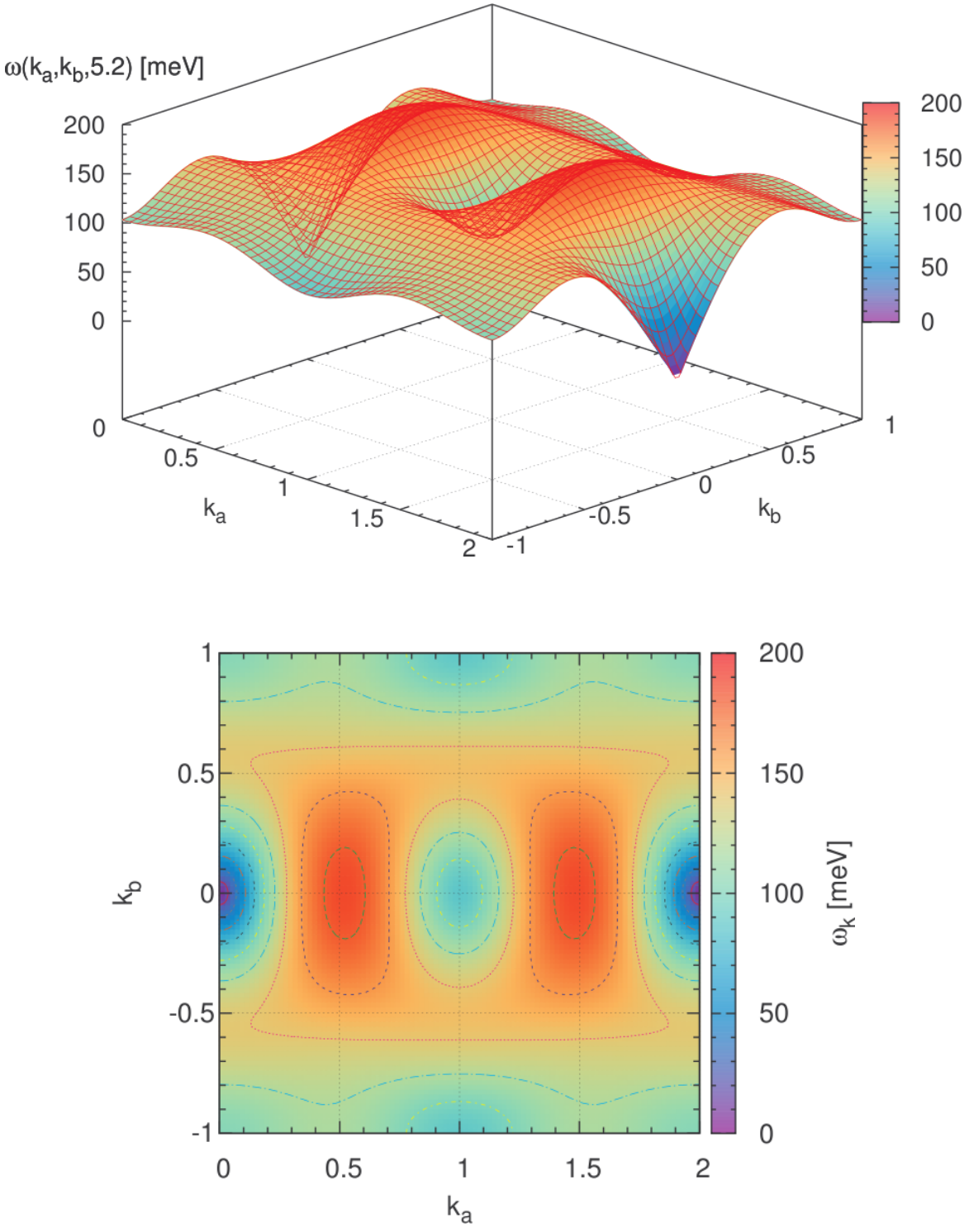

Fig. 7.7.: Fitted dispersion for $\nu = 0.5$ and $k_c = 5.2$.

8. Conclusion & outlook

In this thesis, we studied the three dimensional collinear ordered phase with respect to the magnetic excitations and the application for iron pnictides. The three dimensional character of the magnetism in the iron pnictides was revealed in recent inelastic neutron scattering studies [8, 10, 15]. Hence, we extended the studies of the two dimensional collinear phase within a frustrated J_1-J_2-Heisenberg model by Uhrig *et al*. to three dimensions. The localized Heisenberg model for spin $S = 1$ is chosen on the base of experimental and theoretical results. The model was studied within self-consistent spin wave theory, which is an advantageous approach compared to the common linear spin wave theory because the effect of renormalization due to quantum mechanical fluctuations is included.

In addition, we introduced a biquadratic exchange motivated by the measured anisotropy in the collinear ordered planes and density functional calculations by Yaresko *et al*.. An appropriate mean field decoupling for the Dyson-Maleev as well as for the Schwinger bosons representation was introduced for the bilinear and biquadratic exchange. The method was applied to the two dimensional Néel phase and the results were compared to results obtained by exact diagonalization and series expansion. We found the influence of the biquadratic exchange to be heavily overestimated within the Schwinger bosons representation. Hence, the Dyson-Maleev representation is the best choice for our purposes.

The approximation was applied to the frustrated J_1-J_2-J_c Heisenberg model with and without biquadratic exchange J_{bq} in the three dimensional collinear phase, where the interlayer coupling J_c is also antiferromagnetic. To derive the spin wave dispersion and the ground state energy, the mean field Hamiltonian was diagonalized using a standard Bogoliubov transformation. The set of self-consistent equations for the introduced quantum correction parameters was solved numerically with multidimensional root finding and integration.

As expected, the collinear phase is stabilized by the interlayer exchange. Furthermore, we studied the behavior of the critical point where our spin wave theory breaks down. On the one hand, we identified the magnetization-driven scenario where the phase collapses because of the vanishing magnetic long-range order. On the other hand, the spin wave velocity v_b vanishes first in the velocity-driven scenario. Surprisingly, the staggered magnetization obtains a finite value when the collinear phase ceases to exist in this scenario. The transition between both scenarios depends on the interlayer coupling $\mu = J_c/J_1$ and on the spin S. For small values of μ and $S = 1/2$ or $S = 1$, the magnetization-driven scenario occurs. The velocity-driven scenario occurs for large μ or $S \geq 3/2$. The finite staggered magnetization in the velocity-driven scenario is caused by the cut-off of the logarithmic divergence in the integrand of the staggered magnetization. If the interlayer coupling is sufficiently high, the renormalization of the staggered magnetization is too weak to push is down to zero.

Under the influence of a biquadratic exchange, both the exchange parallel and perpendicular to the spin stripes are strengthened. Compared to the exchange parallel to the spin stripes, the exchange perpendicular to the spin stripes experiences a much stronger renormalization which leads to the anisotropy between the effective exchange constants $\tilde{J}_{1a}$ and $\tilde{J}_{1b}$. Hence, we provided a method for introducing an anisotropy in the exchange constants without having to introduce ab-initio direction dependent exchange constants. While the influence of the biquadratic exchange on the dispersion along the high symmetric k_a-k_c-direction is rather small, the minimum of the dispersion at $k = (0,1,0)$ is lifted. Because the effective exchange parallel to the spin stripes is always weakly strengthened, the minimum at $k = (1,0,1)$ will likely never vanish. This would require an effective ferromagnetic exchange $\tilde{J}_{1b} < 0$. With increasing $\nu = J_{\mathrm{bq}}/J_1$, the critical point is shifted towards lower ratios of $x = J_1/J_2$, which limits the maximum possible biquadratic exchange ν.

For different experimental results for iron pnictides, we determined the parameters of our model by fitting it to the measured ratios of the spin wave velocities. Thereby the whole dispersion was obtained by reproducing the spin wave velocity v_b parallel to the spin stripes. We found that our model reproduces the experimental dispersion and inelastic neutron scattering data for $CaFe_2As_2$ in the direction perpendicular to the spin stripes and between the layers very well. In the direction parallel to the spin stripes, the agreement with inelastic neutron scattering data for excitations up to $\sim$ 100 meV is also very nice and accurate for the parameters obtained for $CaFe_2As_2$. For higher energies and momenta in b-direction, discrepancies are observed. Our model shows a minimum at $k = (0,1,0)$, while a maximum is detected in the experimental results by Zhao *et al.*. Therefore, even a ferromagnetic exchange parallel to the spin stripes would be necessary, which cannot be induced by the biquadratic exchange in our model. Thus, we have arrived at a scenario which is located between the result with no anisotropy and the measured scenario by Zhao *et al.*. The proper situation is not completely clarified, since there is no other neutron scattering data at high energies available except Zhao's data. In contrast to the experimental results for $CaFe_2As_2$, the spin wave velocities proposed by Ong *et al.* lead to a very low energy mode in the direction parallel to the spin stripes. The agreement in k_a- and k_c-direction is fine because the corresponding spin wave velocities were also taken from experiment. Further neutron scattering studies would certainly help to clarify the situation. Especially at $k = (0,1,0)$, we would like to see modes at lower energies, which might have been missed in current studies because the experimentalists concentrated on higher energies.

In addition, we calculated the dynamical structure factor, which is proportional to neutron scattering cross section. We compared it with the results by Zhao *et al.*. While there is a nice agreement in the excitations originating from the magnetic ordering vector, our theoretical expectation cannot explain the whole data because the anisotropy in our model is too weak compared to Zhao's results. Especially the distinction of the energies parallel and perpendicular to the spin stripes is tough when they are of similar magnitude. This effect is caused by the twinning of crystal domains and affects our model with biquadratic exchange.

Previous studies suggested that iron pnictides are close to a quantum phase transition, which is connected to a strong renormalization of the local magnetic moment due to quantum fluctuations. For the proposed value of the spin wave velocity v_b for $Sr/BaFe_2As_2$ by Ong *et al.*, our model of the three dimensional collinear phase reproduces this result. In contrast, recent neutron scattering studies by Zhao *at al.* and Diallo *et al.* tell a different story. Their measured a much higher value of the spin

wave velocity v_b in $CaFe_2As_2$, which leads to the result that the iron pnictides reside deeply in the collinear phase. Thus, the small measured local magnetic moment has to be reduced by other effects for example such as itineracy and hybridization. At this point, it is hard to make a final conclusion on that question. The inelastic neutron scattering studies focused on high energies. Hence, a mode at low energies, which would speak in favor of Ong's suggestion, might have been missed.

In conclusion, our model of the three dimensional collinear phase, studied within self-consistent spin wave, can explain the experimental dispersion found in the 122 pnictide $CaFe_2As_2$ in *a*-, *c*- and partly in $b-$ direction. However, there are still open issues concerning the spin wave excitations in the iron pnictides which cannot be resolved in this thesis. It is obvious, that further adjustments of our model are necessary to eliminate all discrepancies between our theory and the experimental results. In particular, the anisotropy of the the exchange within the collinear ordered planes planes has to be more increased to reach complete agreement with Zhao's data. It might also be possible that a localized model is not sufficient because there are experimental facts which speak in favor of a more itinerant approach to the magnetism. Attempts were made by combining a localized and an itinerant approach by Lv *et al*. [66]. The interaction between the itinerant electrons and the local moments is realized via a ferromagnetic Hund's coupling. Furthermore, more experimental studies of the magnetic excitations in the iron pnictides would be welcomed to clarify the situation.

Outlook

Future work should include the introduction of a single-ion or nearest neighbor anisotropy, in order to take respect of the experimentally measured spin gap. In addition, the biquadratic exchange should be introduced between next nearest neighbors. There is actually no reason why it should not be important for next nearest neighbor exchange when it is relevant for nearest neighbor exchange. Furthermore, the model could be fitted to a wider class of iron pnictides, especially 1111 pnictides, or even iron chalcogenides. As the present work is restricted to zero temperature, the extension to finite temperature lies close as well. In particular, the temperature dependence of the dispersion, the staggered magnetization and the dynamical structure factor are of great interest.

Moreover, a detailed study of the critical point and the transition between the magnetization- and velocity-driven scenario would be desirable, as our studies are based mainly on empirical facts.

To include the charge degrees of freedom, the model has to be extended to a generalized *t-J* model. Thereby, the mutual influence between the spin and the charges can be studied. Especially the Landau-type damping of the spin waves and the influence upon external doping is of great interest. Doping increases the effect of the charge degrees of freedom and leads to a breakdown of the long-range magnetic order in the superconducting phase. By using a combination of continuous unitary transformations (CUTs), effective models can be derived to study the different aspects of the interaction.

A. Conventions

Throughout the entire thesis, several conventions regarding transformations and notation are used. This section summarizes them.

A.1. Notation & units

We use units where $\hbar = k_b = 1$. Consequently, $\beta = 1/T$ is the inverse temperature.

The indices i, j indicate lattice points with the position vectors r_i and r_j, respectively.
k, k' and so on are reciprocal lattice vectors. All reciprocal lattice vectors are measured in units of π/lattice constant. For brevity, vectors are not marked with arrows.

A.2. Fourier transform

As we are dealing with crystal lattices, discrete Fourier transforms between position and momentum space are used. The Fourier transform of the bosonic creation/annihilation operators is given by

$$c_i := \frac{1}{\sqrt{N}} \sum_k \mathrm{e}^{ikr_i} c_k \tag{A.1a}$$

$$c_i^\dagger := \frac{1}{\sqrt{N}} \sum_k \mathrm{e}^{-ikr_i} c_k^\dagger, \tag{A.1b}$$

as they have to be hermitian conjugates. N is the number of lattice points. Thus, the inverse Fourier transforms are given by

$$c_k := \frac{1}{\sqrt{N}} \sum_i \mathrm{e}^{-ikr_i} c_i \tag{A.1c}$$

$$c_k^\dagger := \frac{1}{\sqrt{N}} \sum_i \mathrm{e}^{ikr_i} c_i^\dagger. \tag{A.1d}$$

For all other operators A, the following convention is used:

$$A_i := \frac{1}{N} \sum_k \mathrm{e}^{ikr_i} A_k \tag{A.2a}$$

$$A_i^\dagger := \frac{1}{N} \sum_k \mathrm{e}^{-ikr_i} A_k^\dagger. \tag{A.2b}$$

The inverse Fourier transform then reads

$$A_k := \sum_i \mathrm{e}^{-ikr_i} A_i \tag{A.2c}$$

$$A_k^\dagger := \sum_i \mathrm{e}^{ikr_i} A_i^\dagger. \tag{A.2d}$$

The expression

$$f(t) := \frac{1}{2\pi} \int_{-\infty}^{\infty} \mathrm{d}\omega \, \mathrm{e}^{-i\omega t} f(\omega) \tag{A.3a}$$

describes the continuous Fourier transform between time and frequency space.

$$f(\omega) := \int_{-\infty}^{\infty} \mathrm{d}t \, \mathrm{e}^{i\omega t} f(t) \tag{A.3b}$$

is the corresponding inverse transformation.

A.3. Dirac delta function

The Fourier transform of the Dirac delta function in momentum space is

$$\delta(k) = \frac{1}{N} \sum_i \mathrm{e}^{-ikr_i}. \tag{A.4}$$

In order to calculate the result when the sum is restricted to one of the sublattices, we split the sum in A.4 up

$$\delta(k) = \frac{1}{N} \sum_{i \in A} \mathrm{e}^{-ikr_i} + \frac{1}{N} \sum_{i \in B} \mathrm{e}^{-ikr_i} \tag{A.5a}$$

and we additionally investigate

$$\delta(k+Q) = \frac{1}{N} \sum_{i \in A} \mathrm{e}^{-i(k+Q)r_i} + \frac{1}{N} \sum_{i \in B} \mathrm{e}^{-i(k+Q)r_i}. \tag{A.5b}$$

Q is the magnetic ordering vector which is defined via the relation

$$\mathrm{e}^{\pm iQr_i} = \begin{cases} +1, & r_i \in A \\ -1, & r_i \in B. \end{cases} \tag{A.6}$$

Without loss of generality, the origin r_0 of the lattice has been set in the A sublattice. Consequently, the sum over the sublattice B in A.5b obtains a phase factor of -1:

$$\delta\left(k+Q\right) = \frac{1}{N}\sum_{i\in A}\mathrm{e}^{-ikr_i} - \frac{1}{N}\sum_{i\in B}\mathrm{e}^{-ikr_i}, \tag{A.7}$$

while there is no effect for all lattice vectors in A. For $r_0 \in B$, the signs would be inverted.

Adding and subtracting equations A.5a and A.7, we derive the two identities

$$\frac{1}{N}\sum_{i\in A}\mathrm{e}^{-ikr_i} = \frac{1}{2}\Big(\delta\left(k\right) + \delta\left(k+Q\right)\Big) \tag{A.8a}$$

$$\frac{1}{N}\sum_{i\in B}\mathrm{e}^{-ikr_i} = \frac{1}{2}\Big(\delta\left(k\right) - \delta\left(k+Q\right)\Big), \tag{A.8b}$$

for sums restricted to one sublattice.

B. Contractions

This chapter summarizes all possible contractions in the Dyson-Maleev representation, which appear as prefactors of the decoupled biquadratic term in order S^2 and lower. We only regard the prefactors of terms which result in bilinear terms. For convenience, only the prefactors of each term of operators are listed.

B.1. Antiferromagnetic bonds

The non-vanishing expectation values are

$$n := \left\langle b_i^\dagger b_i \right\rangle = \left\langle b_j^\dagger b_j \right\rangle \tag{B.1a}$$

$$a := \left\langle b_i^\dagger b_j^\dagger \right\rangle = \left\langle b_i \, b_j \right\rangle . \tag{B.1b}$$

We assume that they are all real. For easier reference, we define the operators

$$\hat{I}_0 := b_i^\dagger b_j^\dagger + b_i \, b_j \tag{B.2a}$$

$$\hat{I}_0' := b_i^\dagger \hat{n}_i \, b_j^\dagger + b_i \, \hat{n}_j \, b_j . \tag{B.2b}$$

The prefactors of $\hat{n}_j$ and $b_i \, b_j$ are identical to the prefactors of $\hat{n}_i$ and $b_i^\dagger b_j^\dagger$, respectively.

B.1.1. $\mathcal{O}(S^2)$

B.1.1.1. Prefactor of $\hat{n}_i$

- $\hat{n}_i^2 + \hat{n}_j^2 + 4\hat{n}_i\hat{n}_j$:

  $b_i^\dagger b_i \, b_i^\dagger b_i \longrightarrow 4n + 1$ $\qquad$ $b_i^\dagger b_i \, b_j^\dagger b_j \longrightarrow n$

- $\hat{I}_0^2$:

  $b_i^\dagger b_j^\dagger b_i^\dagger b_j^\dagger \longrightarrow 0$ $\qquad$ $b_i^\dagger b_j^\dagger b_i \, b_j \longrightarrow n$

  $b_i \, b_j \, b_i \, b_j \longrightarrow 0$ $\qquad$ $b_i \, b_j \, b_i^\dagger b_j^\dagger \longrightarrow n + 1$

- $\hat{n}_i \hat{I}_0 + \hat{I}_0 \hat{n}_i$:

$$b_i^\dagger b_i\, b_i^\dagger b_j^\dagger \longrightarrow 2a \qquad b_i^\dagger b_j^\dagger b_i^\dagger b_i \longrightarrow 2a$$
$$b_i^\dagger b_i\, b_i\, b_j \longrightarrow 2a \qquad b_i\, b_j\, b_i^\dagger b_i \longrightarrow 2a$$

- $\hat{I}_0'$:

$$b_i^\dagger b_i^\dagger b_i\, b_j^\dagger \longrightarrow 2a \qquad b_i\, b_j^\dagger b_j\, b_j \longrightarrow 0$$

In total:

$$\sum = 10\,(n+a) + 2$$

B.1.1.2. Prefactor of $b_i^\dagger b_j^\dagger$

- $\hat{n}_i^2 + \hat{n}_j^2 + 4\hat{n}_i\hat{n}_j$:

$$b_i^\dagger b_i\, b_i^\dagger b_i \longrightarrow 0 \qquad b_i^\dagger b_i\, b_j^\dagger b_j \longrightarrow a$$

- $\hat{I}_0^2$:

$$b_i^\dagger b_j^\dagger b_i^\dagger b_j^\dagger \longrightarrow 4a \qquad b_i^\dagger b_j^\dagger b_i\, b_j \longrightarrow a$$
$$b_i\, b_j\, b_i\, b_j \longrightarrow 0 \qquad b_i\, b_j\, b_i^\dagger b_j^\dagger \longrightarrow a$$

- $\hat{n}_i \hat{I}_0 + \hat{I}_0 \hat{n}_i$:

$$b_i^\dagger b_i\, b_i^\dagger b_j^\dagger \longrightarrow 2n+1 \qquad b_i^\dagger b_j^\dagger b_i^\dagger b_i \longrightarrow 2n$$
$$b_i^\dagger b_i\, b_i\, b_j \longrightarrow 0 \qquad b_i\, b_j\, b_i^\dagger b_i \longrightarrow 0$$

- $\hat{n}_j \hat{I}_0 + \hat{I}_0 \hat{n}_j$:

$$b_j^\dagger b_j\, b_i^\dagger b_j^\dagger \longrightarrow 2n+1 \qquad b_i^\dagger b_j^\dagger b_j^\dagger b_j \longrightarrow 2n$$
$$b_j^\dagger b_j\, b_i\, b_j \longrightarrow 0 \qquad b_i\, b_j\, b_j^\dagger b_j \longrightarrow 0$$

- $\hat{I}_0'$:

$$b_i^\dagger b_i^\dagger b_i\, b_j^\dagger \longrightarrow 2n \qquad b_i\, b_j^\dagger b_j\, b_j \longrightarrow 0$$

In total:

$$\sum = 10\,(n+a) + 2$$

B.1.2. $\mathcal{O}(S)$

B.1.2.1. Prefactor of $\hat{n}_i$

- $-2(\hat{n}_i\hat{n}_j^2 + \hat{n}_i^2\hat{n}_j)$:

$$b_i^\dagger b_i\, b_j^\dagger b_j\, b_j^\dagger b_j \longrightarrow 2n^2 + n \qquad b_i^\dagger b_i\, b_i^\dagger b_i\, b_j^\dagger b_j \longrightarrow 4n^2 + 4a^2 + n$$

- $-\frac{1}{2}(\hat{I}_0\hat{I}_0' + \hat{I}_0\hat{I}_0')$:

$$\begin{aligned} b_i^\dagger b_j^\dagger b_i^\dagger b_i^\dagger b_i\, b_j^\dagger &\longrightarrow 6a^2 & b_i^\dagger b_i^\dagger b_i\, b_j^\dagger b_i^\dagger b_j^\dagger &\longrightarrow 6a^2 \\ b_i\, b_j\, b_i^\dagger b_i^\dagger b_i\, b_j^\dagger &\longrightarrow 4a^2 + 4n^2 + 6n + 2 & b_i^\dagger b_i^\dagger b_i\, b_j^\dagger b_i\, b_j &\longrightarrow 4n^2 + 4a^2 \\ b_i^\dagger b_j^\dagger b_i\, b_j^\dagger b_j\, b_j &\longrightarrow 2n^2 & b_i\, b_j^\dagger b_j\, b_j\, b_i^\dagger b_j^\dagger &\longrightarrow 2n^2 + 2n \\ b_i\, b_j\, b_i\, b_j^\dagger b_j\, b_j &\longrightarrow 0 & b_i\, b_j^\dagger b_j\, b_j\, b_i\, b_j &\longrightarrow 0 \end{aligned}$$

- $-\frac{1}{2}[(\hat{n}_i + \hat{n}_j)\hat{I}_0' + \hat{I}_0'(\hat{n}_i + \hat{n}_j)]$:

$$\begin{aligned} b_i^\dagger b_i\, b_i^\dagger b_i^\dagger b_i\, b_j^\dagger &\longrightarrow 12na + 4a & b_i^\dagger b_i^\dagger b_i\, b_j^\dagger b_i^\dagger b_i &\longrightarrow 12na + 2a \\ b_i^\dagger b_i\, b_i\, b_j^\dagger b_j\, b_j &\longrightarrow 4na & b_i\, b_j^\dagger b_j\, b_j\, b_i^\dagger b_i &\longrightarrow 4na \\ b_j^\dagger b_j\, b_i^\dagger b_i^\dagger b_i\, b_j^\dagger &\longrightarrow 4na + 2a & b_i^\dagger b_i^\dagger b_i\, b_j^\dagger b_j^\dagger b_j &\longrightarrow 4na \\ b_j^\dagger b_j\, b_i\, b_j^\dagger b_j\, b_j &\longrightarrow 0 & b_i\, b_j^\dagger b_j\, b_j\, b_j^\dagger b_j &\longrightarrow 0 \end{aligned}$$

- $-\hat{n}_i\hat{n}_j\hat{I}_0 - \hat{I}_0\hat{n}_i\hat{n}_j$:

$$\begin{aligned} b_i^\dagger b_i\, b_j^\dagger b_j\, b_i^\dagger b_j^\dagger &\longrightarrow 4na + 2a & b_i^\dagger b_i\, b_j^\dagger b_j\, b_i\, b_j &\longrightarrow 4na \\ b_i^\dagger b_j^\dagger b_i^\dagger b_i\, b_j^\dagger b_j &\longrightarrow 4na & b_i\, b_j\, b_i^\dagger b_i\, b_j^\dagger b_j &\longrightarrow 4na + 2a \end{aligned}$$

In total:

$$\sum = -18\,(n+a)^2 - 8\,(n+a) - 1$$

B.1.2.2. Prefactor of $b_i^\dagger b_j^\dagger$

- $-2(\hat{n}_i\hat{n}_j^2 + \hat{n}_i^2\hat{n}_j)$:

$$b_i^\dagger b_i\, b_j^\dagger b_j\, b_j^\dagger b_j \longrightarrow 4na + a \qquad b_i^\dagger b_i\, b_i^\dagger b_i\, b_j^\dagger b_j \longrightarrow 4na + a$$

- $-\frac{1}{2}(\hat{I}_0\,\hat{I}'_0 + \hat{I}_0\,\hat{I}'_0)$:

$$b_i^\dagger b_j^\dagger b_i^\dagger b_i^\dagger b_i\, b_j^\dagger \longrightarrow 12na \qquad b_i^\dagger b_i^\dagger b_i\, b_j^\dagger b_i^\dagger b_j^\dagger \longrightarrow 12na + 4a$$
$$b_i^\dagger b_j^\dagger b_i\, b_j^\dagger b_j\, b_j \longrightarrow 4na \qquad b_i^\dagger b_i^\dagger b_i\, b_j^\dagger b_i\, b_j \longrightarrow 4na$$
$$b_i\, b_j\, b_i^\dagger b_i^\dagger b_i\, b_j^\dagger \longrightarrow 4na + 2a \qquad b_i\, b_j^\dagger b_j\, b_j\, b_i^\dagger b_j^\dagger \longrightarrow 4na + 2a$$
$$b_i\, b_j\, b_i\, b_j^\dagger b_j\, b_j \longrightarrow 0 \qquad b_i\, b_j^\dagger b_j\, b_j\, b_i\, b_j \longrightarrow 0$$

- $-\frac{1}{2}[(\hat{n}_i + \hat{n}_j)\hat{I}'_0 + \hat{I}'_0(\hat{n}_i + \hat{n}_j)]$:

$$b_i^\dagger b_i\, b_i^\dagger b_i^\dagger b_i\, b_j^\dagger \longrightarrow 6n^2 + 4n \qquad b_i^\dagger b_i^\dagger b_i\, b_j^\dagger b_i^\dagger b_i \longrightarrow 6n^2 + 2n$$
$$b_i^\dagger b_i\, b_i\, b_j^\dagger b_j\, b_j \longrightarrow 2a^2 \qquad b_i^\dagger b_i^\dagger b_i\, b_j^\dagger b_j^\dagger b_j \longrightarrow 4n^2 + 4a^2$$
$$b_j^\dagger b_j\, b_i^\dagger b_i^\dagger b_i\, b_j^\dagger \longrightarrow 4n^2 + 4a^2 + 2n \qquad b_i\, b_j^\dagger b_j\, b_j\, b_i^\dagger b_i \longrightarrow 2a^2$$
$$b_j^\dagger b_j\, b_i\, b_j^\dagger b_j\, b_j \longrightarrow 0 \qquad b_i\, b_j^\dagger b_j\, b_j\, b_j^\dagger b_j \longrightarrow 0$$

- $-\hat{n}_i\hat{n}_j\hat{I}_0 - \hat{I}_0\hat{n}_i\hat{n}_j$:

$$b_i^\dagger b_i\, b_j^\dagger b_j\, b_i^\dagger b_j^\dagger \longrightarrow 4n^2 + 4a^2 + 4n + 1 \qquad b_i^\dagger b_i\, b_j^\dagger b_j\, b_i\, b_j \longrightarrow 2a^2$$
$$b_i^\dagger b_j^\dagger b_i^\dagger b_i\, b_j^\dagger b_j \longrightarrow 4n^2 + 4a^2 \qquad b_i\, b_j\, b_i^\dagger b_i\, b_j^\dagger b_j \longrightarrow 2a^2$$

In total:

$$\sum = -18\,(n+a)^2 - 8\,(n+a) - 1$$

B.1.3. $\mathcal{O}(S^0)$

B.1.3.1. Prefactor of $\hat{n}_i$

- $\hat{n}_i^2\hat{n}_j^2$:

$$b_i^\dagger b_i\, b_i^\dagger b_i\, b_j^\dagger b_j\, b_j^\dagger b_j \longrightarrow 8n^3 + 6n^2 + 16na^2 + 4a^2 + n$$

- $\frac{1}{4}\hat{I}'^2_0$:

$$b_i^\dagger b_i^\dagger b_i\, b_j^\dagger b_i^\dagger b_i^\dagger b_i\, b_j^\dagger \longrightarrow 48na^2 + 12a^2$$
$$b_i^\dagger b_i^\dagger b_i\, b_j^\dagger b_i\, b_j^\dagger b_j\, b_j \longrightarrow 8n^3 + 16na^2$$
$$b_i\, b_j^\dagger b_j\, b_j\, b_i^\dagger b_i^\dagger b_i\, b_j^\dagger \longrightarrow 8n^3 + 16na^2 + 12n^2 + 8a^2 + 4n$$
$$b_i\, b_j^\dagger b_j\, b_j\, b_i\, b_j^\dagger b_j\, b_j \longrightarrow 0$$

- $\frac{1}{2}(\hat{n}_i \hat{n}_j \hat{I}'_0 + \hat{I}'_0 \hat{n}_i \hat{n}_j)$:

$$
\begin{aligned}
b_i^\dagger b_i\, b_j^\dagger b_j\, b_i^\dagger b_i^\dagger b_i\, b_j^\dagger &\longrightarrow 12a^3 + 24n^2a + 20na + 4a \\
b_i^\dagger b_i\, b_j^\dagger b_j\, b_i\, b_j^\dagger b_j\, b_j &\longrightarrow 12n^2a + 4na \\
b_i^\dagger b_i^\dagger b_i\, b_j^\dagger b_i^\dagger b_i\, b_j^\dagger b_j &\longrightarrow 12a^3 + 24n^2a + 4na \\
b_i\, b_j^\dagger b_j\, b_j\, b_i^\dagger b_i\, b_j^\dagger b_j &\longrightarrow 12n^2a + 8na
\end{aligned}
$$

In total:

$$\sum = 12\,(a+n)^3 + 9\,(n+a)^2 + 2\,(n+a)$$

B.1.3.2. Prefactor of $b_i^\dagger b_j^\dagger$

- $\hat{n}_i^2 \hat{n}_j^2$:

$$b_i^\dagger b_i\, b_i^\dagger b_i\, b_j^\dagger b_j\, b_j^\dagger b_j \longrightarrow 8a^3 + 16n^2a + 8na + a$$

- $\frac{1}{4}\hat{I}'^2_0$:

$$
\begin{aligned}
b_i^\dagger b_i^\dagger b_i\, b_j^\dagger b_i^\dagger b_i\, b_j^\dagger &\longrightarrow 48n^2a + 24na \\
b_i^\dagger b_i^\dagger b_i\, b_j^\dagger b_i\, b_j^\dagger b_j\, b_j &\longrightarrow 16n^2a + 8a^3 \\
b_i\, b_j^\dagger b_j\, b_j\, b_i^\dagger b_i^\dagger b_i\, b_j^\dagger &\longrightarrow 8a^3 + 16n^2a + 16an + 4a \\
b_i\, b_j^\dagger b_j\, b_j\, b_i\, b_j^\dagger b_j\, b_j &\longrightarrow 0
\end{aligned}
$$

- $\frac{1}{2}(\hat{n}_i \hat{n}_j \hat{I}'_0 + \hat{I}'_0 \hat{n}_i \hat{n}_j)$:

$$
\begin{aligned}
b_i^\dagger b_i\, b_j^\dagger b_j\, b_i^\dagger b_i^\dagger b_i\, b_j^\dagger &\longrightarrow 12n^3 + 24na^2 + 14n^2 + 8a^2 + 4n \\
b_i^\dagger b_i\, b_j^\dagger b_j\, b_i\, b_j^\dagger b_j\, b_j &\longrightarrow 12na^2 + 2a^2 \\
b_i^\dagger b_i^\dagger b_i\, b_j^\dagger b_i^\dagger b_i\, b_j^\dagger b_j &\longrightarrow 12n^3 + 24na^2 + 4n^2 + 4a^2 \\
b_i\, b_j^\dagger b_j\, b_j\, b_i^\dagger b_i\, b_j^\dagger b_j &\longrightarrow 12na^2 + 4a^2
\end{aligned}
$$

In total:

$$\sum = 12\,(a+n)^3 + 9\,(n+a)^2 + 2\,(n+a)$$

B.2. Ferromagnetic bonds

The non-vanishing expectation values are

$$n := \left\langle b_i^\dagger b_i \right\rangle = \left\langle b_j^\dagger b_j \right\rangle \tag{B.3a}$$

$$f := \left\langle b_i^\dagger b_j \right\rangle = \left\langle b_j^\dagger b_i \right\rangle . \tag{B.3b}$$

They are all assumed to be real. The operators

$$\hat{F}_0 := b_i^\dagger b_j + b_j^\dagger b_i \tag{B.4a}$$

$$\hat{F}_0' := b_i^\dagger \hat{n}_i b_j + b_j^\dagger \hat{n}_j b_i . \tag{B.4b}$$

are introduced for convenience.

The prefactors of $\hat{n}_j$ and $b_j^\dagger b_i$ are identical to the prefactors of $\hat{n}_i$ and $b_i^\dagger b_j$, respectively.

B.2.1. $\mathcal{O}(S^2)$

B.2.1.1. Prefactor of $\hat{n}_i$

- $\hat{n}_i^2 + \hat{n}_j^2 + 4\hat{n}_i\hat{n}_j$:

$$b_i^\dagger b_i\, b_i^\dagger b_i \longrightarrow 4n + 1 \qquad b_i^\dagger b_i\, b_j^\dagger b_j \longrightarrow n$$

- $\hat{F}_0^2$:

$$b_i^\dagger b_j\, b_i^\dagger b_j \longrightarrow 0 \qquad b_i^\dagger b_j\, b_j^\dagger b_i \longrightarrow n + 1$$
$$b_j^\dagger b_i\, b_j^\dagger b_i \longrightarrow 0 \qquad b_j^\dagger b_i\, b_i^\dagger b_j \longrightarrow n$$

- $-\hat{F}_0'$:

$$b_i^\dagger b_i^\dagger b_i\, b_j \longrightarrow 2f \qquad b_j^\dagger b_j^\dagger b_j\, b_i \longrightarrow 0$$

- $-\hat{F}_0(\hat{n}_i + \hat{n}_j) - (\hat{n}_i + \hat{n}_j)\hat{F}_0$:

$$b_i^\dagger b_j\, b_i^\dagger b_i \longrightarrow 2f \qquad b_i^\dagger b_i\, b_j^\dagger b_i \longrightarrow 2f$$
$$b_i^\dagger b_j\, b_j^\dagger b_j \longrightarrow 0 \qquad b_i^\dagger b_i\, b_i^\dagger b_j \longrightarrow 2f$$
$$b_j^\dagger b_i\, b_i^\dagger b_i \longrightarrow 2f \qquad b_j^\dagger b_j\, b_j^\dagger b_i \longrightarrow 0$$
$$b_j^\dagger b_i\, b_j^\dagger b_j \longrightarrow 0 \qquad b_j^\dagger b_j\, b_i^\dagger b_j \longrightarrow 0$$

In total:

$$\sum = 10\,(n-f) + 2$$

B.2.1.2. Prefactor of $b_i^\dagger b_j$

- $\hat{n}_i^2 + \hat{n}_j^2 + 4\hat{n}_i\hat{n}_j$:

$$b_i^\dagger b_i\, b_i^\dagger b_i \longrightarrow 0 \qquad b_i^\dagger b_i\, b_j^\dagger b_j \longrightarrow f$$

- $\hat{F}_0^2$:

$$b_i^\dagger b_j\, b_i^\dagger b_j \longrightarrow 4f \qquad b_i^\dagger b_j\, b_j^\dagger b_i \longrightarrow f$$
$$b_j^\dagger b_i\, b_j^\dagger b_i \longrightarrow 0 \qquad b_j^\dagger b_i\, b_i^\dagger b_j \longrightarrow f$$

- $-\hat{F}_0'$:

$$b_i^\dagger b_i^\dagger b_i\, b_j \longrightarrow 2n \qquad b_j^\dagger b_j^\dagger b_j\, b_i \longrightarrow 0$$

- $-\hat{F}_0(\hat{n}_i + \hat{n}_j) - (\hat{n}_i + \hat{n}_j)\hat{F}_0$:

$$b_i^\dagger b_j\, b_i^\dagger b_i \longrightarrow 2n \qquad b_i^\dagger b_i\, b_j^\dagger b_i \longrightarrow 0$$
$$b_i^\dagger b_j\, b_j^\dagger b_j \longrightarrow 2n+1 \qquad b_i^\dagger b_i\, b_i^\dagger b_j \longrightarrow 2n+1$$
$$b_j^\dagger b_i\, b_i^\dagger b_i \longrightarrow 0 \qquad b_j^\dagger b_j\, b_j^\dagger b_i \longrightarrow 0$$
$$b_j^\dagger b_i\, b_j^\dagger b_j \longrightarrow 0 \qquad b_j^\dagger b_j\, b_i^\dagger b_j \longrightarrow 2n$$

In total:

$$\sum = -10\,(n-f) - 2$$

$\rightsquigarrow 10\,(n-f) + 2$ for $-b_i^\dagger b_j$.

B.2.2. $\mathcal{O}(S)$

B.2.2.1. Prefactor of $\hat{n}_i$

- $-2(\hat{n}_i\hat{n}_j^2 + \hat{n}_i^2\hat{n}_j)$:

$$b_i^\dagger b_i\, b_j^\dagger b_j\, b_j^\dagger b_j \longrightarrow 2n^2 + n \qquad b_i^\dagger b_i\, b_i^\dagger b_i\, b_j^\dagger b_j \longrightarrow 4n^2 + 4f^2 + n$$

- $-\frac{1}{2}(\hat{F}_0\hat{F}_0' + \hat{F}_0'\hat{F}_0)$:

$$b_i^\dagger b_j\, b_i^\dagger b_i^\dagger b_i\, b_j \longrightarrow 6f^2 \qquad b_i^\dagger b_i^\dagger b_i\, b_j\, b_i^\dagger b_j \longrightarrow 6f^2$$
$$b_i^\dagger b_j\, b_j^\dagger b_j^\dagger b_j\, b_i \longrightarrow 2n^2 + 2n \qquad b_i^\dagger b_i^\dagger b_i\, b_j\, b_j^\dagger b_i \longrightarrow 4n^2 + 4f^2 + 4n$$
$$b_j^\dagger b_i\, b_i^\dagger b_i^\dagger b_i\, b_j \longrightarrow 2n^2 \qquad b_j^\dagger b_j^\dagger b_j\, b_i\, b_i^\dagger b_j \longrightarrow 2n^2$$
$$b_j^\dagger b_i\, b_j^\dagger b_j^\dagger b_j\, b_i \longrightarrow 0 \qquad b_j^\dagger b_j^\dagger b_j\, b_i\, b_j^\dagger b_i \longrightarrow 0$$

- $\hat{n}_i\hat{n}_j\hat{F}_0 + \hat{F}_0\hat{n}_i\hat{n}_j$:

$$b_i^\dagger b_i\, b_j^\dagger b_j\, b_i^\dagger b_j \longrightarrow 4nf \qquad b_i^\dagger b_j\, b_i^\dagger b_i\, b_j^\dagger b_j \longrightarrow 4nf + 2f$$
$$b_i^\dagger b_i\, b_j^\dagger b_j\, b_j^\dagger b_i \longrightarrow 4nf + 2f \qquad b_j^\dagger b_i\, b_i^\dagger b_i\, b_j^\dagger b_j \longrightarrow 4nf$$

- $\frac{1}{2}[\hat{F}_0'(\hat{n}_i + \hat{n}_j) + (\hat{n}_i + \hat{n}_j)\hat{F}_0']$:

$$b_i^\dagger b_i^\dagger b_i\, b_j\, b_i^\dagger b_i \longrightarrow 12nf + 2f \qquad b_i^\dagger b_i\, b_i^\dagger b_i^\dagger b_i\, b_j \longrightarrow 12nf + 4f$$
$$b_j^\dagger b_j^\dagger b_j\, b_i\, b_i^\dagger b_i \longrightarrow 4nf \qquad b_i^\dagger b_i\, b_j^\dagger b_j^\dagger b_j\, b_i \longrightarrow 4nf$$
$$b_i^\dagger b_i^\dagger b_i\, b_j\, b_j^\dagger b_j \longrightarrow 4nf + 2f \qquad b_j^\dagger b_i\, b_i^\dagger b_i^\dagger b_i\, b_j \longrightarrow 4nf$$
$$b_j^\dagger b_j^\dagger b_j\, b_i\, b_j^\dagger b_j \longrightarrow 0 \qquad b_j^\dagger b_j\, b_j^\dagger b_j^\dagger b_j\, b_i \longrightarrow 0$$

In total:

$$\sum = -18\,(n-f)^2 - 8\,(n-f)$$

B.2.2.2. Prefactor of $b_i^\dagger b_j$

- $-2(\hat{n}_i\hat{n}_j^2 + \hat{n}_i^2\hat{n}_j)$:

$$b_i^\dagger b_i\, b_j^\dagger b_j\, b_j^\dagger b_j \longrightarrow 4nf + f \qquad b_i^\dagger b_i\, b_i^\dagger b_i\, b_j^\dagger b_j \longrightarrow 4nf + f$$

- $-\frac{1}{2}(\hat{F}_0\hat{F}_0' + \hat{F}_0'\hat{F}_0)$:

$$b_i^\dagger b_j\, b_i^\dagger b_i^\dagger b_i\, b_j \longrightarrow 12nf \qquad b_i^\dagger b_i^\dagger b_i\, b_j\, b_i^\dagger b_j \longrightarrow 12nf + 4f$$
$$b_i^\dagger b_j\, b_j^\dagger b_j^\dagger b_j\, b_i \longrightarrow 4nf + 2f \qquad b_i^\dagger b_i^\dagger b_i\, b_j\, b_j^\dagger b_i \longrightarrow 4nf$$
$$b_j^\dagger b_i\, b_i^\dagger b_i^\dagger b_i\, b_j \longrightarrow 4nf + 2f \qquad b_j^\dagger b_j^\dagger b_j\, b_i\, b_i^\dagger b_j \longrightarrow 4nf$$
$$b_j^\dagger b_i\, b_j^\dagger b_j^\dagger b_j\, b_i \longrightarrow 0 \qquad b_j^\dagger b_j^\dagger b_j\, b_i\, b_j^\dagger b_i \longrightarrow 0$$

- $\hat{n}_i\hat{n}_j\hat{F}_0 + \hat{F}_0\hat{n}_i\hat{n}_j$:

$$b_i^\dagger b_i\, b_j^\dagger b_j\, b_i^\dagger b_j \longrightarrow 4n^2 + 4f^2 + 2n \qquad b_i^\dagger b_j\, b_i^\dagger b_i\, b_j^\dagger b_j \longrightarrow 4n^2 + 4f^2 + 2n$$
$$b_i^\dagger b_i\, b_j^\dagger b_j\, b_j^\dagger b_i \longrightarrow 2f^2 \qquad b_j^\dagger b_i\, b_i^\dagger b_i\, b_j^\dagger b_j \longrightarrow 2f^2$$

- $\frac{1}{2}[\hat{F}_0'(\hat{n}_i + \hat{n}_j) + (\hat{n}_i + \hat{n}_j)\hat{F}_0']$:

$$b_i^\dagger b_i^\dagger b_i\, b_j\, b_i^\dagger b_i \longrightarrow 6n^2 + 2n \qquad b_i^\dagger b_i\, b_i^\dagger b_i^\dagger b_i\, b_j \longrightarrow 6n^2 + 4n$$
$$b_j^\dagger b_j^\dagger b_j\, b_i\, b_i^\dagger b_i \longrightarrow 2f^2 \qquad b_i^\dagger b_i\, b_j^\dagger b_j^\dagger b_j\, b_i \longrightarrow 2f^2$$
$$b_i^\dagger b_i^\dagger b_i\, b_j\, b_j^\dagger b_j \longrightarrow 4n^2 + 4f^2 + 2n \qquad b_j^\dagger b_j\, b_i^\dagger b_i^\dagger b_i\, b_j \longrightarrow 4n^2 + 4f^2$$
$$b_j^\dagger b_j^\dagger b_j\, b_i\, b_j^\dagger b_j \longrightarrow 0 \qquad b_j^\dagger b_j\, b_j^\dagger b_j^\dagger b_j\, b_i \longrightarrow 0$$

In total:

$$\sum = 18\,(n-f)^2 + 8\,(n-f)$$

$\rightsquigarrow 10\,(n-f) + 2$ for $-b_i^\dagger b_j$.

B.2.3. $\mathcal{O}(S^0)$

B.2.3.1. Prefactor of $\hat{n}_i$

- $\hat{n}_i^2\hat{n}_j^2$:

$$b_i^\dagger b_i\, b_i^\dagger b_i\, b_j^\dagger b_j\, b_j^\dagger b_j \longrightarrow 8n^3 + 16nf^2 + 6n^2 + 4f^2 + n$$

- $\frac{1}{4}\hat{F}_0'^2$:

$$b_i^\dagger b_i^\dagger b_i\, b_j\, b_i^\dagger b_i\, b_i\, b_j \longrightarrow 48nf^2 + 12f^2$$
$$b_i^\dagger b_i^\dagger b_i\, b_j\, b_j^\dagger b_j^\dagger b_j\, b_i \longrightarrow 8n^3 + 16nf^2 + 8n^2 + 8f^2$$
$$b_j^\dagger b_j^\dagger b_j\, b_i\, b_i^\dagger b_i^\dagger b_i\, b_j \longrightarrow 8n^3 + 4n^2 + 16nf^2$$
$$b_j^\dagger b_j^\dagger b_j\, b_i\, b_j^\dagger b_j^\dagger b_j\, b_i \longrightarrow 0$$

- $-\frac{1}{2}(\hat{n}_i\,\hat{n}_j\,\hat{F}_0' + \hat{F}_0'\hat{n}_i\,\hat{n}_j)$:

$$b_i^\dagger b_i\, b_j^\dagger b_j\, b_i^\dagger b_i^\dagger b_i\, b_j \longrightarrow 12f^3 + 24n^2f + 8nf$$
$$b_i^\dagger b_i\, b_j^\dagger b_j\, b_j^\dagger b_j^\dagger b_j\, b_i \longrightarrow 12n^2f + 8nf$$
$$b_i^\dagger b_i^\dagger b_i\, b_j\, b_i^\dagger b_i\, b_j^\dagger b_j \longrightarrow 12f^3 + 24n^2f + 16nf + 2f$$
$$b_j^\dagger b_j^\dagger b_j\, b_i\, b_i^\dagger b_i\, b_j^\dagger b_j \longrightarrow 12n^2f + 4nf$$

In total:

$$\sum = 12\left(n-f\right)^3 + 9\left(n-f\right)^2 + \left(n-f\right)$$

B.2.3.2. Prefactor of $b_i^\dagger b_j$

- $\hat{n}_i^2 \hat{n}_j^2$:

$$b_i^\dagger b_i\, b_i^\dagger b_i\, b_j^\dagger b_j\, b_j^\dagger b_j \longrightarrow 8f^3 + 16n^2 f + 8nf + f$$

- $\frac{1}{4}\hat{F}_0'^2$:

$$\begin{aligned}
b_i^\dagger b_i^\dagger b_i\, b_j\, b_i^\dagger b_i^\dagger b_i\, b_j &\longrightarrow 48n^2 f + 24nf \\
b_i^\dagger b_i^\dagger b_i\, b_j\, b_j^\dagger b_j^\dagger b_j\, b_i &\longrightarrow 8f^3 + 16n^2 f + 8nf \\
b_j^\dagger b_j^\dagger b_j\, b_i\, b_i^\dagger b_i^\dagger b_i\, b_j &\longrightarrow 8f^3 + 16n^2 f + 8nf \\
b_j^\dagger b_j^\dagger b_j\, b_i\, b_j^\dagger b_j^\dagger b_j\, b_i &\longrightarrow 0
\end{aligned}$$

- $-\frac{1}{2}(\hat{n}_i\,\hat{n}_j\,\hat{F}_0' + \hat{F}_0'\hat{n}_i\,\hat{n}_j\,)$:

$$\begin{aligned}
b_i^\dagger b_i\, b_j^\dagger b_j\, b_i^\dagger b_i^\dagger b_i\, b_j &\longrightarrow 12n^3 + 24nf^2 + 8n^2 + 8f^2 \\
b_i^\dagger b_i\, b_j^\dagger b_j\, b_j^\dagger b_j^\dagger b_j\, b_i &\longrightarrow 12nf^2 + 4f^2 \\
b_i^\dagger b_i^\dagger b_i\, b_j\, b_i^\dagger b_i\, b_j^\dagger b_j &\longrightarrow 12n^3 + 24nf^2 + 10n^2 + 4f^2 + 2n \\
b_j^\dagger b_j^\dagger b_j\, b_i\, b_i^\dagger b_i\, b_j^\dagger b_j &\longrightarrow 12nf^2 + 2f^2
\end{aligned}$$

In total:

$$\sum = -12\left(n-f\right)^3 - 9\left(n-f\right)^2 - \left(n-f\right)$$

$\rightsquigarrow 12\left(n-f\right)^3 + 9\left(n-f\right)^2 + \left(n-f\right)$ for $-b_i^\dagger b_j$.

C. Density of states

This section introduces a *density of states*

$$\begin{aligned} \varrho\left(\gamma\right) &= \frac{1}{N}\sum_{k}\delta\left(\gamma-\gamma_k\right) \\ &= \frac{1}{\left(2\pi\right)^2}\iint\limits_{\mathrm{BZ}}\mathrm{d}^2k\;\delta\left(\gamma-\gamma_k\right), \end{aligned} \tag{C.1}$$

so that the two dimensional integration over the Brillouin zone can be reduced to a one dimensional integration. In this appendix, the reciprocal lattice vectors are denoted in units of $1/$(lattice constant).

In Chapter 4, it was shown that the spin wave dispersion for the two dimensional square lattice can be interpreted as $\omega_k = \omega(\gamma_k)$ with $\gamma_k = 1/2(\cos k_a + \cos k_b) \in [-1,1]$. Thus, it is possible to write summations/integrations over the Brillouin zone in terms of a density of states

$$\sum_{k\in\,\mathrm{BZ}} F\left(\omega_k\right) \longrightarrow 2\int\limits_0^1 \mathrm{d}\gamma\;\varrho\left(\gamma\right) F\left(\omega\left(\gamma\right)\right) \tag{C.2a}$$

$$\frac{1}{\left(2\pi\right)^2}\iint\limits_{\mathrm{BZ}}\mathrm{d}^2k\;F\left(\omega_k\right) \longrightarrow 2\int\limits_0^1 \mathrm{d}\gamma\;\varrho\left(\gamma\right) F\left(\omega\left(\gamma\right)\right), \tag{C.2b}$$

where the factor 2 is a consequence of the symmetry of ω_k and ϱ in γ.

We now derive the density of states for a two dimensional square lattice. The factor γ_k with $k_{a,b} \in [-\pi,\pi]$ (BZ) is rewritten as

$$\begin{aligned} \gamma_k &= \frac{1}{2}\left(\cos k_a + \cos k_b\right) \\ &= \cos\left(\frac{k_a+k_b}{2}\right)\cos\left(\frac{k_a-k_b}{2}\right) \\ &= \cos k_1 \cos k_2 \end{aligned} \tag{C.3}$$

with $k_{1,2} \in [-\pi, \pi]$. Therewith, the density of states reads

$$\begin{aligned}
\varrho(\gamma) &= \frac{1}{\pi^2} \int_0^\pi \mathrm{d}k_1 \int_0^\pi \mathrm{d}k_2 \, \delta(\gamma - \cos k_1 \cos k_2) \\
&= \frac{1}{\pi^2} \int_0^\pi \mathrm{d}k_1 \frac{1}{\cos k_1} \int_0^\pi \mathrm{d}k_2 \, \delta\left(\frac{\gamma}{\cos k_1} - \cos k_2\right) \\
&= \frac{1}{\pi^2} \int_0^\pi \mathrm{d}k_1 \frac{1}{\cos k_1} \int_{-1}^1 \mathrm{d}\beta \, \frac{1}{\sqrt{1-\beta^2}} \, \delta\left(\frac{\gamma}{\cos k_1} - \beta\right) \\
&= \frac{1}{\pi^2} \int_{\arccos -\gamma}^{\arccos \gamma} \mathrm{d}k_1 \frac{1}{\cos k_1} \sqrt{1 - \left(\frac{\gamma}{\cos k_1}\right)^2}^{-1},
\end{aligned}$$

where we substituted $\beta = \cos k_2$ and swapped the integration limits in step 3. The limits of the outer integration have to be adjusted due to the Dirac delta. Furthermore, we use the symmetry of $\arccos x$ and substitute

$$\begin{aligned}
\alpha &= \frac{1}{\sqrt{1-\gamma^2}} \sin k_1 = \frac{\sqrt{1-\cos^2 k_1}}{\sqrt{1-\gamma^2}} \\
\Leftrightarrow \cos^2 k_1 &= 1 - \left(1-\gamma^2\right)\alpha^2,
\end{aligned}$$

where $\alpha \in [0,1]$. We now have

$$\begin{aligned}
\varrho(\gamma) &= \frac{2}{\pi^2} \int_0^1 \mathrm{d}\alpha \, \frac{1}{\sqrt{1-\left(1-\gamma^2\right)\alpha^2}} \underbrace{\frac{\sqrt{1-\gamma^2}}{\sqrt{1-\left(1-\gamma^2\right)\alpha^2-\gamma^2}}}_{\sqrt{\left(1-\gamma^2\right)\left(1-\alpha^2\right)}} \\
&= \frac{2}{\pi^2} \int_0^1 \mathrm{d}\alpha \, \frac{1}{\sqrt{1-\alpha^2}} \frac{1}{\sqrt{1-\left(1-\gamma^2\right)\alpha^2}}. \qquad \text{(C.4)}
\end{aligned}$$

Introducing the *complete elliptic integral of the first kind*

$$K(x) := \int_0^1 \mathrm{d}\alpha \, \frac{1}{\sqrt{1-\alpha^2}} \frac{1}{\sqrt{1-x^2\alpha^2}}, \qquad \text{(MAPLE definition)} \qquad \text{(C.5)}$$

the final result for the density of states of the two dimensional square lattice is

$$\varrho(\gamma) = \frac{2}{\pi^2} K\left(\sqrt{1-\gamma^2}\right). \qquad \text{(C.6)}$$

D. Details for evaluating the integrals

In this appendix, we describe how the domain of integration in the two and three dimensional collinear phase is decomposed. Furthermore, we present how the divergences in the integrand of the staggered magnetization and of the self-consistency equations are treated. This procedure is also applicable for the model with biquadratic exchange discussed in Chapter 6.
For brevity, the reciprocal lattice vectors are still denoted in units of π/(lattice constant).

D.1. 2D collinear phase: $x = 0$

The two dimensional collinear phase is reproduced for $x = 0$. The integration is reduced to k_a and k_b and the self-consistency equations are given by

$$\begin{aligned}\alpha_1 = \alpha_c = \beta &= \frac{2}{\pi^2} \int_0^{1/2} \mathrm{d}k_a \int_0^{1/2} \mathrm{d}k_b \, \frac{1}{\sqrt{1 - \left(\cos k_a \cdot \cos k_b\right)^2}} - \frac{1}{2} \\ &= \frac{2}{\pi^2} \int_0^{1/2} \mathrm{d}k_a \int_0^{1/2} \mathrm{d}k_b \, f\left(k_a, k_b\right) - \frac{1}{2}\end{aligned} \tag{D.1a}$$

$$\alpha_2 = \frac{2}{\pi^2} \int_0^{1/2} \mathrm{d}k_a \int_0^{1/2} \mathrm{d}k_b \, \sqrt{1 - \left(\cos k_a \cdot \cos k_b\right)^2} - \frac{1}{2}, \tag{D.1b}$$

where we have used the symmetry of $\cos u$ about $u = 0$. The k-dependence is only manifested in the product $(\cos k_a \cdot \cos k_b)^2$. Thus, the integration of the reciprocal lattice vectors is reduced to $k_i \in [0, 0.5]$. The integrand in the self-consistency equation for α_2 does not diverge at all and is uncritical. The integrand $f(k_a, k_b)$ of the self-consistency equations for α_1, α_c and β also appears in the staggered magnetization

$$\begin{aligned}m_{\mathrm{st}} &= S + \frac{1}{2} - \frac{2}{\pi^2} \int_0^{1/2} \mathrm{d}k_a \int_0^{1/2} \mathrm{d}k_b \, \frac{1}{\sqrt{1 - \left(\cos k_a \cdot \cos k_b\right)^2}} \\ &= S + \frac{1}{2} - \frac{2}{\pi^2} \int_0^{1/2} \mathrm{d}k_a \int_0^{1/2} \mathrm{d}k_b \, f\left(k_a, k_b\right)\end{aligned} \tag{D.2}$$

and diverges at $k = (0,0)$. To eliminate the divergence in $f(k_a, k_b)$, we expand the integrand for small values of k:

$$f\left(k_a, k_b\right) \longrightarrow \tilde{f}\left(k_a, k_b\right) \approx \frac{1}{\sqrt{k_a^2 + k_b^2}}. \tag{D.3}$$

This expression can be integrated analytically. For a rectangle with side length $\tilde{k}_a$ and $\tilde{k}_b$, one obtains the result

$$\begin{aligned} \tilde{F}\left(\tilde{k}_a, \tilde{k}_b\right) &= \int_0^{\tilde{k}_a} \mathrm{d}k_a \int_0^{\tilde{k}_b} \mathrm{k}_b \, \tilde{f}\left(k_a, k_b\right) \\ &= \tilde{k}_a \operatorname{arsinh} \frac{\tilde{k}_b}{\tilde{k}_a} + \tilde{k}_b \operatorname{arsinh} \frac{\tilde{k}_a}{\tilde{k}_b}. \end{aligned} \tag{D.4}$$

Typically, we choose $\tilde{k}_a = \tilde{k}_b = \Delta k = 10^{-3}$, which results in $F\left(\Delta k, \Delta k\right) \approx 0.0017627$.

In total, the domain of integration in the self-consistency equations for α_1, α_c and β and in m_{st} is split up in three parts (see Fig. D.1):

$$\begin{aligned} I &= \int_0^{1/2} \mathrm{d}k_a \int_0^{1/2} \mathrm{d}k_b \, f\left(k_a, k_b\right) \\ &= \underbrace{F\left(\Delta k, \Delta k\right)}_{\mathrm{I}} + \underbrace{\int_{\Delta k}^{1/2} \mathrm{d}k_a \int_0^{\Delta k} \mathrm{d}k_b \, f\left(k_a, k_b\right)}_{\mathrm{II}} + \underbrace{\int_0^{1/2} \mathrm{d}k_a \int_{\Delta k}^{1/2} \mathrm{d}k_b \, f\left(k_a, k_b\right)}_{\mathrm{III}}. \end{aligned} \tag{D.5}$$

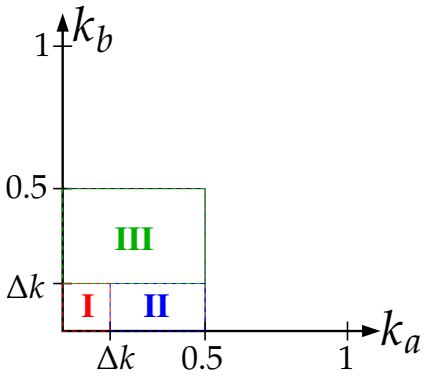

Fig. D.1.: Decomposition of the domain of integration for $x = 0$ of the integrals appearing in the self-consistency equations for α_1, α_c, β and in the staggered magnetization m_{st}.

D.2. 3D collinear phase: $x \neq 0$

No special treatment for the self-consistency equations is required in the three dimensional collinear phase because the numerators of the integrands always vanish at the gapless Goldstone modes located at $k = (0,0,0)$ and $k = (1,0,1)$. However, a divergence is still present in the integrand of the staggered magnetization (5.30)

$$\begin{aligned} m_{\mathrm{st}} &= S + \frac{1}{2} - \frac{1}{\pi^3} \int_0^1 \mathrm{d}k_a \int_0^1 \mathrm{d}k_b \int_0^{1-k_a} \mathrm{d}k_c \, \frac{\bar{A}_k}{\sqrt{\bar{A}_k^2 - \bar{B}_k^2}} \\ &= S + \frac{1}{2} - \frac{1}{\pi^3} \int_0^1 \mathrm{d}k_a \int_0^1 \mathrm{d}k_b \int_0^{1-k_a} \mathrm{d}k_c \, g\left(k_a, k_b, k_c\right), \end{aligned} \tag{D.6}$$

where the symmetry of $\cos u$ about $u = 0$ and the point symmetry about $(0.5, k_b, 0.5)$ in the k_a-k_c-plane have already been taken into account. $\bar{A}_k$ and $\bar{B}_k$ are defined in (5.20). As before, the idea is to decompose the domain of integration and to expand the integrand of m_{st} for small momenta in a cube with side length Δk. In total, the domain of integration has to be split into five parts (see Fig. D.2). Thus, the integral in the staggered magnetization (D.6) reads

$$\begin{aligned} \int_0^1 \mathrm{d}k_a \int_0^1 \mathrm{d}k_b \int_0^{1-k_a} \mathrm{d}k_c \, g\left(k_a, k_b, k_c\right) = {} & \underbrace{\int_0^{\Delta k} \mathrm{d}k_a \int_0^{\Delta k} \mathrm{d}k_b \int_0^{\Delta k} \mathrm{d}k_c \, \tilde{g}\left(k_a, k_b, k_c\right)}_{\mathrm{I}} \\ & + \underbrace{\int_0^{1-\Delta k} \mathrm{d}k_a \int_0^1 \mathrm{d}k_b \int_{\Delta k}^{1-k_a} \mathrm{d}k_c \, g\left(k_a, k_b, k_c\right)}_{\mathrm{II}} \\ & + \underbrace{\int_{1-\Delta k}^1 \mathrm{d}k_a \int_0^1 \mathrm{d}k_b \int_0^{1-k_a} \mathrm{d}k_c \, g\left(k_a, k_b, k_c\right)}_{\mathrm{III}} \\ & + \underbrace{\int_{\Delta k}^{1-\Delta k} \mathrm{d}k_a \int_0^1 \mathrm{d}k_b \int_0^{\Delta k} \mathrm{d}k_c \, g\left(k_a, k_b, k_c\right)}_{\mathrm{IV}} \\ & + \underbrace{\int_0^{\Delta k} \mathrm{d}k_a \int_{\Delta k}^1 \mathrm{d}k_b \int_0^{\Delta k} \mathrm{d}k_c \, g\left(k_a, k_b, k_c\right)}_{\mathrm{V}}, \end{aligned} \tag{D.7}$$

where

$$\tilde{g}\left(k_a, k_b, k_c\right) \approx \frac{2J_2\left(S-\alpha_2\right)+J_1\left(S-\alpha_1\right)+J_c\left(S-\alpha_c\right)}{\sqrt{v_a^2 k_a^2+v_b^2 k_b^2+v_c^2 k_c^2}} \tag{D.8}$$

is the expansion of $g(k_a, k_b, k_c)$ for small momenta. The spin wave velocities are given in Eq. (5.22).

The expansion (D.8) still diverges at $k = (0,0,0)$, but the divergence can be eliminated by substituting all reciprocal lattice vectors with $k_i \to k_i^2$:

$$\mathrm{I} \longrightarrow \int_0^{\sqrt{\Delta k}} \mathrm{d}k_a \int_0^{\sqrt{\Delta k}} \mathrm{d}k_b \int_0^{\sqrt{\Delta k}} \mathrm{d}k_c \frac{2J_2\left(S-\alpha_2\right)+J_1\left(S-\alpha_1\right)+J_c\left(S-\alpha_c\right)}{\sqrt{v_a^2 k_a^4+v_b^2 k_b^4+v_c^2 k_c^4}} 6k_a k_b k_c. \tag{D.9}$$

The integrand is now smooth at $k = (0,0,0)$ and can be integrated numerically. The integrals II-V are uncritical.

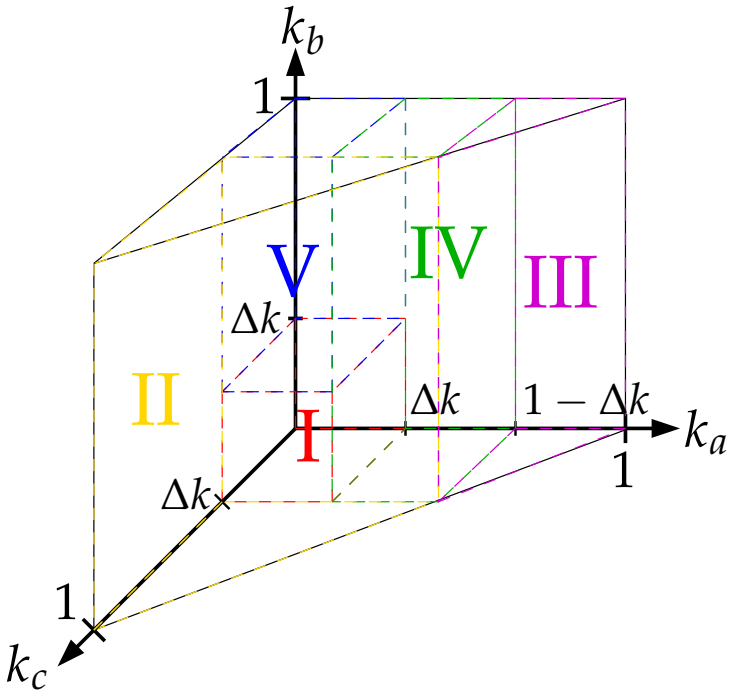

Fig. D.2.: Decomposition of the domain of integration of the integral appearing in the staggered magnetization m_{st} for $x \neq 0$.

Bibliography

[1] Y. Kamihara, T. Watanabe, M. Hirano, and H. Hosono, "Iron-based layered superconductor $LaO_{1-x}F_xFeAs$ ($x = 0.05 - 0.12$) with $T_c = 26$ K," *J. Am. Chem. Soc.* **130** (2008) 3296.

[2] Z. A. Ren, G.-C. Che, X.-L. Dong, J. Yang, W. Lu, W. Yi, X.-L. Shen, Z.-C. Li, L.-L. Sun, F. Zhou, and Z.-X. Zhao, "Superconductivity and phase diagram in iron-based arsenic-oxides $ReFeAsO_{1-\delta}$ (Re = rare-earth metal) without fluorine doping," *Europhys. Lett.* **83** (2008) 17002.

[3] J. G. Bednorz and K. A. Müller, "Possible high T_c superconductivity in the Ba-La-Cu-O system," *Z. Phys. B* **64** (1986) 189.

[4] S. Medvedev, T. M. McQueen, I. A. Troyan, T. Palasyuk, M. I. Eremets, R. J. Cava, S. Naghavi, F. Casper, V. Ksenofontov, G. Wortmann, and C. Felser, "Electronic and magnetic phase diagram of β-$Fe_{1.01}Se$ with superconductivity at 36.7 K under pressure," *Nat. Mat.* **8** (2009) 630.

[5] Y. Kamihara, H. Hiramatsu, M. Hirano, R. Kawamura, H. Yanagi, T. Kamiya, and H. Hosono, "Iron-based layered superconductor: LaOFeP," *J. Am. Chem. Soc.* **128** (2006) 10012.

[6] L. Boeri, O. V. Dolgov, and A. A. Golubov, "Is $LaFeAsO_{1-x}F_x$ an electron-phonon superconductor?," *Phys. Rev. Lett.* **101** (2008) 026403.

[7] I. I. Mazin, "Superconductivity gets an iron boost," *Nature* **464** (2010) 183.

[8] J. Zhao, D.-X. Yao, S. Li, T. Hong, Y. Chen, S. Chang, W. Ratcliff II, J. W. Lynn, H. A. Mook, G. F. Chen, J. L. Luo, N. L. Wang, E. W. Carlson, J. Hu, and P. Dai, "Low energy spin waves and magnetic interactions in $SrFe_2As_2$," *Phys. Rev. Lett.* **101** (2008) 167203.

[9] S. O. Diallo, V. P. Antropov, T. G. Perring, C. Broholm, J. J. Pulikkotil, N. Ni, S. L. Bud'ko, P. C. Canfield, A. Kreyssig, A. I. Goldman, and R. J. McQueeney, "Itinerant magnetic excitations in antiferromagnetic $CaFe_2As_2$," *Phys. Rev. Lett.* **102** (2009) 187206.

[10] J. Zhao, D. T. Adroja, D.-X. Yao, R. Bewley, S. Li, X. F. Wang, G. Wu, X. H. Chen, J. Hu, and P. Dai, "Spin waves and magnetic exchange interactions in $CaFe_2As_2$," *Nat. Phys.* **5** (2009) 555.

[11] G. S. Uhrig, M. Holt, J. Oitmaa, O. P. Sushkov, and R. R. P. Singh, "Pnictides as frustrated quantum antiferromagnets close to a quantum phase transition," *Phys. Rev. B* **79** (2009) 092416.

[12] M. Rotter, M. Tegel, and D. Johrendt, "Superconductivity at 38 K in the iron arsenide $(Ba_{1-x}K_x)Fe_2As_2$," *Phys. Rev. Lett.* **101** (2008) 107006.

[13] A. Kreyssig, M. A. Green, Y. Lee, G. D. Samolyuk, P. Zajdel, J. W. Lynn, S. L. Bud'ko, M. S. Torikachvili, N. Ni, S. Nandi, J. B. Leão, S. J. Poulton, D. N. Argyriou, B. N. Harmon, R. J. McQueeney, P. C. Canfield, and A. I. Goldman, "Pressure-induced volume-collapsed tetragonal phase of $CaFe_2As_2$ as seen via neutron scattering," *Phys. Rev. B* **78** (2008) 184517.

[14] K. Sasmal, B. Lv, B. Lorenz, A. M. Guloy, F. Chen, Y.-Y. Xue, and C.-W. Chu, "Superconducting Fe-based compounds $(A_{1-x}Sr_x)Fe_2As_2$ with A=K and Cs with transition temperatures up to 37 K," *Phys. Rev. Lett.* **101** (2008) 107007.

[15] R. J. McQueeney, S. O. Diallo, V. P. Antropov, G. D. Samolyuk, C. Broholm, N. Ni, S. Nandi, M. Yethiraj, J. L. Zarestky, J. J. Pulikkotil, A. Kreyssig, M. D. Lumsden, B. N. Harmon, P. C. Canfield, and A. I. Goldman, "Anisotropic three-dimensional magnetism in $CaFe_2As_2$," *Phys. Rev. Lett.* **101** (2008) 227205.

[16] H. Takahashi, K. Igawa, K. Arii, Y. Kamihara, M. Hirano, and H. Hosono, "Superconductivity at 43 K in an iron-based layered compound $LaO_{1-x}F_xFeAs$," *Nature* **453** (2008) 376.

[17] C. de la Cruz, Q. Huang, J. W. Lynn, J. Li, W. Ratcliff II, J. L. Zarestky, H. A. Mook, G. F. Chen, J. L. Luo, N. L. Wang, and P. Dai, "Magnetic order close to superconductivity in the iron-based layered $LaO_{1-x}F_xFeAs$ systems," *Nature* **453** (2008) 899.

[18] H.-H. Klauss, H. Luetkens, R. Klingeler, C. Hess, F. J. Litterst, M. Kraken, M. M. Korshunov, I. Eremin, S.-L. Drechsler, R. Khasanov, A. Amato, J. Hamann-Borrero, N. Leps, A. Kondrat, G. Behr, J. Werner, and B. Büchner, "Commensurate spin density wave in LaFeAsO: A local probe study," *Phys. Rev. Lett.* **101** (2008) 077005.

[19] A. I. Goldman, D. N. Argyriou, B. Ouladdiaf, T. Chatterji, A. Kreyssig, S. Nandi, N. Ni, S. L. Bud'ko, P. C. Canfield, and R. J. McQueeney, "Lattice and magnetic instabilities in $CaFe_2As_2$: A single-crystal neutron diffraction study," *Phys. Rev. B* **78** (2008) 100506.

[20] J. Zhao, W. Ratcliff II, J. W. Lynn, G. F. Chen, J. L. Luo, N. L. Wang, J. Hu, and P. Dai, "Spin and lattice structures of single-crystalline $SrFe_2As_2$," *Phys. Rev. B* **78** (2008) 140504.

[21] J. Dong, H. J. Zhang, G. Xu, Z. Li, G. Li, W. Z. Hu, D. Wu, G. F. Chen, X. Dai, J. L. Luo, Z. Fang, and N. L. Wang, "Competing orders and spin-density-wave instability in $LaO_{1-x}F_xFeAs$," *Europhys. Lett.* **83** (2008) 27006.

[22] A. N. Yaresko, G.-Q. Liu, V. N. Antonov, and O. K. Andersen, "Interplay between magnetic properties and fermi surface nesting in iron pnictides," *Phys. Rev. B* **79** (2009) 144421.

[23] W. E. Pickett, "Iron-based superconductors: Timing is crucial," *Nat. Phys.* **5** (2009) 87.

[24] A. Leithe-Jasper, W. Schnelle, C. Geibel, and H. Rosner, "Superconducting state in $SrFe_{2-x}Co_xAs_2$ by internal doping of the iron arsenide layers," *Phys. Rev. Lett.* **101** (2008) 207004.

[25] T. Park, E. Park, H. Lee, T. Klimczuk, E. D. Bauer, F. Ronning, and J. D. Thompson, "Pressure-induced superconductivity in $CaFe_2As_2$," *J. Phys. C* **20** (2008) 322204.

[26] P. L. Alireza, Y. T. C. Ko, J. Gillett, C. M. Petrone, J. M. Cole, G. G. Lonzarich, and S. E. Sebastian, "Superconductivity up to 29 K in $SrFe_2As_2$ and $BaFe_2As_2$ at high pressures," *J. Phys. C* **21** (2009) 012208.

[27] T. Yildirim, "Origin of the 150-K anomaly in LaFeAsO: Competing antiferromagnetic interactions, frustration, and a structural phase transition," *Phys. Rev. Lett.* **101** (2008) 057010.

[28] W. E. Pickett, "Electronic structure of the high-temperature oxide superconductors," *Rev. Mod. Phys.* **61** (1989) 433.

[29] A. V. Chubukov, D. V. Efremov, and I. Eremin, "Magnetism, superconductivity, and pairing symmetry in iron-based superconductors," *Phys. Rev. B* **78** (2008) 134512.

[30] W. L. Yang, A. P. Sorini, C.-C. Chen, B. Moritz, W.-S. Lee, F. Vernay, P. Olalde-Velasco, J. D. Denlinger, B. Delley, J.-H. Chu, J. G. Analytis, I. R. Fisher, Z. A. Ren, J. Yang, W. Lu, Z. X. Zhao, J. van den Brink, Z. Hussain, Z.-X. Shen, and T. P. Devereaux, "Evidence for weak electronic correlations in iron pnictides," *Phys. Rev. B* **80** (2009) 014508.

[31] K. Haule, J. H. Shim, and G. Kotliar, "Correlated electronic structure of $LaO_{1-x}F_xFeAs$," *Phys. Rev. Lett.* **100** (2008) 226402.

[32] Q. Si and E. Abrahams, "Strong correlations and magnetic frustration in the high T_c iron pnictides," *Phys. Rev. Lett.* **101** (2008) 076401.

[33] L. Craco, M. S. Laad, S. Leoni, and H. Rosner, "Normal-state correlated electronic structure of iron pnictides from first principles," *Phys. Rev. B* **78** (2008) 134511.

[34] M. J. Han, Q. Yin, W. E. Pickett, and S. Y. Savrasov, "Anisotropy, itineracy, and magnetic frustration in High-T_c iron pnictides," *Phys. Rev. Lett.* **102** (2009) 107003.

[35] M. M. Qazilbash, J. J. Hamlin, R. E. Baumbach, L. Zhang, D. J. Singh, M. B. Maple, and D. N. Basov, "Electronic correlations in the iron pnictides," *Nat. Phys.* **5** (2009) 647.

[36] D. H. Lu, M. Yi, S.-K. Mo, J. G. Analytis, J.-H. Chu, A. S. Erickson, D. J. Singh, Z. Hussain, T. H. Geballe, I. R. Fisher, and Z.-X. Shen, "ARPES studies of the electronic structure of LaOFe(P,As)," *Physica C* **469** (2009) 452.

[37] R. A. Ewings, T. G. Perring, R. I. Bewley, T. Guidi, M. J. Pitcher, D. R. Parker, S. J. Clarke, and A. T. Boothroyd, "High-energy spin excitations in $BaFe_2As_2$ observed by inelastic neutron scattering," *Phys. Rev. B* **78** (2008) 220501.

[38] Z. P. Yin, S. Lebègue, M. J. Han, B. P. Neal, S. Y. Savrasov, and W. E. Pickett, "Electron-hole symmetry and magnetic coupling in antiferromagnetic LaFeAsO," *Phys. Rev. Lett.* **101** (2008) 047001.

[39] J. Hubbard, "Electron correlations in narrow energy bands," *Proc. Roy. Soc. A* **276** (1963) 238.

[40] M. C. Gutzwiller, "Effect of correlation on the ferromagnetism of transition metals," *Phys. Rev. Lett.* **10** (1963) 159.

[41] J. Kanamori, "Electron correlation and ferromagnetism of transition metals," *Prog. Theor. Phys.* **30** (1963) 275.

[42] A. Reischl, E. Müller-Hartmann, and G. S. Uhrig, "Systematic mapping of the hubbard model to the generalized *t-J* model," *Phys. Rev. B* **70** (2004) 245124.

[43] N. D. Mermin and H. Wagner, "Absence of ferromagnetism or antiferromagnetism in one- or two-dimensional isotropic heisenberg models," *Phys. Rev. Lett.* **17** (1966) 1133.

[44] A. Auerbach, *Interacting electrons and quantum magnetism*. Graduate Texts in Contemporary Physics. Springer, New York, 1994.

[45] R. V. Lange, "Nonrelativistic theorem analogous to the Goldstone theorem," *Phys. Rev.* **146** (1966) 301.

[46] N. W. Ashcroft and N. D. Mermin, *Festkörperphysik*. Oldenbourg Verlag, München, 2007.

[47] R. R. P. Singh, Z. Weihong, C. J. Hamer, and J. Oitmaa, "Dimer order with striped correlations in the J_1-J_2 Heisenberg model," *Phys. Rev. B* **60** (1999) 7278.

[48] O. P. Sushkov, J. Oitmaa, and Z. Weihong, "Quantum phase transitions in the two-dimensional J_1-J_2 model," *Phys. Rev. B* **63** (2001) 104420.

[49] R. R. P. Singh, W. Zheng, J. Oitmaa, O. P. Sushkov, and C. J. Hamer, "Symmetry breaking in the collinear phase of the J_1-J_2 Heisenberg model," *Phys. Rev. Lett.* **91** (2003) 017201.

[50] P. Chandra, P. Coleman, and A. I. Larkin, "Ising transition in frustrated Heisenberg models," *Phys. Rev. Lett.* **64** (1990) 88.

[51] L. Capriotti, A. Fubini, T. Roscilde, and V. Tognetti, "Ising transition in the two-dimensional quantum J_1-J_2 Heisenberg model," *Phys. Rev. Lett.* **92** (2004) 157202.

[52] N. Shannon, T. Momoi, and P. Sindzingre, "Nematic order in square lattice frustrated ferromagnets," *Phys. Rev. Lett.* **96** (2006) 027213.

[53] D.-X. Yao and E. W. Carlson, "Magnetic excitations in the high-T_c iron pnictides," *Phys. Rev. B* **78** (2008) 052507.

[54] D.-X. Yao and E. W. Carlson, "Magnetic excitations of undoped iron oxypnictides," *Front. Phys. China* **5** (2010) 166, `arXiv:0910.2528v1`.

[55] J. Oitmaa, C. J. Hamer, and W. Zheng, *Series Expansion Methods for Strongly Interacting Lattice Models*. Cambridge Univ. Press, Cambridge, 2006.

[56] R. Applegate, J. Oitmaa, and R. R. P. Singh, "Spin waves in J_{1a}-J_{1b}-J_2 orthorhombic square-lattice Heisenberg models: Application to iron pnictide materials," *Phys. Rev. B* **81** (2010) 024505.

[57] B. Schmidt, M. Siahatgar, and P. Thalmeier, "Frustrated local-moment models for iron pnictide magnetism," *Phys. Rev. B* **81** (2010) 165101.

[58] A. N. Yaresko. Private communication, 2009.

[59] J. J. Pulikkotil, L. Ke, M. van Schilfgaarde, T. Kotani, and V. P. Antropov, "Magnetism and exchange coupling in iron pnictides," *Supercond. Sci. Technol.* **23** (2010) 054012.

[60] H. Lee, Y.-Z. Zhang, H. O. Jeschke, and R. Valenti, "Possible origin of the reduced magnetic moment in iron pnictides: Frustrated versus unfrustrated bands," `arXiv:0912.4024v1`.

[61] M. D. Girardeau and M. Popovic-Boziv, "Magnetic ordering in a generalized Heisenberg model with biquadratic exchange. I: Hamiltonian and two-spin eigenstates," *J. Phys. C* **10** (1977) 2471.

[62] I. I. Mazin, D. J. Singh, M. D. Johannes, and M. H. Du, "Unconventional superconductivity with a sign reversal in the order parameter of $LaFeAsO_{1-x}F_x$," *Phys. Rev. Lett.* **101** (2008) 057003.

[63] K. Kuroki, S. Onari, R. Arita, H. Usui, Y. Tanaka, H. Kontani, and H. Aoki, "Unconventional pairing originating from the disconnected fermi surfaces of superconducting $LaFeAsO_{1-x}F_x$," *Phys. Rev. Lett.* **101** (2008) 087004.

[64] P. M. R. Brydon and C. Timm, "Spin excitations in the excitonic spin-density-wave state of the iron pnictides," *Phys. Rev. B* **80** (2009) 174401.

[65] V. Cvetkovic and Z. Tesanovic, "Multiband magnetism and superconductivity in Fe-based compounds," *Europhys. Lett.* **85** (2009) 37002.

[66] W. Lv, F. Krüger, and P. Phillips, "Orbital ordering and unfrustrated $(\pi, 0)$ magnetism from degenerate double exchange in the pnictides," `arXiv:1002.3165v1`.

[67] T. Holstein and H. Primakoff, "Field dependence of the intrinsic domain magnetization of a ferromagnet," *Phys. Rev.* **58** (1940) 1098.

[68] F. J. Dyson, "General theory of spin-wave interactions," *Phys. Rev.* **102** (1956) 1217.

[69] F. J. Dyson, "Thermodynamic behavior of an ideal ferromagnet," *Phys. Rev.* **102** (1956) 1230.

[70] S. Maleev, "Scattering of slow neutrons in ferromagnets," *Sov. Phys. JETP* **6** (1958) 776.

[71] Z. Weihong and C. J. Hamer, "Spin-wave theory and finite-size scaling for the heisenberg antiferromagnet," *Phys. Rev. B* **47** (1993) 7961.

[72] A. Auerbach and D. P. Arovas, "Schwinger Bosons Approaches to Quantum Antiferromagnetism," `arXiv:0809.4836v2`.

[73] G. L. Squires, *Introduction to the theory of Thermal Neutron Scattering*. Dover Publications, New York, 1996.

[74] A. J. A. James, F. H. L. Essler, and R. M. Konik, "Finite-temperature dynamical structure factor of alternating Heisenberg chains," *Phys. Rev. B* **78** (2008) 094411.

[75] A. L. Fetter and J. D. Walecka, *Quantum theory of many particle systems*. International series in pure and applied physics. McGraw Hill, San Francisco, 1971.

[76] F. Krüger and S. Scheidl, "Spin dynamics of stripes," *Phys. Rev. B* **67** (2003) 134512.

[77] D. P. Arovas and A. Auerbach, "Functional integral theories of low-dimensional quantum heisenberg models," *Phys. Rev. B* **38** (1988) 316.

[78] A. Auerbach and D. P. Arovas, "Spin dynamics in the square-lattice antiferromagnet," *Phys. Rev. Lett.* **61** (1988) 617.

[79] C. Raas. Private communication, 2009.

[80] J. Oitmaa. Private communication, 2009.

[81] M. Takahashi, "Modified spin-wave theory of a square-lattice antiferromagnet," *Phys. Rev. B* **40** (1989) 2494.

[82] W. H. Press, S. A. Teukolsky, W. T. Vetterling, and B. P. Flannery, *Numerical Recipes 3rd Edition: The Art of Scientific Computing*. Cambridge Univ. Press, Cambridge, 2007.

[83] A. Smerald and N. Shannon, "Iron pnictides are three dimensional magnets," `arXiv:0909.2207v1`.

[84] P. Chandra and B. Doucot, "Possible spin-liquid state at large *S* for the frustrated square Heisenberg lattice," *Phys. Rev. B* **38** (1988) 9335.

[85] S. Raghu, X.-L. Qi, C.-X. Liu, D. J. Scalapino, and S.-C. Zhang, "Minimal two-band model of the superconducting iron oxypnictides," *Phys. Rev. B* **77** (2008) 220503.

[86] A. Ong, G. S. Uhrig, and O. P. Sushkov, "Spin-wave velocities, density of magnetic excitations, and nmr relaxation in iron pnictides," *Phys. Rev. B* **80** (2009) 014514.

Danksagung

Zuerst möchte ich mich sehr herzlich bei Herrn Prof. Dr. Götz S. Uhrig für die Vergabe des Themas sowie die intensive und hervorragende Betreuung bedanken.

Herrn Prof. Dr. Werner Weber danke ich herzlich für die Übernahme des Zweitgutachtens.

Bei meiner Büronachbarin Eva Bömer bedanke ich mich für die schöne gemeinsame Zeit und die Bereitschaft zum intensiven Korrekturlesen und Durchschauen der Arbeit. Selbiges gebührt auch Fabian Heisterkamp, der ebenfalls freundlicherweise die Arbeit Korrekturgelesen hat.

Ein besonderer Dank geht an Isabelle Exius für ihre Hilfestellung und Beratung im Umgang mit MATLAB. Carsten Raas möchte ich für die Bereitstellung der Daten zur Exakten Diagonalisierung des Heisenberg-Modells mit biquadratischer Wechselwirkung und für die Hilfestellung im Umgang mit Linux danken.

Bei der gesamten Arbeitsgruppe möchte ich für die freundliche Aufnahme und die sehr angenehme Atmosphäre bedanken.

Zuletzt möchte ich mich bei meiner Familie und insbesondere bei meinen Eltern bedanken, die mich stets auf meinem Weg unterstützt und gefördert haben.